Marine Geology
March 2022, Volume 445, Pages 106755 (39p.)
https://doi.org/10.1016/j.margeo.2022.106755
https://archimer.ifremer.fr/doc/00751/86341/

First characterization of the volcanism in the southern Mozambique Channel: Geomorphological and structural analyses

Berthod C. [1, *], Bachèlery P. [1], Jorry Stephan [2], Pitel-Roudaut Mathilde [2], Ruffet G. [3, 4], Revillon Sidonie [5], Courgeon S. [6], Doucelance R. [1]

[1] Université Clermont Auvergne, CNRS, IRD, OPGC, Laboratoire Magmas et Volcans, 6 avenue Blaise Pascal, 63178 Aubière, France
[2] Geo-Ocean, Ifremer, Université de Bretagne Occidentale, CNRS, 29280 Plouzané, France
[3] Université de Rennes 1, Géosciences Rennes, F-35042 Rennes Cedex, France
[4] CNRS (CNRS/INSU) UMR 6118, Géosciences Rennes, F-35042 Rennes Cedex, France
[5] SEDISOR, Univ. Brest UMR6538, IUEM, Plouzané, France
[6] Geneva Petroleum Consultants International, Chemin des Vergers 4, CH-1205, Switzerland

* Corresponding author : C. Berthod, email address : carole.berthod@uca.fr

Abstract :

The southern part of the Mozambique Channel is characterized by a cluster of isolated seamounts, including the Bassas da India atoll and Europa Island, ranging in latitude from 20°S to 22°S and from 38° to 40° in longitude, and located at the Rovuma-Lwandle plate boundary. Only Cenozoic carbonate platforms have previously been studied in this region, with very little work done on the volcanic history. We confirm here the volcanic nature of the basement of the Bassa da India/Europa complex by providing important constraints on the setting of this hitherto poorly understood volcanism.

Recent bathymetric surveys and dredging operations allowed us to map and date these seamounts, comprising, from west to east, the Hall Bank, the Jaguar Bank, Bassas da India, Ptolemee, and Europa. In addition, we discovered, to the south of Bassas da India, two large new polygenetic volcanic edifices, Pamela Seamount 1 (PS1) and Pamela Seamount 2 (PS2), showing heights and diameters of up to 900 m and 13 km, respectively. Mapping and statistical analysis carried out revealed that the volcanic structures of the Bassas da India/Europa complex are organized along two main alignments with different stages of development: (i) a NE-SW volcanic alignment characterized by volcanic ridges up to 700 m in height, comprising small individual volcanic cones; and (ii) a NW-SE volcanic alignment in which many large and well-developed individual volcanic cones can be found. From this distribution of the volcanism, we suggest that the large volcanic edifices of the Bassas da India/Europa complex were fed by long-lived magma systems, repeatedly supplied from deep magma reservoirs through a significant network of dykes and faults, with lateral injections of magma guided by a dense network of faults allowing magma to reach the surface along rift-zones. 40Ar/39Ar dating confirms that the volcanism covers a period from the Oligo-Miocene to the Pleistocene, and probably extends to the present day. The two volcanic alignments are also consistent with the tectonic features already recognized for the region and are spatially superimposed by active seismicity. Magma ascent is strongly controlled by large pre-existing crustal structures.

Highlights

► Bassas da India/Europa seafloor is characterized by seven large seamounts and more than 430 volcanic cones ► Miocene to Pleistocene volcanism is distributed along two main trends with different stages of maturation ► Magma ascent is strongly controlled by large pre-existing crustal structures ► Large edifices are fed by a well-developed magmatic system whereas volcanic ridges are supplied by episodic lateral magma migration though a network of faults.

Keywords : Mozambique channel, Bassas da India, Europa, Volcanic ridge, Volcanic cones, Structural inheritance

1. Introduction

The most voluminous volcanic activity on Earth occurs in the deep sea environment (Crisp, 1984), but it is also the least known. Based on bathymetric surveys and satellite data, the number of estimated seamounts varies by several orders of magnitude, from 200,000 for large seamounts to 25 million including those with smaller features (Wessel, 2007; Wessel et al., 2010; Yesson et al., 2011). Despite the large number of volcanic seamounts, their eruptions are difficult to access, and they are rarely studied in sufficient detail to allow a good understanding of the eruption processes and magma emplacement in the submarine realm (Fornari et al., 1988; Rubin et al., 2012).

The Mozambique Channel is characterized by scattered young submarine volcanism. Over the past fifty years, much work has been done to understand the evolution of the Mozambique channel and its margins (e.g., Heirtzler & Burroughs, 1971; Scrutton, 1978; Norton and Sclater, 1979; Segoufin and Patriat, 1980; Thompson et al., 1982; Martin and Hartnady, 1986; Mougenot et al., 1986; Coffin and Rabinowitz, 1987; Leclaire et al., 1989; Raillard, 1990; Cox, 1992; Hartnady et al., 1992; Ben Avraham et al., 1995; Tikku et al., 2002; Jokat et al., 2003; Bernard et al., 2005; König and Jokat, 2006; Eagles and König, 2008; König and Jokat, 2010; Leinweber and Jokat, 2012; Mahanjane, 2012; Leinweber et al., 2013; Reeves, 2014; Davis et al., 2016; Klimke et al. 2016; Mueller et al., 2016; Nguyen et al., 2016; Phethean et al., 2016; Reeves et al., 2016; Mueller and Jokat, 2017; Klimke et al. 2018; Reeves, 2018; Stamps et al., 2018; Tuck-Martin et al, 2018; Mueller and Jokat, 2019; Sinha et al., 2019; Thompson et al., 2019; Vormann et al., 2020; Stamps et al., 2021; Vormann and Jokat, 2021a). However, Cenozoic volcanism in the Mozambique Channel remains little studied.

Since the Cretaceous, volcanism has spread to many places in the Mozambique Channel, forming archipelagoes, isolated islands, atolls, seamounts and volcanic ridges. The morphology, nature and age of this volcanism, from the northernmost archipelagoes (i.e., Glorieuses and Comoros Islands, Fig. 1a) to the southernmost islands and seamounts (Europa and Bassas da India, Mt Bourcart, Almirante Leite, and Mozambique Ridge, Fig. 1b), is poorly known or incompletely understood, particularly with regard to the submarine part of these edifices. Several hypotheses coexist as to the source of this Cenozoic volcanism, suggesting a link with the East African Rift System (Kusky et al. 2010; Franke et al., 2015; Michon, 2016; Courgeon et al., 2018; Deville et al., 2018; O'Connor et al. 2019; Famin et al., 2020; Wiles et al. 2020; Vormann and Jokat, 2021b), involving lithospheric fractures and/or a combination of tectonic microplates (Upton, 1982; Nougier et al., 1986; Saria et al., 2014;

Franke et al., 2015; Michon, 2016; Deville et al, 2018; Courgeon et al, 2018; Stamps et al., 2018; Famin et al., 2020; Stamps et al., 2021; Tzevahirtzian et al., 2021), and/or the influence of plume-related thermal anomalies or a superplume mantle under East Africa (e.g., Emerick and Duncan, 1982; Hartnady, 1985; Späth et al., 1996; Class et al., 1998; O'Connor et al. 2019).

The northern entrance of the Mozambique channel is the site of a frequently active volcanism in the Comoros archipelago (Fig. 1a). Indeed, Karthala volcano (Grande Comore Island), which forms the highest point of the Comoros archipelago, is one of the largest active volcanoes in the world and the second most active volcano in the Indian Ocean (Bachèlery et al., 2016). In addition, volcanic products a few thousand years old have recently been identified on the island of Anjouan, southeast of Grande Comore (Quidelleur et al., 2022). Mayotte Island, the most easterly island of the archipelago is also affected by active volcanism with unprecedented offshore seismo-volcanic activity (Cesca et al., 2020; Lemoine et al., 2020; Berthod et al., 2021a; Feuillet et al., 2021). It is obvious that volcanism represents a major risk for the population living in the Comoros archipelago. Consequently, this active volcanism at the northern entrance of the Mozambique Channel is a focal point for study by the scientific community.

The southern part of the Mozambique Channel is also characterized by several scattered volcanic edifices, including Mt. Bourcart and an unnamed seamount identified as Mt. X (Breitzke et al., 2017), Almirante Leite (Hartnady, 1985; Wiles et al., 2014; O'Connor et al., 2019), and a cluster of volcanic landforms consisting of two uninhabited islands, the atoll of Bassas da India and the island of Europa (Fig. 1b, Jokat, 2006; Courgeon et al., 2016, 2017; Breitzke et al., 2017, Courgeon, 2017; Dorschel et al., 2018), where healthy and flourishing coral reefs can be observed (Bouchard and Crumplin, 2011; Jorry et al., 2016; Levin et al., 2018; McClanahan et al., 2021), as well as two drowned Neogene shallow-water carbonate platforms (Hall and Jaguar Banks, Fig. 1c), whose platform tops are currently located at a depth of hundreds of meters below sea level (Courgeon et al., 2016). These edifices are the most striking parts of a submarine volcanic complex extending over a length of 200 km. This complex, located between 21.5°S – 22.3° S and 39.5°E – 40.3° E, is poorly understood and is the target of our work.

Previous work by Courgeon et al., (2016), Courgeon (2017), and Counts et al. (2018) focused on the carbonate platforms and the associated superficial volcanic structures of this complex. The goal of this paper is to describe from a morphological perspective the volcanic

bedrock of these carbonate platforms, in order to better understand the origin of the Bassas da India/Europa complex and the related magmatic processes. For this purpose, we analyzed bathymetry DEMs and imaged the regional distribution and the morphology of the volcanic structures, using multibeam bathymetry and acoustic backscatter images extending around Bassas da India and Europa and the surrounding edifices, acquired during the PAMELA-MOZ01 (Olu, 2014) and PAMELA-MOZ04 (Jouet and Deville, 2015) cruises. We also carried out the first $^{40}Ar/^{39}Ar$ dating on dredged volcanic samples from this area. Our study confirms the volcanic nature of the Bassas da India/Europa complex, shows a clear tectonic control for the formation of the submarine seamounts, and highlights the relevance of considering Cenozoic volcanism in the geodynamic evolution of the Mozambique Channel.

2) Geological context

Gondwana break-up and inherited structures

The Mozambique Channel, in the SW Indian Ocean, between the East-African continental margin and the Madagascar continental fragment, is related to the break-up of Gondwana supercontinent and the relative drift of the African and "Antarctico-Indio-Madagascarian" continental blocks. The history of the opening of the Mozambique Channel has been well documented (Cox, 1992; Reeves, 2000; Jokat et al., 2003; König and Jokat, 2006; Eagles and König, 2008; Leinweber and Jokat, 2012; Mahanjane, 2012; Reeves 2014; Mueller and Jokat, 2017; Tuck-Martin et al, 2018, Mueller and Jokat, 2019; Thompson et al., 2019). The southward motion of Madagascar relative to Africa occurred from the Middle Jurassic to the Early Cretaceous (~165-120 Ma, Coffin and Rabinowitz, 1987; Leinweber and Jokat, 2012; Mahanjane, 2014; Mueller and Jokat, 2019; Thompson et al., 2019) through the activity of a major NNW-SSE transform fault known as "Davie Ridge" (Fig. 1a, Scrutton, 1978; Rabinowitz et al., 1983; Coffin and Rabinowitz, 1987; Leclaire et al., 1989; Bassias and Leclaire, 1990; Bassias, 1992; Mahanjane, 2014; Bassias and Bertagne, 2015; Courgeon et al., 2018; Vormann et al., 2020; Vormann and Jokat, 2021a).

To the south of this major tectonic structure, the Mozambique Basin is part of the Africa-Antarctica Corridor extending from the Mozambique coast in SE-Africa to the coast of East-Antarctica (Bernard et al., 2005; Mueller and Jokat, 2019). Since the northern part is characterized by east–west striking magnetic anomalies from about 20°S to 27°S (Fig. 1a), the Mozambique Basin was recognised to have been created by almost north–south oriented

spreading between Africa and Antarctica (Mueller and Jokat, 2019). Three major north–south oriented tectonic features, the Eric Simpson Fracture Zone (ESFZ), the Prince Edward Fracture Zone (PEFZ) and the the Andrew Bain Fracture Zone (Fig. 1a), have been identified and divide the Africa-Antarctica Corridor into three discrete spreading segments (Mueller and Jokat, 2019).

Cenozoic tectonic setting

The relative drift during the Jurassic was followed by volcano-tectonic stages associated with the separation of India and Antarctica from Madagascar during the Cretaceous period, and then with the development of the East African rift system (EARS) from the Oligocene up to the present (Chorowicz, 2005; Ebinger, 2012; MacGregor, 2015). The present-day EARS is a well-defined continental-scale rift, linked to volcanism and earthquakes, which extends southward along two main terrestrial branches (Chorowicz, 2005). These eastern and western branches separate the Nubian and Somalian plates, and between them lie two microplates, the northern Victoria and southern Rovuma microplates, which have developed in response to rift kinematics with a third microplate, the Lwandle microplate (Hartnady, 2002; Stamps et al., 2008; Saria et al., 2014; Stamps et al., 2021). The southern extension of the EARS is well-establish north of the Mozambique Channel (Mougenot et al., 1986; Grimison and Chen, 1988; Calais et al. 2006; Stamps et al., 2008; Yang and Chen, 2010; Franke et al., 2015, Michon 2016). In addition, recent studies based largely on GPS measurements, seismology and structural analysis, proposed that the southern part of the Mozambique Channel is crossed, from NE to SW, by the Rovuma/Lwandle plate boundary, following the Quathlamba seismic axis, a linear cluster of seismicity between Madagascar and southern Mozambique (Hartnady, 1990; Hartnady et al. 1992; Stamps et al., 2008; Déprez et al., 2013; Saria et al., 2014; Stamps et al., 2015, 2021). Analysis of the spatial distribution of active faults in the area, performed by Deville et al. (2018), reveals the presence of a 200 km - wide system of faults, trending N45–80°, superimposed onto the Quathlamba seismic axis. An east-west orientated steep-flanked depression located in the southern part of the Mozambique Channel is also interpreted as the superficial expression of this regional extension, and associated with the present-day kinematics of the East African Rift System (Wiles et al., 2020). Furthermore, the structural study carried out by Deville et al. (2018) demonstrates that a second set of N160–180° trending faults, mostly observed north of 20°S, is probably associated with, and controlled by, the Davie Ridge structure.

Cenozoic volcanism

Since the Cretaceous, volcanic activity has been concentrated in several sectors along the Mozambique Channel. To the north, the origin of the Neogene Comoros volcanism is the subject of a long-lasting debate (Emerick and Duncan, 1982; Emerick, 1985; Class et al., 1998; Späth et al., 1996; Debeuf et al., 2003; Debeuf, 2009; Michon, 2016). Michon (2016) points out that the Comorian volcanism is superimposed onto seismic zones and graben structures (Nougier et al., 1986; Zinke et al., 2003; Debeuf, 2009; Pelleter et al., 2014). This has led the volcanism across the Comoros archipelago to be interpreted as being related to an E-W right-lateral shear zone or a wide trans-tensional boundary between the Lwandle and Somali plates, rather than simply the surface expression of a deep mantle plume (Michon, 2016; Famin et al., 2020; Feuillet et al., 2021; Tzevahirtzian et al., 2021). The Cretaceous Glorieuses volcanism to the north is older (ca. 69 Ma, Leroux et al., 2020), and has recently been explored and sampled (Berthod et al., 2021b).

To the south, Cenozoic volcanism has been recognized for the Sakalaves seamounts, the Bassas da India atoll, Europa Island, Hall and Jaguar Banks, Mt. Bourcart and an unnamed seamount identified as Mt. X which was discovered during the RV Sonne cruise SO-183 (Fig. 1b, Jokat, 2006). Young volcanic edifices are also present in the heart of the Natal Valley and on the Mozambique Ridge (Hartnady, 1986; Ben Avraham et al., 1995; Jokat, 2009, 2014; Castelino et al., 2016; O'Connor et al., 2019). The isotopic signature of these ~7 Ma basanites-alkaline basalts, coupled with recent tomographic models of the Afro-Arabian mantle (Hansen et al., 2012), suggests a link with an African Superplume beneath eastern Africa (O'Connor et al., 2019). Uplift of the South African Plateau during the Upper Cretaceous and Cenozoic has been documented (Ponte et al., 2019; Baby et al., 2020), interpreted as the African Plate passing over the African Superplume, and resulting in a partial rejuvenation of the topography in the Neogene (Baby et al., 2020).

Bassas da India/Europa region

The general features of the seafloor geomorphology of the Bassas da India/Europa region have been outlined by Breitzke et al. (2017), Dorschel et al. (2018), and Wiles et al. (2020). Volcanism appears to be diversely distributed in space, with an alignment of five edifices in two distinct directions (Figs 1 and 2). Hall and Jaguar Banks and Bassas da India atoll are roughly aligned along the N40° trend with the Mt. Bourcart and Almirente Leite seamounts, whereas in the southeast, Europa Island, Ptolemee seamount and Bassas da India atoll are aligned along a N150° trend. Furthermore, Europa Island and Mt. X are also aligned along the

N40° trend (Fig. 1b). Bassas da India atoll and Europa Island are topped by modern carbonate platforms (Fig. 1c). Hall and Jaguar Banks, SW of Bassas da India, which consist of drowned shallow-water carbonate platforms, now also lie at a depth of hundreds of meters (Courgeon et al. 2016). Sediment transfer on the slopes of Bassas da India, Europa and the carbonate platforms has been widely described by Counts et al. (2018). Volcanic rocks, identified as olivine basalts, pyroxene-phyric basalts and altered basalts, have been dredged from the flanks of the Jaguar seamount (Jokat, 2006). In addition, volcanic seamounts, such as Ptolemee seamount, southeast of Bassas da India (Fig. 1c; Jorry, 2014), were highlighted during recent oceanographic surveys (Jorry, 2014; Olu, 2014). In this region, the overall evolution of drowned flat-topped carbonate platforms is intimately linked with tectonics and rejuvenated volcanism (Courgeon et al., 2016, 2017; Courgeon, 2017). Previous studies mostly focus on shallow-water carbonate platforms and only give an indirect indication of the age and chronology of the recent volcanic activity. The Hall and Jaguar drowned carbonate platforms are locally overlain by volcaniclastic deposits and can have been cut by explosive volcanic features (e.g., craters – see Courgeon et al., 2017). These carbonate platforms and terraces are occasionally covered by submarine volcanic lava flows, indicating relatively recent (i.e., Late Cenozoic) volcanic activity, synchronous and/or postdating carbonate platform growth (Courgeon et al., 2017, Deville et al., 2018). These carbonate platforms have been dated at 16.3 to 5.4 Ma, giving a minimum age for the building of the volcanic edifice (Courgeon, 2017; Courgeon et al., 2017). Based on 2D seismic sections, Courgeon et al. (2017) proposed that volcanism began during Upper Oligocene times.

By describing the volcanic forms (cones, craters, calderas) and erosional-depositional features (landslide scars, channels, mass-wasting deposits) on their submarine flanks and neighboring slopes, our compilation of multibeam bathymetry data significantly improves our knowledge of the general seafloor geomorphology of the Bassas da India/Europa volcanic edifices (Breitzke et al., 2017; Dorschel et al., 2018; Wiles et al., 2020), and updates the various morphometric features published by Courgeon et al., (2016), Courgeon (2017), and Counts et al. (2018).

3) Material and methods

We performed a basic analysis of physical variables of all identified volcanic cones to describe the characteristics and distribution of the volcanic structures that form the Bassas da India/Europa complex. Our study was based on bathymetry and reflectivity data collected by Kongsberg EM122 and Kongsberg EM 710 multibeam echosounders (MBES), on board the R/V Atalante, during the PAMELA-MOZ01 (Olu, 2014) and PAMELA-MOZ04 (Jouet and Deville, 2015) cruises. For shallow water (0-1500 m), Kongsberg EM710 MBES was deployed with its 70 – 110 kHz frequency and 256 beams (400 in high-resolution mode). For deeper water, Kongsberg EM122 multibeam was used with its 12 kHz frequency and 288 beams (432 in high-resolution mode).

Geomatics

Acoustic data were processed by the Ifremer hydrography team with Caraibes software version 4.3 (©Ifremer): automatic and manual quality controls, tide and sound velocity corrections and gridding. We used the average of all the depths measured in each cell to grid the cleaned XYZ data. Cell size resolution of bathymetric and reflectivity rasters were chosen according to the spatial resolution of the echosounder, thus the sampling varies from 100 m to 10 m, accordingly. We used the datum WGS-84 coordinate system with Mercator projection.

Individual seamounts were identified by visual inspection coupled with the bathymetry using ArcGIS™v10.3 software, based on bathymetry, associated slope and reflectivity data whose space grid resolutions range from 10 m to 30 m. The basal outlines of seamounts were then redigitized and combined in a shapefile in the WGS84 geographic coordinate system.

For the geometrical analysis, the perimeters, lengths and areas of seamounts were calculated with the *arcpy.AddGeometryAttributes_management* arcpy tool in a geodesic coordinate system. To define the direction of each seamount, we used the rotation values from the theoretic ellipses calculated for each seamount polygon in the Mercator projection system with the *Spatial Statistics Tools/Directional Distribution* ArcGis tool.

For the spatial analysis, in order to obtain comparable statistic results for each area studied, we used the bathymetric raster of 100 m cell size resolution which covers all seamounts homogeneously. Mean, maximum, minimum and the range of bathymetric values for each seamount were calculated with the *Spatial Analyst/Zonal statistics as table* ArcGis Tool. Maximum and mean slopes were calculated with the same ArcGis Tool directly from the 100 m slope raster, derived from the 100 m bathymetric raster.

$^{40}Ar/^{39}Ar$ dating

Dredges were performed on Hall and Jaguar Banks (DW05 and DR19, respectively, Fig. 1c, Tab. 1) and Bassas da India (DR08) during the PAMELA-MOZ01 (Olu, 2014) and PAMELA-MOZ04 (Jouet and Deville, 2015) cruises. Thin sections (Fig. S1 in supplementary material) helped select the freshest samples (Tab. 1): MOZ01-DW05-01 and MOZ01-DW05-13 (Hall Bank), MOZ01-DR19-04 (Jaguar Bank) and MOZ04-DR08-01(Bassas da India). MOZ01-DW05-01 is a basanite made of olivine phenocrysts mostly iddingsitized in a fine-grained microcrystalline mesostasis (Fig. S1a in supplementary material). MOZ01-DW05-13 presents a more evolved composition with large euhedral feldspar phenocrysts in a groundmass composed of alkali feldspar, nepheline, clinopyroxene, biotite, titanite, amphibole and Fe-Ti oxides (Fig. S1b in supplementary material). MOZ01-DR19-04 and MOZ04-DR08-01 are ultramafic rocks and consist of sub-euhedral to euhedral olivine and zoned clinopyroxene phenocrysts embedded in an oxidized matrix (Fig. S1c,d in supplementary material). Using these petrological observations, we selected three millimetric (1 - 2 mm) whole rock grains (MOZ01-DW05-01, MOZ01-DR19-04 and MOZ04-DR08-01) and one biotite crystal (MOZ01-DW05-13). Selected fractions were analyzed by the $^{40}Ar/^{39}Ar$ method in step-heating using a CO_2 laser probe coupled with a MAP 215 mass spectrometer. The whole procedure is described in detail in Ruffet et al., (1991, 1995, 1997). These samples were irradiated in two batches, IR32 and IR34, in the 8C facility of the McMaster Nuclear Reactor (Hamilton, Ontario, Canada). Irradiation of biotite MOZ01-DW05-13 lasted 49.58 h with a global efficiency (J/h) of 8.201 x 10^{-5} h^{-1} whereas irradiation of whole-rock samples MOZ01-DW5-01, MOZ01-DR19-04 and MOZ04-DR08-01 lasted 50.00 h with a global efficiency (J/h) of 8.618 x 10^{-5} h^{-1}. The irradiation standard was sanidine TCRs (28.608 ± 0.033 Ma, see Renne et al., 1998, 2010, 2011). Blanks were performed routinely each first or third/fourth run and are subtracted from the subsequent sample gas fractions. Apparent age errors are plotted at the 2σ level and do not include the errors on the $^{40}Ar^*/^{39}Ar_K$ ratio, and age of the monitor and decay constant. Plateau ages were calculated if 70% or more of the $^{39}Ar_K$ was released in at least three or more contiguous steps that defined apparent ages in agreement, to within 2σ, with the integrated age of the plateau segment. The errors on the $^{40}Ar^*/^{39}Ar_K$ ratio and age of the monitor and decay constant are included in the final calculation of the error margins on the plateau ages.

$^{40}Ar/^{39}Ar$ ages are provided with 2σ errors. Analytical data and parameters used for calculations (e.g., isotopic ratios measured on pure K, Ca and Cl salts; mass discrimination; atmospheric argon ratios; J parameter; decay constants) and reference sources are available in the supplementary Table S1.

4) Results

Mapping and distribution of the volcanic edifices

A detailed analysis of the geomorphological features of each main edifice and of their submarine neighboring slopes, based on the multibeam backscatter and bathymetric data set, is provided in the following sections.

a. Hall Bank

Hall Bank is located in the western part of the area studied (21°52' S, 39°04' E; Figs 1 and 2). Morphologically, Hall Bank constitutes a circular seamount with a diameter of 26 km that rises more than 2600 m from the surrounding seafloor (Fig. 3). The flat top of the seamount, 8 km in diameter and rising to within 500 m of sea level, corresponds to a drowned Cenozoic carbonate platform (Courgeon et al., 2016). Volcanic structures and material (Fig. 4a), including a clearly identifiable explosion crater (Fig. 5a), have been previously reported at the top of the platform indicating recent volcanic activity, postdating the carbonate platform development (Pliocene in age, Courgeon et al., 2017). Samples of volcanic rocks have been collected by dredging (MOZ01-DW05, see location on Figs 1c and 5a, b) from the top of the carbonate platform. $^{40}Ar/^{39}Ar$ age spectra yielded by analysis of a millimetric whole-rock fragment and biotite crystals from dredged samples MOZ01-DW05-01 and MOZ01-DW05-13, provided two perfectly concordant plateau ages at 20.5 ± 1.5 Ma and 20.2 ± 0.1 Ma (Fig. 6 and supplementary Table S1).

The carbonate platform and volcanic edifice are affected by several faults and numerous landslide scars (W, SW, NW, S and NE flanks, Figs 4b and 5a, b). The SW, W and NE flanks of the edifice are characterized by the presence of marked erosional channels and gullies that extend to the base of the seamount (Figs 2 and 5a, b). Volcanic cones can be identified on the north and southeast flanks of Hall Bank, as well as eastwards along a submarine structure toward Jaguar Bank. A cluster of volcanic cones is observed on the northern flank of Hall Bank (Fig. 5a, b). In this area, we also identified a surface morphology with irregular

contours, a constant slope and a high and homogenous sonar backscatter signal. Since high acoustic backscatter signals can be interpreted as volcanic units not covered by significant marine sedimentation, this surface morphology seems to reveal a lava flow that spreads more than 5 km northwards. The dimensions of this unit are up to 8 km in length, 50 – 100 m in height and more than 2 km in width (Fig. 5a, b). A similar acoustic signature and slope are observed in the southwestern portion of Hall Bank, where a thin lava flow might extend over an area of at least 4 km in length and 200 m in width (Fig. 5a, b). Alternatively, this high-backscatter trail can be interpreted as a recent coarse-grained volcaniclastic flow within a channel.

In other places, at a depth of more than 1200 m, the seafloor is characterized by a patchy backscatter pattern probably indicative of a coarse- to fine-grained sedimentary cover. In contrast, east of Hall Bank, a submarine high which is over 10 km long and 5 km wide, with high-backscatter and high topography, appears to extend the seamount with an average along-axis slope of 8 to 11° toward Jaguar Bank (Figs 3b, 5a, b). Interpreted as a volcanic ridge, the unit is marked by the presence of normal faults, cones, cone alignments and inferred lava flows.

b. **Jaguar Bank**

Jaguar Bank lies immediately to the east of Hall Bank (21°54’ S, 39°26’ E; Figs 1 and 2). This 2000 m-high seamount displays a triangular shape, extending over more than 40 km along its greatest axis, following NNW-SSE and WSW-ENE orientations (Fig. 2). The submarine relief is marked by a flat-topped morphology (Fig. 3a), which corresponds to a submerged Oligocene-Miocene shallow-water carbonate platform lying at about 300 – 500 m below sea level, previously described by Courgeon et al. 2017 (Fig. 5c, d). The carbonate platform top is characterized by a smooth surface and the presence of volcanic morphologies interpreted as being lava flows (Courgeon et al., 2017), and by a dense network of N70 – 75° oriented normal faults (Fig. 2) that lower the southern part of the platform surface (Courgeon et al., 2016; Miramontes et al., 2019). Following Courgeon et al. (2017), some of these faults are associated with volcanic activity. Similarly to Hall Bank, the edge of the carbonate platform is affected by multiple landslide scars that are associated with erosive channels and gullies affecting most of the edifice (Fig. 5c, d).

The slopes of the Jaguar edifice extend NNW with a 12 km-wide topographic high, trending N150° along a radial direction from the carbonate platform (Figs 2 and 5a, b). This

flank, with its uneven relief, and on which volcanic cones can be identified, can be considered a remnant of the volcanic bedrock. The acoustic backscatter pattern on this morphological high is not uniformly high, suggesting the presence, at least partially, of a sedimentary cover. The eastern part of this volcanic flank is cross-cut by a N60° normal fault that seems to be overlain by a large volcanic cone (labelled "Post-fault volcanic cone" on Fig. 5c, d).

North-east of Jaguar Bank, a volcanic ridge is clearly revealed by the bathymetry and the high-backscatter signal, contrasting with the lower backscatter of the surrounding seabed on either side of the ridge, indicative of a smooth, fine-grained sediment cover (Fig. 5c, d). This well-developed N65° volcanic ridge, with an average along-axis slope of 4°, rises locally to more than 1000 m above the surrounding seafloor (Fig. 2b). This ridge has a slightly convex along-axis profile, from the carbonate platform to the deep sea, with steeper slopes (up to 17°), before terminating in an extension composed of a series of pointy volcanic cones over 200 m high (Figs 5c, d and 7b). Numerous volcanic cones have been identified, their distribution providing insight into the preferential intrusion paths and extension of this volcanic ridge to more than 20 km from the carbonate platform. This volcanic relief, about 10 km wide, is parallel to a dense network of pluri-kilometric N60 – 75° normal faults (Figs 2 and 5c, d) and spreads to Bassas da India atoll. Volcanic cones on both sides of this volcanic ridge seem also to be aligned along a N140° direction (Fig. 5c, d). A whole-rock fragment of the MOZ01-DR19-04 sample dredged on the northern flank of the ridge (see location on Figs 1c and 5c, d) yielded concordant plateau and isochron ages of 9.6 ± 0.2 Ma and 9.7 ± 0.3 Ma, respectively (Fig. 6 and supplementary Table S1).

It is likely that Jaguar Bank also extends in a SSE direction with the presence of several volcanic cones (see Fig. 2). The lack of bathymetric data in this area does not allow us to fully describe this submarine extension of the bank.

c. **Bassas da India**

Bassas da India atoll is located in the northeastern part of the volcanic complex (21°54' S, 39°26' E; Figs 1 and 2). The edifice constitutes a circular volcanic feature, 45 km in diameter, which rises more than 3000 m from the surrounding seafloor (Fig. 3a). On the northwestern to northeastern sides, submarine slopes are relatively steep, cut by slope failures and many erosive channels and gullies (Figs 2 and 7c, and *Figs 3b and 9b in Count et al., 2018*). Mass transport deposits have been recognized from interpretation of seismic data (Counts et al., 2018). The atoll itself is fringed by a drowned terrace, at a depth of about 400

m to 600 m, and mainly developed towards the south (Fig. 2). A major WSW-ENE normal fault is clearly discernible, separating this submarine terrace from the main platform, and affecting the flanks of the seamount (Figs 1 and 2 - see also Courgeon et al. 2016, Fig. 3a). Courgeon et al. (2017) recognized successive collapse structures along this southern flank related to normal faulting. Volcanic landforms have been identified along the southern edge of this submarine terrace (Fig. 4c and Courgeon et al., 2017), and volcanic rocks have been collected from there (MOZ04-DR08, Fig. 1c). A single whole rock fragment of sample MOZ04-DR08-01 yielded perfectly concordant plateau and isochron ages at 8.0 ± 0.2 Ma (Fig. 6 and supplementary Table S1).

The southern flank of Bassas da India shows high backscatter signals that are interpreted as areas of predominantly volcanic material (Figs 2, and 8a, b). The sector is characterized by N60° normal faults and many aligned volcanic cones, which is consistent with a preferential intrusion path. East of Bassas da India, the high-offset normal fault runs down the middle of a small volcanic ridge (average along-axis slope of 11°, about 10 km in length, 5 km in width, and 400 m in height at its maximum). To the southwest of Bassas da India, a volcanic promontory (10 km in width), associated with a dense fault network (Figs 2 and 7b), extends toward Jaguar Bank. This structure, which extends more than 15 km beyond the Bassas da India submarine terrace, with an along-axis average slope of 6° in its median section, seems to connect with the volcanic ridge northeast of Jaguar Bank described above, with a group of tall pointy volcanic cones marking the continuity between the two ridges (Figs 3b, 7b). In these areas, volcanism seems to be closely related to tectonics, with a dense networks of faults and volcanic cones. Although the faults frequently intersect the volcanic structures, at least some of the volcanic cones mask the fault zone, indicating later emplacement (Fig. 8a, b). This suggests that eruptive activity was coeval with tectonic activity, at least in this region.

d. **Ptolemee seamount**

Located between Bassas da India and Europa (22.00° S, 46.06° E, Figs 1 and 2), Ptolemee seamount was discovered in 2014 during the Ptolemee oceanographic expedition (Jorry, 2014). This circular edifice is about 20 km in diameter and up to 2000 m in height (Fig. 3a). The seamount rises to 770 m below sea level, and at least three distinct ridges extend south-southeast, north-northwest and east, from a very well-preserved caldera at its summit (Figs 7d and 8c, d). This caldera, about 5 km^2 in area, extending N70° – 75°, has a

horseshoe shape open to the east. Several volcanic cones are identifiable within and along the rim of the caldera. The main volcanic ridges are well defined by their high backscatter signal and numerous elongated and aligned volcanic cones (Fig. 8c, d). The north-northwest and south-southeast volcanic ridges share the same orientation (N155°). Together they are about 40 km in length and 3 – 6 km in width. The north-northwest volcanic ridge ends abruptly at the northern limit, whereas the south-southeast volcanic ridge extends to the south up to the Europa edifice with an average along-axis slope of 4° (Figs 3b, 7d, 8c, f). These volcanic ridges are dominated by the presence of numerous large volcanic cones. Another 3 km-wide volcanic ridge extends more than 18 km eastwards from the summit of Ptolemee seamount, with an along-axis average slope of 6°, and several large volcanic cones, mainly towards its eastern end (Figs 7d and 8c, d). To the west of the summit a topographic high and a cone alignment, with almost the same orientation as the eastern ridge, appears to exist. No mass transport deposits, erosive channels or superficial expression of faults were observed in this zone. Apart from the volcanic ridges and cones described above, the flanks of Ptolemee seamount are characterized by low acoustic backscatter, indicative of a smooth, fine-grained sedimentary cover.

e. **Pamela Seamounts 1 and 2**

The area between Bassas da India atoll and Ptolemee seamount comprises two domains characterized by massive and reflective edifices, and numerous volcanic features, suggesting the existence of two large volcanic edifices, previously unknown, hereafter called Pamela Seamount 1 (21.37° S, 39.56° E, Fig. 2) and Pamela Seamount 2 (21.80° S, 40.06° E). The existence of Pamela Seamount 1 (PS1) can be inferred from the 952 m-resolution 2014 GEBCO bathymetry but the new bathymetric map carried out during the PAMELA cruises provides greater accuracy, from 100 m to 30 m-resolution, of the morphology and characteristics of the northern and eastern flanks of this seamount. Its diameter and height were estimated at about 30 km and 1500 m, respectively (Fig. 7c, d). Numerous volcanic cones have been identified that lie along two main alignments oriented N70° and N115° (Figs 7d and 8a, b). These preferential orientations are also observed in the morphology of the elongated cones. As for Ptolemee seamount, 3 – 5 km-wide volcanic ridges radiating from the summit are identifiable to the east (average along-axis slope of 4°) and the south-southwest (with an along-axis average slope of 8°). They concentrate most of the identifiable volcanic cones of PS1. Extending the south-southeast volcanic ridge southwards, several large, isolated

pointy cones (over 400 m high) occur on the seafloor between PS1 and PS2 (Figs 3b and 7d). To the northwest of PS1, several faults can be identified, suggesting a NE-SW trending graben, a few hundred meters deep (Fig. 7c), between PS1 and Bassas da India. Volcanic cones are numerous in this region, and are distributed along a main NW-SE trend (Fig. 8a, b). This trend defines a topographic high between PS1 and Bassas da India, rising to about 700 m above the surrounding seabed, locally downcut by the NE-SW trending graben (Fig. 7a,c and 8a, b). On the eastern flank of PS1, a gully over 300 m wide and about 200 m deep is identifiable (Fig. 7a, c). It could be associated with a fault intersecting a volcanic cone (Fig. 8a, b).

Pamela seamount 2 (PS2) rises more than 900 m high from the seafloor to the north of Ptolemee (Fig. 7d). This seamount, also not previously reported in the literature, displays similar features to the Ptolemee seamount. The edifice is made of numerous volcanic cones and displays a roughly oval morphology (16 x 10 km in diameter) with an elongated base along a N50° axis, and no discernible volcanic ridges.

f. **Europa**

Europa Island, located in the southeastern part of the study area (22°21' S, 40°21' E; Figs 2 and 8e, f), rises more than 2500 m from the ocean floor (Fig. 3). The island, 6 km in diameter, with a maximum altitude of 6 m, is surrounded by a well-developed fringing reef (Jorry et al., 2016). Europa edifice exhibits a circular shape with a basal diameter of up to 40 km. The slopes are largely covered by a thin sedimentary cover, as evidence from seismic data and acoustic backscatter by Counts et al. (2018). Significant areas of erosion with many channels are identified all around the edifice (Fig. 8f). Some of them with higher backscatter values can be active. Irregular and undulating surfaces, located downslope of these channels, have been interpreted as downslope mass transport and gravity flow deposits (Counts et al., 2018). A normal fault has been identified in the northern part of Europa. The fault is oriented N40°, which is similar to the N40 – 80° system observed between Hall Bank and Bassas da India (Fig. 5). This fault seems to mark a transition zone between the well-defined channels running along the northern flank of Europa, and lobes of mass-wasting deposits (Fig. 8e, f). The presence of deposits at the base of the fault can be associated with a steep decrease in slope between the fault scarp and the plain. The absence of a change in slope and the regular decrease in slope along the channel confirm that its activity postdates the faulting, and indicates longterm channel activity (Fig. 8e). A few volcanic cones and volcanic outcrops,

even megablocks, with high-backscatter signatures, are visible around Europa (Figs 2 and 8e, f). Volcanic cones present no preferential distribution. Some of them seem to overlie mass transport deposits in the northern part of Europa, indicating a volcanic activity that could locally postdates sedimentation processes reaching the deep seafloor (see *Fig. 7a in Counts et al., 2018*).

Characteristics of the volcanic cones

Numerous volcanic cones and their alignments can be identified either on the flanks of the seven large edifices or along the volcanic ridges (Figs 2, 5 and 8). A total of 430 volcanic cones have been mapped with multibeam data used in this analysis and their morphology investigated. This number is certainly underestimated, as only about 45% of the Bassas da India/Europa region has been mapped by multibeam survey (Fig. 1c). The spatial distribution and shape of the cones are clearly non-random. Characteristics and distribution of the volcanic structures in this archipelago are given in Table 2 and described below.

Volcanic cones have mostly conical or conical-like forms with circular to elongate bases. A crater or a horseshoe-shaped crater have only been observed at the summit of less than 5% of the edifices (Figs 5 and 8). The basal area of individual volcanic cones ranges from 0.01 to 4.95 km^2 (Fig. 9a). The average basal area for volcanic cones around Ptolemee, PS1 and PS2 seamounts varies within a narrow range of between 0.92 and 1.2 km^2, whereas those in Hall and Jaguar Banks, Bassas da India and Europa region display smaller average values (0.24, 0.27, 0.49 and 0.54 km^2, respectively). Thus, the larger edifices are mainly located along the NW-SE volcanic alignment, from PS1 to Europa (Fig. 9a, 9d). Volcanic cone elevations range from 10 m to over 670 m (Fig. 9b) and almost 50% of cones are < 150 m in height. Only 2% of volcanic cones are > 500 m in relief and are mainly located on the northern part of Ptolemee seamount (Fig. 9b). In contrast, many small volcanic cones, with a height of < 100 m, are found on the volcanic ridge located between the eastern part of the Jaguar Bank and Bassas da India (Fig. 9b). The same tendency can be observed for average values. Average height is above 200 m for volcanic cones located around Ptolemee, PS1 and PS2 seamounts (230 m, 207 m and 280 m, respectively) whereas those around Hall and Jaguar Blanks, Bassas da India and Europa yield a smaller average height of 157 m, 124 m, 151 m and 158 m, respectively.

Aspect ratios (height/average base length) of the volcanic cones vary from 0.04 to 0.46 (Fig. 9c). Volcanic cones around Pamela Seamount 1 present the smaller average aspect ratio

of 0.18, whereas those located around Hall Bank display the highest (0.26 on average). With an average of 0.21, all of our results are in agreement with those obtained for scoria cones in many volcanic provinces such as the Comoros Archipelago (Tzevahirtzian et al. 2021), at Linosa (Romagnoli et al., 2020), Pico Island (Stretch et al., 2006; Mitchell et al., 2012), Terceira (Casalbore et al., 2015; Weiß et al., 2015), and higher than those in Canary (Mitchell et al., 2002) and Hawaii (Clague et al., 2000).

The mean slope distribution is presented in Figures 9d and 9e. 95% of mean slopes of the volcanic cones are < 25° (410/430), with 85% ranging from 10° to 25° (Fig. 9d). Less than 5% exceed 25°. Both small and large edifices can have mean slopes up to 20° (Fig. 9d). Moreover, small edifices with a basal area < 1 km^2 tend to present a large range of mean slopes varying from 4° to 29° (Fig. 9d). On the contrary, large edifices with a basal area of up to 2 km^2 are characterized by elevated mean slopes that are up to 15°. The distribution of the mean slopes is fairly unimodal, centered on 15 – 20° for Pamela Seamount 1 and Pamela Seamount 2 and on 20 – 25° for Bassas da India, Ptolemee and Europa, and Hall Bank (Fig. 9e). Jaguar Bank presents a larger range of distribution, with mean slopes between 10° and 25°. As for the mean slopes, the distribution of maximum slope is fairly unimodal with the most frequent slope being between 25° and 35° (Fig. 9f). Volcanic cones of Hall Bank, Ptolemee and Bassas da India display the most elevated maximum slopes, with angles of 30 – 35°. There appears to be a correlation between maximum slope and volcanic cone elevation. In fact, we observe a logarithmic increase of the maximum slope with height (Fig. 9g). Maximum slopes are found on high edifices, but we note that values rarely exceed 40° (Fig. 9g).

Directions of elongation have been obtained for each volcanic cone and plotted in Figure 9h. The distribution of directions of elongation is more or less bimodal. The most frequent direction ranges from 160 to 200°, while a second subset lies between 080 and 100°.

5) Discussion

a. Volcanic morphologies

The complex morphologies of volcanic edifices result from a long-term equilibrium between cyclic stages of growth and destruction (e.g., Mitchell et al., 2002). The landforms depicted on the submarine areas of the volcanic islands and seamounts are usually classified into two groups: landforms of volcanic origin and those derived from erosive-depositional

processes (Casalbore, 2018). Volcanic landforms primarily consist of volcanic cones, lava flows, calderas and craters, and areas of undifferentiated volcanic bedrock. Erosive-depositional landforms mainly result from channel erosion, gravity-driven instability and wave erosion.

In the Bassas da India/Europa complex, we describe several types of morphologies including large volcanic edifices topped by an atoll or a carbonate platform, volcanic seamounts, and volcanic ridges.

Large volcanic edifices with emerged or drowned carbonate platforms

The Bassas da India atoll and Europa island are the tops of volcanic edifices characterized by well-developed erosion systems, mainly consisting of numerous gullies and large channels, both active and inactive, some of which terminate in a lobe of deposits (Fig. 8e, f, and *Figs 3b and 9b in Count et al., 2018*). Only a few outcrops of the volcanic basement form relief that emerges from the sedimentary cover. Some are relatively well-developed, such as south of Bassas da India and northwest of Europa (Fig. 8e and f). Few individual volcanic cones were mapped on these edifices (Figs 5 and 8). The predominance of erosive-depositional processes for Bassas da India and Europa edifices results in smooth slopes that tend to become gentler towards the base, giving a slightly concave shape (Fig. 3a). This is particularly noticeable for Europa, which has the most concave slopes (Fig. 3a), reflecting significant spreading of sediments on the lower slopes and the nearby seafloor, controlled by gravity-driven instability (Counts et al., 2018).

Landslide scars are frequently visible around the submarine volcanoes of the Bassas da India/Europa complex (Jorry et al., 2016; Counts et al., 2018). They frequently originate at the edge of the carbonate platforms that exhibit scalloped margins (see Courgeon et al., 2016) and extend down to the volcanic slope of the seamounts, resulting in steep upper slope gradients where little sedimentation occurs. These scars participate to the destabilization and the progressive erosion of the volcanic slopes (Fig. 5). At Bassas da India, the presence of a large scar has induced an important asymmetry of the top of the volcanic edifice, which explains why the modern reef ring exhibits a scalloped margin along the northeastern part of the atoll. This process that creates scalloped margins may result in erosional deep-water carbonate basins and, potentially, the demise and disintegration of carbonate platforms on the long term, according to Mullins and Hine (1989).

Hall and Jaguar Banks also have many well-developed narrow gullies, canyons and channels mostly originating from steep landslide scars. Even if they are partly covered by a fine-grained sedimentation, characterised by low backscatter, the submarine slopes of these two seamounts have slighly more uneven relief compared to those of Bassas da India and Europa, with more frequent volcanic bedrock outcrops and volcanic cones, especially along the well-developed volcanic ridges. This difference in morphology (Fig. 3a) can be related to a greater contribution of sediment supply from coastal hydrodynamic processes (wind- or tide-generated water movement, shallow currents, or density cascading) for the emergent Bassas da India atoll and Europa Island, due to wave erosion, whereas Hall and Jaguar Banks lie at a depth of several hundred meters.

A potential difference in age of volcanism should also be considered. In the Comoros archipelago, Mayotte and Moheli display smooth slopes shaped by erosion-depositional processes, many small slope failures and channels and well-developed insular shelf and terraces. On the contrary, Grande Comore and Anjouan are characterized by submarine flanks shaped mainly by volcanism, with very narrow shelves and no submarine terraces. Based on these morphologies, Tzevahirtzian et al. (2021) suggested that Mayotte and Moheli are older than Grande Comore and Anjouan. Accordingly, we suggest that the existence of better-preserved volcanic morphologies on the flanks of the Hall and Jaguar Banks could reflect more recent volcanic activity than for Bassas da India and Europa. A structural component cannot, of course, be totally excluded as tectonics and rejuvenated volcanism are linked in the evolution of islands and drowned platforms (Courgeon et al, 2016).

Volcanic seamounts without carbonate platforms

The three volcanic seamounts not topped by a carbonate platform, namely Ptolemee, Pamela Seamount 1 (PS1) and Pamela Seamount 2 (PS2), exhibit remarkably well-preserved primary volcanic morphologies both at their tops and along the volcanic ridges (Figs 7 and 8). Unfortunately, the available data do not cover the summit of PS1. Despite this, we can clearly identify numerous volcanic cones and cone alignments on these three edifices. Ptolemee seamount is probably the most exceptional, with an impressive caldera and numerous volcanic cones, sometimes with a summit crater, within and around the caldera, and sharp volcanic ridges that develop radially from the caldera, extending south-southeastward toward Europa, north-northwestward, and eastward. The first two define a N155° alignment. Their morphologies allows us to compare them to rift zones like those described, for example, at

Lō‘ihi seamount, Hawaii (Fornari et al., 1988; Clague et al., 2019). These very well-preserved morphologies, with few signs of gravitational instability, and their higher backscatter compared to the surrounding sediment-covered seabed, are indicative of a relatively recent age for this volcanism.

Volcanic ridges

As noted for Ptolemee, the distribution of the volcanic cones does not appear to be random. Volcanic cones are located on the flanks of the main volcanic edifices (Bassas da India, Europa, Hall and Jaguar banks, Ptolemee and Pamela Seamounts 1 and 2), but mostly along volcanic ridges. Volcanic ridges have been identified E of Hall Bank, NE of Jaguar Bank, SSW and E of Bassas da India atoll, SSE, E and W of Ptolemee seamount, and SSE and E Pamela Seamount 1 (Figs 2, 5, 7, and 8). Furthermore, Jaguar Bank has a clearly elongated shape along a SE-NW orientation, with its northwest and southeast flanks characterized by a high acoustic backscatter and numerous elongated volcanic cones (Figs 2 and 5). This elongated shape could also reflect the existence of a volcanic ridge with a N150° orientation.

The volcanic ridges constitute elongated topographic highs with numerous volcanic cones and areas of high backscatter signal that can indicate extensive lava flows not covered by significant marine sedimentation. As noted above, the volcanic ridges have average along-axis slopes of between 11° (E of Hall Bank, E of Bassas da India) and 4° (NE of Jaguar Bank, SSE of Ptolemee seamount, E of Pamela Seamount 1). They often show a higher slope at shallower water depths, close to the atoll or carbonate bank or top of the seamount, except for the NE ridge of Jaguar Bank which has a slightly convex profile (Figs 3b and 7b). We also noted that the volcanic ridges of the Hall Bank, Jaguar Bank and Bassas da India often coincide with fault networks running along the ridge axis. They are also more evenly shaped and rise more prominently from the surrounding seafloor than those of Ptolemee seamount and Pamela Seamount 1 (Fig. 3b).

The elongation and width of the volcanic ridges, the regularly plunging along-strike slope from the top of the main volcanic center (Figs 3, 5, 7 and 8), and the high concentration of volcanic cones and faults, leads us to compare them to the rift zones described for shield volcanoes (MacDonald, 1972). Volcanic rift zones are preferential pathways for intrusive/extrusive activity, resulting in narrow elongated ridges. The morphology of the rift zones of shield volcanoes is a valuable indicator of the processes that can be responsible for their construction (e.g., Harpp et al., 2003). The length and width of a rift zone, as well as

along-axis slope, is directly controlled by the capability of magma to migrate laterally under magmatic driving pressure (Dieterich, 1988; Fialko and Rubin, 1999). The changes in slope along the rift axis and the regularity of the slope make it possible to assess the continuity of the intrusive dyke system and the constancy of magma supply (Angevine et al., 1984; Harpp et al., 2003). The slope values of the identified volcanic ridges (Table 3) are similar to those obtained for the offshore section of the rift-zones of Hawaiian volcanoes (Mark and Moore, 1987; Fornari et al., 1988; Lonsdale, 1989; Clague et al., 2019), Canary Islands (Gee et al., 2001; Mitchell et al., 2002; Acosta et al., 2003b), Galapagos Islands (Harpp et al., 2003; Geist et al., 2006, 2008), and Grande Comore Island (Tzevahirtzian et al., 2021).

However, there are significant differences to typical Hawaiian rift zones such as Puna Ridge (Smith et al., 2002) or Hilo Ridge (Lipman and Calvert, 2011). Rift zones in the Bassas da India-Europa complex are less long (less than 30 km) than those of the Hawaiian volcanoes, and their morphology is more discontinuous. Such differences have already been reported for some rift zones in the Canary Islands (Acosta et al., 2003b) and the Galapagos Islands (Harpp et al., 2003). In the Bassas da India/Europa complex, most of the volcanic ridges have uneven relief with significant slope reversals due to the presence of large volcanic cones. At or near the end of volcanic ridges, large volcanic cones frequently dominate the landforms, and can even occur in isolation on the seafloor within the axis of the ridge, as noted for example for the SSE ridge of Ptolemee seamount.

Such differences can be related to magmatic driving pressure and magma supply rate. For Acosta et al. (2003b), the magma supply rate on La Palma and El Hierro is too low to smooth out the topographic irregularities along the rift zone axis, explaining the morphological differences to Hawaiian rift zones. According to Harpp et al. (2003), short rift zones with uneven relief suggest that magma input into the rift is sporadic and reflects low magmatic driving pressure that decreases progressively with distance as magma migrates laterally from a shallow magma chamber.

A low magma supply rate from a shallow magma chamber fits well with the morphologies of the proximal rift zone sections of the volcanoes of the Bassas da India-Europa complex. However, this does not appear to be consistent with the presence of numerous large volcanic cones in the distal sector of these rift zones. The presence of large volcanic cones in these areas suggests that they were fed by a poorly degassed magma from a deep reservoir, similarly to the current eruption offshore Mayotte (Berthod et al., 2021a; Feuillet et al., 2021). It therefore seems necessary to consider the coexistence of two different

scenarios to explain the feeding of the eruptions that built the volcanic rifts (Fig. 10): (i) Lateral injection of magma from a shallow magma chamber located under the main volcanic center mainly feeding eruptions in the proximal section of the rift zones, and (ii) direct magma injections from a deeper storage zone feeding the large volcanic cones in the distal section of the rift zones, or, occasionally, at higher altitude. In both cases, magma injections follow the same weakness zones, at least near-surface, determining the rift zone's orientation.

Volcanic cones

Four hundred and thirty volcanic cones have been identified on the flanks of the seven major volcanic edifices and along the volcanic ridges (Figs. 2, 5 and 8). Each individual volcanic cone, showing a relatively simple shape, is inferred to be the result of a unique eruption. They are interpreted as monogenetic volcanic edifices formed by pyroclastic rock fragments and/or low effusion rate lava flows (pillow lava). Some of them have an elongated shape or form alignments of cones that represent the trace of a dyke intrusion and a linear eruptive fissure. Physical and chemical properties such as effusive rate, cooling rate, magma composition, viscosity or volatiles content, and the pre-eruptive topography and the water depth also control the shape of volcanic cones in the submarine realm (Bonatti and Harrison, 1988; Fink and Griffiths, 1990; Rappaport et al., 1997 ; Gregg and Fink, 2000). Our mapping does not allow us to establish the role of each of these parameters. Nevertheless, we note that volcanic cones of the Bassas da India/Europa complex are characterized by high aspect ratios (0.21 in average, Fig. 9c) and high slope values, which can reach 40° (Fig. 9f). These morphological characteristics are steeper than those found for worldwide seamounts (Mukhopadhyay and Khadge, 1990; Mukhopadhyay and Batiza, 1994; Rappaport et al., 1997; Clague and Dixon, 2000, Clague et al., 2000; Rowden et al., 2005; Stretch et al., 2006; Mitchell et al., 2012, 2002; Casalbore et al., 2015; Weiß et al., 2015; Romagnoli et al., 2020; Tzevahirtzian et al., 2021). This may be due to low effusion rates favoring in-situ accumulation of pillow lavas and pyroclasts, rather than large sheet flows (Rubin et al., 2012), or higher magma viscosity. It is generally accepted that increasing silica content leads to an increase in viscosity of melts (Liebske et al., 2003; Bouhifd et al., 2004; Stabile et al., 2016). Volcanic rocks of the Bassas da India/Europa complex are composed of alkali mafic lavas with low silica content (olivine basalts to nephelinites; Courgeon et al., 2017). Some authors suggest that alkali basalts are slightly more viscous than tholeiites (Acosta et al., 2003b; Chevrel et al., 2014), which could be consistent with the observed high slope values.

b. **Chronology**

Previously, little was known about magmatic activity in the southern Mozambique Channel and only a few indirect ages have been obtained for Bassas da India, Hall Bank and Jaguar Bank (Courgeon et al., 2016, 2017). These authors showed that the oldest shallow-water carbonate of Hall Bank is Burdigalian in age (i.e., 16.3 ± 0.1 Ma) suggesting that the underlying volcanic units are older than the Late Oligocene to Early Miocene. As we obtained $^{40}Ar/^{39}Ar$ plateau ages of 20.5 ± 1.5 and 20.2 ± 0.1 Ma (Early Miocene) on MOZ01-DW05-01 and MOZ01-DW05-13 volcanic samples, respectively (Fig. 6), our geochronological data suggest that the dated samples may indeed belong to the Hall Bank volcanic basement. However, these samples correspond to loose volcanic fragments that were collected by dredging at the top of the youngest carbonate platform of Hall Bank (Fig. 1c). Courgeon et al. (2017) showed that the carbonate platform was affected by several late explosive and effusive eruptions, as evidenced by the presence of volcanic craters and lava flows on the top of the platform. The volcaniclastic deposits dredged from the top of Hall Bank and the very well-preserved crater morphology imply a phreatomagmatic eruption affecting the Hall Bank carbonate platform during the Pleistocene (Courgeon et al., 2017). Therefore, we can deduce that our rocks, dated at about 20 Ma, could correspond to fragments of the deep volcanic basement, brought up by this recent explosive eruption.

The lava sample collected from the northeast volcanic ridge of Jaguar provided an $^{40}Ar/^{39}Ar$ plateau age of 9.6 ± 0.2 Ma. This age is close to previous ages obtained for a packstone sample collected along the southern flank of the Jaguar Bank carbonate platform (11.45 ± 0.37 Ma, strontium isotopic stratigraphy, after Courgeon et al., 2017). This indicates that the volcanism contributing to the building of this submarine ridge occurred synchronously with, or shortly after, the growth of the carbonate platform. Similarly, the volcanic rock dated for Bassas da India comes from the submarine ridge extending southwest of the atoll. The $^{40}Ar/^{39}Ar$ plateau and isochron ages of 8.0 ± 0.2 Ma obtained for this sample (Fig. 6) is also very close to that obtained for the drowned carbonate terraces south of Bassas da India (8.48 ± 0.49 Ma - strontium isotopic stratigraphy on a packstone) by Courgeon et al. (2016, 2017). These data all show that, while the major phase of building of the volcanic edifices occurred up to the Early Miocene, volcanism resumed and continued during and after carbonate platform growth, during Late Miocene to Pliocene times, and probably until the Pleistocene.

Though we do not have a direct age for the seamounts located between Bassas da India and Europa (Ptolemee seamount, Pamela Seamounts 1 and 2), their very well-preserved morphology, with perfectly identifiable volcanic structures, argues for a relatively recent activity, probably of Pliocene-Pleistocene age.

Thus, from our $^{40}Ar/^{39}Ar$ data, and following Courgeon et al. (2016, 2017), we can state that, while the main building phases of the seamounts of the Bassas da India/Europa complex are Oligocene to Early Miocene in age (> 20 Ma), volcanism resumed and continued during and after the growth of the carbonate platforms, until the Late Miocene (8 – 10 Ma) and probably more recently (until the Pleistocene - see Courgeon et al, 2017), along the volcanic ridges and on drowned carbonate platforms.

The volcanism on the Bassas da India/Europa complex is similar in age to the Miocene Rungwe Volcanic Province located in the southern part of the Western branch of the East African Rift, in Tanzania (Fig. 1a, Mesko et al., 2014), and the Neogene Comoros volcanism in the northern entrance of the Mozambique Channel (Debeuf, 2009; Pelleter et al., 2014; Michon et al., 2016; Quidelleur et al. 2022). These results, together with the ages (6 - 7 Ma) obtained by O'Connor et al. (2019) for the young Mozambique Ridge volcanism, are in line with what would be expected for the southward migration of the East African Rift System and related magmatism. Petrological and geochemical studies are still needed to support and confirm this relationship.

c. Relationship between tectonics and volcanism

Linear volcanic ridges, elongated volcanic cones and alignments of cones are often used as tectonic markers of the near-field stress, or can be seen as the result of magma emplacement into a pre-existing damaged lithosphere (Tibaldi, 1995 ; Michon et al., 2007; Navarro et al., 2009). Previous structural studies in the southern Mozambique Channel, by Courgeon et al. (2016; 2017) and Deville et al. (2018), described a dense network of faults with a dominant N45 – 80° orientation in the areas of Hall Bank, Jaguar Bank and Bassas da India atoll (Figs 2, 5 and 10) and further south-west, whereas faults with a N160 – 180° orientation are predominant north of Bassas da India and in the Davie Ridge area. Drowned carbonate platforms and the recent volcanic units of Hall and Jaguar Banks are clearly affected by N45 – 80° normal faults (Fig. 5b, d), indicating that some of them are probably active and contemporaneous with the most recent volcanic events (Courgeon et al., 2017). Based on the interpretation of seismic profiles, Deville et al. (2018) deduce that the period of

faulting lasted from late Miocene to the present-day, pointing out that the most recent faults affect the entire sedimentary cover and are clearly expressed in the topography of the seafloor. They deduce that faults were active during the Quaternary and were probably contemporaneous with the most recent volcanism.

Our own observations confirm that N45 – 80° faults are widespread in the area from Bassas da India to Hall Bank, whereas very few faults are observed between Pamela Seamount 1 and Europa Island (Figs 2 and 8). These faults vary in length and can reach up to several kilometers. In many places the faults crosscut the seamounts and volcanic deposits (Figs 4b-d and 8a, b). But locally they can be masked by volcanic deposits, in particular by some of the volcanic cones (Figs 4, 5, and 8a, b), thus supporting the contemporaneity of volcanism and tectonics. If we consider the overall pattern of the main volcanic edifices and ridges, there are two clear alignments (Fig. 11). Between Hall Bank and Bassas da India, the volcanic features are organized according to an overall NE-SW orientation (hereafter called the NE-SW trend), whereas the volcanic features between Bassas da India and Europa are mainly aligned according to a global NW-SE orientation (the NW-SE trend).

The NE-SW trend is characterized by two flat-topped seamounts (Hall and Jaguar Banks) with a carbonate platform currently at a depth of several hundred meters, and a large volcanic edifice now topped by an atoll (Bassas da India). Volcanic ridges that we interpret as rift zones dominate the submarine morphology of all these volcanic edifices. They develop mainly along the overall NE-SW orientation of the trend, but Jaguar bank also shows a ~N150° elongation, similar to the orientation of the NW-SE trend. Statistical analysis of the volcanic cones along this NE-SW trend show that they have small basal areas, and are low in elevation (Fig. 11a, b). More than 60% are < 150 m high and 95% have a surface ranging from 0.02 to 1 km^2 (Fig. 11c, d).

Along the NW-SE trend, between Bassas da India and Europa, three large seamounts have been discovered, including Ptolemee seamount, the two largest having well-developed rift zones with an orientation parallel to the NW-SE trend, and shorter rift zones following an ENE-WSW orientation. Numerous isolated volcanic cones, mainly located along the extension of the southern rift zones, characterize the area between the edifices. (Figs 2, 8 and 10). These volcanic cones are, on average, larger and higher than those located in the NE-SW trend (Fig. 11). Indeed, 81.8% of the > 2 km^2 volcanic cones are located on this trend (Fig. 11c) and 58.7 % of the volcanic cones are > 150 m in height (Fig. 11d).

In summary, several observations can be made:

(1) The NE-SW trend is characterized by large volcanic edifices topped by carbonate platforms with well-developed polygenetic rift zones making up long, wide and high landforms associated with numerous small volcanic cones

(2) The NW-SE trend includes seamounts with volcanic ridges that are lower in relief but have larger volcanic cones.

(3) The orientation of the rift zones, or volcanic ridges, close to the dominant NE-SW and NW-SE orientations, indicates that their development was influenced by the general regional tectonic stress field or by inherited structures in the lithosphere.

This difference in morphology, controlled by the magmatic activity, suggests a higher magma supply rate along the NE-SW trend, through a better expressed network of faults, leading to the growth of well-developed volcanic ridges.

d. **Magma supply, and magma feeding system.**

The long-term magma supply rate for the Bassas da India/Europa volcanism can be approximated from the area occupied by volcanic formations on the seafloor. Assuming a uniform crustal thickness of 6 km (Leinweber et al., 2013), the total volume of all volcanic edifices represents 4% of the total crustal volume over the 27,900 km^2 study area. The seamount and volcanic cone basal areas cover 5,905 km^2, which represents a minimum of 21% of the seafloor. Comparable values have been obtained from the Canary archipelago volcanism, at 7,273 km^2 (Acosta et al., 2003b), whereas it represents 56 % of the area for the island of Hawaii (10,458 km^2, Acosta et al., 2003a). This difference in the area covered by volcanic products of these archipelagoes is interpreted as being due to a weaker magma supply for Canary and Bassas da India/Europa archipelagos than for Hawaii, leading to a low effusive rate and sporadic eruptions, in good agreement with the alkaline nature of the volcanism.

It is challenging to obtain information on the geometry of magma supply and storage systems from the morphology of the volcanic edifices and the spatial distribution of the magma vents alone (Tibaldi, 2015). The magma feeding system is often complex, including multiple levels of magma storage from which magma can be drained into rift zones. The depth and geometry of the magma reservoir(s) beneath a volcano is likely to be a result of the combined effects of the stress field, the magma supply rate which determines thermal conditions, and the density structure beneath and within the volcanic edifice. The Bassas da

India/Europa complex comprises both central, or shield, volcanoes and diverging elongated volcanic ridges. Hall Bank, Jaguar Bank, Bassas da India and Europa are large central volcanoes rising more than 2000 m from the surrounding seafloor (Fig. 3a). The two newly discovered seamounts (PS1 and PS2) and Ptolemee seamount, between Bassas da India and Europa, are smaller, but rise 900 m, 1500 m and 2000 m above the surrounding seabed, respectively. The volcanic ridges originating from these central volcanoes form reliefs several hundred meters high, regularly plunging along-strike from the main volcanic center (Fig. 3b). The volcanic cones around these seven volcanic edifices are most likely monogenetic cones, ranging in height from > 10 to 665 m (Fig. 9a, b). They have been mapped mainly along the ridges, but also off-ridge, on the flanks of the seamounts. Such geomorphological patterns are not unique to the Bassas da India/Europa complex. They are strongly reminiscent of the morphology of other oceanic volcanoes, such as Lō'ihi, Hawaii Islands (Fornari et al., 1988; Clague et al., 2019), Canary Islands (Acosta et al., 2003a; Llanes et al., 2009), Comoros Islands (Tzevahirtzian et al., 2021), Galapagos Islands (Harpp et al., 2003; Geist et al., 2006; Glass et al., 2007) and the Azores (Romer et al., 2018). The similarities in volcanic morphology between these islands and seamounts suggest similar modes of formation, involving long-term building of central volcanoes and magma injections into rift zones from shallow magma reservoir.

We show that volcanic products of the Bassas da India/Europa complex are associated with faults contemporaneous with volcanism, which probably favor magma ascent. The largest volcanic edifices appear to be located at the intersection of fault zones affecting the oceanic lithosphere (Figs 2, 3a, d and 8c, d). This fracturing in the lithosphere has probably played an important role in the construction and the dimension of volcanic edifices, facilitating the ascent and storage of magma, and thus the construction of polygenetic edifices that can last several million years. In the northern part of the Mozambique basin, investigation of seismic refraction data along profiles across the Mozambican margin (20140010 profile, Mueller and Jokat, 2017) located the crust-mantle boundary at a depth of about 15 km. Therefore, it seems reasonable to suggest that deep magma reservoirs might be located at this crust-mantle boundary (Fig. 10), as magmatic underplating beneath the oceanic crust is commonly associated with intraplate volcanism (e.g., Charvis et al., 1999; Fullea et al., 2015; Merz et al., 2019). After initial eruptions of basic magmas and increasing edifice load, magma would be stored in shallower reservoirs. Moderate to shallow depth magma chambers can have existed within the crust when the magma supply rate was high enough to provide

suitable thermal conditions. The morphology of the rift zones is an indicator of the existence of such high-level magma storage, at least during the main period of growth of Bassas da India and Jaguar Bank, allowing magma to be emplaced laterally from a shallow magma chamber into the rift zones. In contrast, the largest volcanic cones probably result from subvertical magma ascent from the mantle through the crust, bypassing the shallower storage zones.

We suggest that the well-developed NE-SW trends (Bassas da India - Jaguar Bank - Hall Bank, Figs 1c and 11) might result from long-lasting magmatic activity or high magma transfer rate, with volcanic shields being able to build rift zones fed by lateral transfer of magma from a storage system situated beneath the main shield. In contrast, the NW-SE trend (between Bassas da India and Europa Island, Figs 2 and 11), with seamounts and volcanic ridges whose morphology reveals the presence of many large monogenetic volcanic cones, might represent less mature stage of growth, with more frequent deep magma injections and rapid magma ascent.

e. Integration in the geodynamic evolution of the Mozambique Channel

Our study demonstrates that magma ascent is strongly controlled by large pre-existing crustal structures as shown, at different scales, by the NE-SW and NW-SE alignment of the main volcanic edifices (Figs 2, 10 and 11), the orientation of the volcanic ridges and faults, the alignment of the volcanic cones and the shape of the elongated cones. We suggest that these large pre-existing crustal structures controlling magma ascent correspond to the fault zones affecting the oceanic lithosphere of the Mozambique Basin, active since at least the Late Miocene, described by Deville et al. (2018). The NE-SW fault trend, parallel to the magnetic anomalies of the oceanic crust (Fig. 1a, König and Jokat, 2010; Leinweber and Jokat, 2012; Mueller and Jokat, 2017), corresponds to the still active Quathlamba seismic axis (Hartnady, 1990), related to southward movement of the Lwandle block relative to the Rovuma block (Saria et al., 2014). The NW-SE volcanic alignments in our study area show orientations close to the N160-180° fractures predominant to the north of Bassa da India (Deville et al., 2018), and probably controlled by the Davie Ridge system and the transform fracture zones affecting the Mozambique Basin (König and Jokat, 2010; Leinweber & Jokat, 2012).

Many authors consider the structures currently active in the Mozambique Channel as related to the progressive southward extension of the East African Rift System since the Oligocene (e.g. Mougenot et al., 1986; Kusky et al. 2010; Franke et al., 2015; MacGregor, 2015; Michon, 2016; Courgeon et al., 2018; Deville et al., 2018; O'Connor et al. 2019; Famin et al., 2020; Wiles et al., 2020; Vormann and Jokat, 2021b). The correlation between fault systems and earthquake epicenters is used by Deville et al. (2018) to suggest that the tectonically active zones in the Mozambique Channel, including the Davie Ridge, are directly connected to the eastern branch of the East African Rift System.

The Cenozoic volcanic systems within and around the Mozambique Channel (including Madagascar and the Mozambique Ridge) raise the question of their possible link with a southward extension of the East African Rift System (Breitzke et al., 2017; Dorschel et al., 2018; Deville et al., 2018; Courgeon et al., 2018; Wiles et al., 2020). For the Bassas da India/Europa complex, the coexistence of active fault systems and Oligo-Miocene to Pleistocene age volcanism argues for such a relationship. Such a context, where Neogene eruptive episodes are contemporaneous with tectonic activity, is reminiscent of others EARS-related settings such as the Comoros archipelago (Feuillet et al., 2021; Tzevahirtzian et al., 2021) or the Miocene Rungwe Volcanic Province in the southern part of the Western Rift in Tanzania (Fig. 1a, Mesko et al., 2014). Geochemical and petrological data on the dredged rocks collected during the PAMELA-MOZ01 (Olu, 2014) and PAMELA-MOZ04 (Jouet and Deville, 2015) cruises will provide more information on the origin of the magma, and the potential connection of this volcanism with the East African Rift System (Berthod et al. in preparation) and the superplume mantle tracked isotopically along Africa from from the Red Sea to the Indian Ocean (O'Connor et al., 2019).

6) Conclusion

New bathymetric mapping in the Bassas da India/Europa region in the Mozambique Channel, acquired during the 2014 PAMELA-MOZ1 and the 2015 PAMELA-MOZ04 cruises, provide new constraints on the Cenozoic volcanism emplaced on the surrounding seafloor. Our comprehensive geomorphological survey of the Bassas da India/Europa complex has enabled us to describe the underwater volcanic morphology of Bassas da India and Europa, and the Hall Bank, Jaguar Bank and Ptolemee seamounts. In addition, we discovered and described two new large edifices located immediately to the south of Bassas

da India and rising more than 900 m and 1500 m respectively, named here Pamela Seamount 1 and Pamela seamount 2. $^{40}Ar/^{39}Ar$ ages obtained for a number of dredged samples from lava flows together with data from the literature confirm that this volcanism covers a period from the Oligo-Miocene to the Pleistocene, and probably extends to the present day. The main building phases of the seamounts of the Bassas da India/Europa complex are Oligocene to Early Miocene in age (> 20 Ma). But volcanism continued during and after the growth of carbonate platforms on top of the main volcanic edifices, until the Late Miocene (8 – 10 Ma) and probably more recently, along the volcanic ridges and on drowned carbonate platforms as well.

Bathymetry and acoustic backscatter images clearly show that these volcanoes have volcanic ridges forming landforms whose orientations appear to be strongly controlled by regional tectonics. The morphology of these ridges and the presence of volcanic cones and faults indicate that they are volcanic rift zones, typical of many oceanic shield volcanoes. However, the presence of large volcanic cones along these volcanic ridges leads us to deduce the involvement of at least two levels of magma storage feeding these structures. The morphology of the rift zones is consistent with the existence of shallow magma storage zones, allowing magma to intrude laterally into the rift zones to feed fissure eruptions and building small volcanic cones and lava flows. In contrast, we suggest that the large volcanic cones are more likely to be the result of sporadic subvertical ascent of magma from a deep reservoir located in the mantle or at the base of the crust, bypassing more superficial storage areas.

The distribution and features of the main volcanoes, the orientation and differences in morphology of the volcanic ridges, and the morphological properties of the 430 volcanic cones identified, allowed us to characterize the two main trends, NE-SW and NW-SE, which are linked to structural features in the region. The NE-SW trend, with volcanic edifices topped by carbonate platforms and well-developed polygenetic rift zones, might result from long-term magmatic activity or a high magma transfer rate. The NW-SE trend that includes seamounts with less-developed volcanic ridges but larger volcanic cones, might represent a less mature stage of growth, with more frequent deep magma injections and rapid magma ascent. For both trends, the orientation of the rift zones, or volcanic ridges, close to the dominant NE-SW and NW-SE orientations, indicates that their development was influenced by the overall regional tectonic stress field or by inherited structures in the lithosphere.

Indeed, the Bassas da India/Europa complex is located on the Quathlamba seismic axis and on the Rovuma-Lwandle boundary characterized by the two main strikes of lithospheric

faults of N45 – 80° and N160 – 180°. Thus, all of these results converge toward a model in which magma ascent is strongly controlled by large pre-existing crustal structures associated with the opening of the Mozambique Basin and the movement of the Davie ridge, formed as a consequence of the breakup of Gondwana, and of the ongoing southward propagation of the East African Rift System. This potential link to the present-day kinematics of the East African Rift System and a possible superplume beneath southern Africa needs to be confirmed with geochemical and petrological data of the dredged rocks.

Acknowledgments

This work is part of the PAMELA (Passive Margin Exploration Laboratory) research project. This research was co-funded by TOTAL and IFREMER as a part of the PAMELA (Passive Margin Exploration Laboratories) scientific project. The authors would like to thank Frances van Wyk de Vries for her review of the English grammar. This is Laboratory of Excellence ClerVolc contribution number XXX.

References

Acosta, J., Uchupi, E., Muñoz, A., Herranz, P., Palomo, C., Ballesteros, M., Group, Z.E.E.W., 2003a. Geologic evolution of the Canarian Islands of Lanzarote, Fuerteventura, Gran Canaria and La Gomera and comparison of landslides at these islands with those at Tenerife, La Palma and El Hierro. Geophys. Canar. Islands 1–40. https://doi.org/10.1007/s11001-004-1513-3

Acosta, J., Uchupi, E., Smith, D., Muñoz, A., Herranz, P., Palomo, C., Llanes, P., Ballesteros, M., Group, Z.E.E.W., 2003b. Comparison of volcanic rifts on La Palma and El Hierro, Canary Islands and the island of Hawaii. Geophys. Canar. Islands 59–90. https://doi.org/10.1007/s11001-004-1162-6.

Angevine, C.L., Turcotte, D.L., Ockendon, J.R., 1984. Geometrical form of aseismic ridges, volcanoes, and seamounts. J. Geophys. Res. Solid Earth 89, 11287–11292. https://doi.org/10.1029/JB089iB13p11287

Baby, G., Guillocheau, F., Braun, J., Robin, C., Dall'Asta, M., 2020. Solid sedimentation rates history of the Southern African continental margins: Implications for the uplift history of the South African Plateau. Terra Nova, 32(1), 53-65.

Bachèlery, P., Morin, J., Villeneuve, N., Soulé, H., Nassor, H., Ali, A.R., 2016. Structure and eruptive history of Karthala volcano, in: Active Volcanoes of the Southwest Indian

Ocean. Springer, pp. 345–366.

Bassias, Y., 1992. Petrological and geochemical investigation of rocks from the Davie Fracture Zone (Mozambique Channel) and some tectonic implications. J. African Earth Sci. (and Middle East) 15, 321–339. https://doi.org/10.1016/0899-5362(92)90018-8

Bassias, Y., & Bertagne, R., 2015. Study updates uplift-erosion correlation, Davie fracture zone. Oil & Gas Journal, 113(9), 64-75.

Bassias, Y., & Leclaire, L., 1990. The Davie Ridge in the Mozambique Channel: Crystalline basement and intraplate magmatism. Neues Jahrbuch für Geologie und Paläontologie-Monatshefte, 67-90.

Ben Avraham, Z., Hartnady, C.J.H., Le Roex, A.P., 1995. Neotectonic activity on continental fragments on the Southwest Indian Ocean: Agulhas Plateau and Mozambique Ridge. J. Geophys. Res. 100, 6199–6211. https://doi.org/10.1029/94JB02881

Bernard, A., Munschy, M., Rotstein, Y., & Sauter, D., 2005. Refined spreading history at the Southwest Indian Ridge for the last 96 Ma, with the aid of satellite gravity data. Geophysical Journal International, 162(3), 765-778.

Berthod C, Médard E, Bachèlery P, Gurioli L, Di Muro A, Peltier A, Komorowski J, Benbakkar M, Devidal J, Langlade J, Besson P, Boudon G, Rose-Koga E, Deplus C, Le Friant A, Bickert M, Nowak S, Thinon I, Burckel P, Hidalgo S, Jorry S, Fouquet Y, Feuillet N (2021) The 2018-ongoing Mayotte submarine erup- tion: magma migration imaged by petrological monitoring. Earth Planet Sci Lett 571:117085. https:// doi. org/ 10. 1016/j. epsl. 2021. 117085

Berthod, C., Zaragosi, S., Famin, V., 2021b. SCRATCH cruise : Sampling in the Comoros Region: Anthropization, Tectonics, volcanism, and Climate Hypotheses, NV Marion Dufresne II. https://doi.org/10.17600/18002274

Bonatti, E., Harrison, C.G.A., 1988. Eruption styles of basalt in oceanic spreading ridges and seamounts: Effect of magma temperature and viscosity. J. Geophys. Res. Solid Earth 93, 2967–2980. https://doi.org/10.1029/JB093iB04p02967

Bouchard, C., Crumplin, W., 2011. Two faces of France:'France of the Indian Ocean'/'France in the Indian Ocean.' J. Indian Ocean Reg. 7, 161–182. https://doi.org/10.1080/19480881.2011.637423

Bouhifd, M.A., Richet, P., Besson, P., Roskosz, M., Ingrin, J., 2004. Redox state, microstructure and viscosity of a partially crystallized basalt melt. Earth Planet. Sci. Lett. 218, 31–44. https://doi.org/10.1016/S0012-821X(03)00641-1

Breitzke, M., Wiles, E., Krocker, R., Watkeys, M.K., Jokat, W., 2017. Seafloor morphology in the Mozambique Channel: evidence for long-term persistent bottom-current flow and deep-reaching eddy activity. Mar. Geophys. Res. 38, 241–269. https://doi.org/10.1007/s11001-017-9322-7

Calais, E., Hartnady, C., Ebinger, C., Nocquet, J.M., 2006. Kinematics of the East African Rift from GPS and earthquake slip vector data. In: Yirgu, G., Ebinger, C.J., Maguire, P.K.H. (Eds.), Structure and Evolution of the Rift Systems Within the Afar Volcanic Province, Northeast Africa. In: Geol. Soc. (Lond.) Spec. Publ., vol. 259, pp. 9–22.

Casalbore, D., 2018. Volcanic islands and seamounts, in: Submarine Geomorphology. Springer, pp. 333–347. https://doi.org/10.1007/978-3-319-57852-1_17

Casalbore, D., Romagnoli, C., Pimentel, A., Quartau, R., Casas, D., Ercilla, G., Hipólito, A., Sposato, A., Chiocci, F.L., 2015. Volcanic, tectonic and mass-wasting processes offshore Terceira Island (Azores) revealed by high-resolution seafloor mapping. Bull. Volcanol. 77, 24. https://doi.org/10.1007/s00445-015-0905-3

Castelino, J. A., Eagles, G., Jokat, W., 2016. Anomalous bathymetry and palaeobathymetric models of the Mozambique Basin and Riiser-Larsen Sea. Earth and Planetary Science Letters, 455, 25-37. https://doi.org/10.1016/j.epsl.2016.09.018

Cesca, S., Letort, J., Razafindrakoto, H.N.T., Heimann, S., Rivalta, E., Isken, M.P., Nikkhoo, M., Passarelli, L., Petersen, G.M., Cotton, F., Dahm, T., 2020. Drainage of a deep magma reservoir near Mayotte inferred from seismicity and deformation. Nat. Geosci. 13, 87–93. https://doi.org/10.1038/s41561-019-0505-5

Charvis, P., Laesanpura, A., Gallart, J., A., H., Lépine, J.-C., de Voogd, B., Minshull, T., Hello, Y., Pontoise, B., 1999. Spatial distribution of hotspot material added to the lithosphere under La Reunion, from wide-angle seismic data. J. Geophys. Res. 104, 2875–2893. https://doi.org/10.1029/98JB02841

Chevrel, M.O., Baratoux, D., Hess, K.-U., Dingwell, D.B., 2014. Viscous flow behavior of tholeiitic and alkaline Fe-rich martian basalts. Geochim. Cosmochim. Acta 124, 348–365. https://doi.org/10.1016/j.gca.2013.08.026

Chorowicz, J., 2005. The east African rift system. J. African Earth Sci. 43, 379–410. https://doi.org/10.1016/j.jafrearsci.2005.07.019

Clague, D.A., Paduan, J.B., Caress, D.W., Moyer, C.L., Glazer, B.T., Yoerger, D.R., 2019. Structure of Lō ʻihi Seamount, Hawai ʻi and Lava Flow Morphology From High-Resolution Mapping. Front. Earth Sci. 7, 58. https://doi.org/10.3389/feart.2019.00058

Clague, D.A., Dixon, J.E., 2000. Extrinsic controls on the evolution of Hawaiian ocean island volcanoes. Geochemistry, Geophys. Geosystems 1. https://doi.org/10.1029/1999GC000023

Class, C., Goldstein, S.L., Altherr, R., Bachèlery, P., 1998. The process of plume–lithosphere interactions in the ocean basins—the case of Grande Comore. J. Petrol. 39, 881–903. https://doi.org/doi.org/10.1093/petroj/39.5.881

Coffin, M.F., Rabinowitz, P.D., 1987. Reconstruction of Madagascar and Africa: evidence from the Davie fracture zone and western Somali basin. J. Geophys. Res. Solid Earth 92, 9385–9406. https://doi.org/10.1029/JB092iB09p09385

Counts, J.W., Jorry, S.J., Leroux, E., Miramontes, E., Jouet, G., 2018. Sedimentation adjacent to atolls and volcano-cored carbonate platforms in the Mozambique Channel (SW Indian Ocean). Mar. Geol. 404, 41–59. https://doi.org/10.1016/j.margeo.2018.07.003

Courgeon, S., 2017. Cenozoic evolution of isolated carbonate platforms from the Mozambique Channel (SW Indian Ocean): development and controls in active geodynamic settings. Aix-Marseille.

Courgeon, S., Bachèlery, P., Jouet, G., Jorry, S.J., Bou, E., BouDagher-Fadel, M.K., Révillon, S., Camoin, G., Poli, E., 2018. The offshore east African rift system: new insights from the Sakalaves seamounts (Davie Ridge, SW Indian Ocean). Terra Nov. 30, 380–388. https://doi.org/10.1111/ter.12353

Courgeon, S., Jorry, S.J., Jouet, G., Camoin, G., BouDagher-Fadel, M.K., Bachèlery, P., Caline, B., Boichard, R., Revillon, S., Thomas, Y., 2017. Impact of tectonic and volcanism on the Neogene evolution of isolated carbonate platforms (SW Indian Ocean). Sediment. Geol. 355, 114–131. https://doi.org/10.1016/j.sedgeo.2017.04.008

Courgeon, S., Jorry, S.J., Camoin, G.F., BouDagher-Fadel, M.K., Jouet, G., Révillon, S., Bachèlery, P., Pelleter, E., Borgomano, J., Poli, E., 2016. Growth and demise of Cenozoic isolated carbonate platforms: New insights from the Mozambique Channel seamounts (SW Indian Ocean). Mar. Geol. 380, 90–105. https://doi.org/10.1016/j.margeo.2016.07.006

Cox, K.G., 1992. Karoo igneous activity, and the early stages of the break-up of Gondwanaland. Geol. Soc. London, Spec. Publ. 68, 137–148. https://doi.org/10.1144/GSL.SP.1992.068.01.09

Crisp JA 1984 Rates of magma emplacement and volcanic output. J Volcanol Geotherm Res 20:177–211. https://doi.org/10.1016/0377-0273(84)90039-8

Davis, J.K., Lawver, L.A., Norton, I.O., Gahagan, L.M., 2016. New Somali Basin magnetic anomalies and a plate model for the early Indian Ocean. Gondwana Res. 34, 16–28. https://doi.org/10.1016/j.gr.2016.02.010.

Debeuf, D., 2009. Étude de l'évolution volcano-structurale et magmatique de Mayotte, Archipel des Comores, océan Indien: approches structurale, pétrographique, géochimique et géochronologique.

Debeuf, D., Bachèlery, P., Sigmarsson, O., 2003. Two contemporaneous magma series on Mayotte Island, Comores Archipelago, Indian Ocean, in: EGS-AGU-EUG Joint Assembly, p. 9625.

Déprez, A., Doubre, C., Masson, F., Ulrich, P., 2013. Seismic and aseismic deformation along the East African Rift System from a reanalysis of the GPS velocity field of Africa. Geophys. J. Int. 193, 1353–1369.

Deville, E., Marsset, T., Courgeon, S., Jatiault, R., Ponte, J.-P., Thereau, E., Jouet, G., Jorry, S.J., Droz, L., 2018. Active fault system across the oceanic lithosphere of the Mozambique Channel: Implications for the Nubia–Somalia southern plate boundary. Earth Planet. Sci. Lett. 502, 210–220. https://doi.org/10.1093/gji/ggt085

Dieterich, J., 1988. Growth and Persistence of Hawaiian Volcanic Rift Zones. J. Geophys. Res. 93, 4258–4270. https://doi.org/10.1029/JB093iB05p04258

Dorschel, B., Jensen, L., Arndt, J.E., Frummer, G., De Haas, H., Fielies, A., Franke, D., Jokat, W., Krocker, R., Kroon, D., 2018. The Southwest Indian Ocean Bathymetric Compilation (swIOBC). Geochemistry, Geophys. Geosystems 19, 968–976. https://doi.org/10.1002/2017GC007274

Eagles, G., König, M., 2008. A model of plate kinematics in Gondwana breakup. Geophys. J. Int. 173, 703–717. https://doi.org/10.1111/j.1365-246X.2008.03753.x

Ebinger, C., 2012. Evolution of the Cenozoic East African Rift System: cratons, plumes and continental breakup, in: Regional Geology and Tectonics: Phanerozoic Rift Systems and Sedimentary Basins. Elsevier Boston, pp. 132–162.

Emerick, C.M., 1985. Geochronology and geochemistry of lavas from the Comores Islands and northern Madagascar [Ph. D. dissert.]. Oregon State Univ., Corvallis.

Emerick, C.M., Duncan, R.A., 1982. Age progressive volcanism in the Comores Archipelago, western Indian Ocean and implications for Somali plate tectonics. Earth Planet. Sci. Lett. 60, 415–428. https://doi.org/10.1016/0012-821X(82)90077-2

Famin, V., Michon, L., Bourhane, A., 2020. The Comoros archipelago: a right-lateral

transform boundary between the Somalia and Lwandle plates. Tectonophysics 789, 228539. https://doi.org/10.1016/j.tecto.2020.228539

Feuillet, N., Jorry, S., Crawford, W.C. et al. 2021. Birth of a large volcanic edifice offshore Mayotte via lithosphere-scale dyke intrusion. Nat. Geosci. 14, 787–795. https://doi.org/10.1038/s41561-021-00809-x

Fialko, Y.A., Rubin, A.M., 1999. What controls the along-strike slopes of volcanic rift zones? J. Geophys. Res. Solid Earth 104, 20007–20020. https://doi.org/10.1029/1999JB900143

Fink, J.H., Griffiths, R.W., 1990. Radial spreading of viscous-gravity currents with solidifying crust. J. Fluid Mech. 221, 485–509.

Fornari, D.J., Perfit, M.R., Allan, J.F., Batiza, R., Haymon, R., Barone, A., Ryan, W.B.F., Smith, T., Simkin, T., Luckman, M.A., 1988. Geochemical and structural studies of the Lamont seamounts: seamounts as indicators of mantle processes. Earth Planet. Sci. Lett. 89, 63–83. https://doi.org/10.1016/0012-821X(88)90053-7

Franke, D., Jokat, W., Ladage, S., Stollhofen, H., Klimke, J., Lutz, R., Mahanjane, E.S., Ehrhardt, A., Schreckenberger, B., 2015. The offshore East African Rift System: Structural framework at the toe of a juvenile rift. Tectonics 34, 2086–2104. https://doi.org/10.1002/2015TC003926

Fullea, J., Camacho, A.G., Negredo, A.M., Fernández, J., 2015. The Canary Islands hot spot: New insights from 3D coupled geophysical–petrological modelling of the lithosphere and uppermost mantle. Earth Planet. Sci. Lett. 409, 71–88. https://doi.org/10.1016/j.epsl.2014.10.038

Gee, M.J.R., Masson, D.G., Watts, A.B., Mitchell, N.C., 2001. Offshore continuation of volcanic rift zones, El Hierro, Canary Islands. J. Volcanol. Geotherm. Res. 105, 107–119. https://doi.org/10.1016/S0377-0273(00)00241-9

Geist, D., Diefenbach, B.A., Fornari, D.J., Kurz, M.D., Harpp, K., Blusztajn, J., 2008. Construction of the Galápagos platform by large submarine volcanic terraces. Geochemistry, Geophys. Geosystems 9. https://doi.org/10.1029/2007GC001795

Geist, D.J., Fornari, D.J., Kurz, M.D., Harpp, K.S., Adam Soule, S., Perfit, M.R., Koleszar, A.M., 2006. Submarine Fernandina: Magmatism at the leading edge of the Galápagos hot spot. Geochemistry, Geophys. Geosystems 7. https://doi.org/10.1029/2006GC001290

Gregg, T.K.P., Fink, J.H., 2000. A laboratory investigation into the effects of slope on lava flow morphology. J. Volcanol. Geotherm. Res. 96, 145–159. https://doi.org/10.1016/S0377-0273(99)00148-1

Grimison, N.L., Chen, W.P., 1988. Earthquakes in Davie Ridge–Madagascar region and the southern Nubian–Somalian plate boundary. J. Geophys. Res. 93, 10,439–10,450.

Hansen, S.E., Nyblade, A.A., Benoit, M.H., 2012. Mantle structure beneath Africa and Arabia from adaptively parameterized P-wave tomography: Implications for the origin of Cenozoic Afro-Arabian tectonism. Earth Planet. Sci. Lett. 319, 23–34. https://doi.org/10.1016/j.epsl.2011.12.023

Harpp, K.S., Fornari, D.J., Geist, D.J., Kurz, M.D., 2003. Genovesa Submarine Ridge: A manifestation of plume-ridge interaction in the northern Galápagos Islands. Geochemistry, Geophys. Geosystems 4. https://doi.org/10.1029/2003GC000531

Hartnady, C. J. H., 1985. Uplift, faulting, seismicity, thermal spring and possible incipient volcanic activity in the Lesotho-Natal Region, SE Africa: The Quathlamba Hotspot Hypothesis. Tectonics, 4(4), 371-377.

Hartnady, C.J.H., 1990. Seismicity and plate boundary evolution in southeastern Africa. South African J. Geol. 93, 473–484.

Hartnady, CJH, Ben-Avraham, Z., Rogers, J., 1992. Deep-ocean basins and submarine rises off the continental margin of south-eastern Africa: new geological research. S. Afr. J. Sci. 88 (11-12), 534–539.

Heirtzler, J. R., & Burroughs, R. H., 1971. Madagascar's paleoposition: new data from the Mozambique Channel. Science, 174(4008), 488-490.

Jokat, W., 2014. The expedition of the research vessel 'Sonne' to the Mozambique Basin in 2014 (SO-230). Alfred-Wegener-Institut, Helmholtz-Zentrum für Polar- und Meeresforschung, 125. http://epic.awi.de.

Jokat, W., 2009. The expedition of the research vessel Pelagia to the natal basin and the Mozambique ridge in 2009 (Project AISTEK III). Alfred-Wegener-Institut für Polar- und Meeresforschung, 67, http://epic.awi.de.

Jokat, W, 2006. Southeastern Atlantic and southwestern Indian Ocean: reconstruction of the sedimentary and tectonic development since the Cretaceous AISTEK-II: Mozambique Ridge and Mozambique Basin. Berichte zur Polarforsch. 521.

Jokat, W., Boebel, T., König, M., Meyer, U., 2003. Timing and geometry of early Gondwana breakup. J. Geophys. Res. Solid Earth 108. https://doi.org/10.1029/2002JB001802

Jorry, S., 2014. PTOLEMEE cruise, RV L'Atalante.

Jorry, S.J., Camoin, G.F., Jouet, G., Le Roy, P., Vella, C., Courgeon, S., Prat, S., Fontanier, C., Paumard, V., Boulle, J., 2016. Modern sediments and Pleistocene reefs from isolated

carbonate platforms (Iles Eparses, SW Indian Ocean): a preliminary study. Acta Oecologica 72, 129–143. https://doi.org/10.1016/j.actao.2015.10.014

Jouet, G., Deville, E., 2015. PAMELA-MOZ04 cruise. Pourquoi pas ? https://doi.org/https://doi.org/10.17600/15000700

Klimke, J., Franke, D., Mahanjane, E.S. & Leitchenkov, G., 2018. Tie points for Gondwana reconstructions from a structural interpretation of the Mozambique Basin, East Africa and the Riiser-Larsen Sea, Antarctica, Solid Earth, 9, 25–37. https://doi.org/10.5194/se-9-25-2018

Klimke, J., Franke, D., Gaedicke, C., Schreckenberger, B., Schnabel, M., Stollhofen, H., Rose, J., Chaheire, M., 2016. How to identify oceanic crust—Evidence for a complex break-up in the Mozambique Channel, off East Africa. Tectonophysics, 693, 436-452. https://doi.org/10.1016/j.tecto.2015.10.012

König, M., Jokat, W., 2006. The mesozoic breakup of the weddell sea. Journal of Geophysical Research: Solid Earth, 111(B12). https://doi.org/10.1029/2005JB004035

König, M., Jokat, W., 2010. Advanced insights into magmatism and volcanism of the Mozambique Ridge and Mozambique Basin in the view of new potential field data. Geophys. J. Int. 180, 158–180. https://doi.org/10.1111/j.1365-246X.2009.04433.x

Kusky, T.M., Toraman, E., Raharimahefa, T., Rasoazanamparany, C., 2010. Active tectonics of the Alaotra–Ankay Graben System, Madagascar: possible extension of Somalian–African diffusive plate boundary? Gondwana Res 18:274–294

Leclaire, L., Bassias, Y., Clocchiatti, M., Segoufin, J., 1989. La Ride de Davie dans le Canal de Mozambique: approche stratigraphique et géodynamique. CR Acad. Sci.(Paris, série 2) 308, 1077–1082.

Leinweber, V.T., Jokat, W., 2012. The Jurassic history of the Africa–Antarctica corridor—new constraints from magnetic data on the conjugate continental margins. Tectonophysics 530, 87–101. https://doi.org/10.1016/j.tecto.2011.11.008

Leinweber, V.T., Klingelhoefer, F., Neben, S., Reichert, C., Aslanian, D., Matias, L., Heyde, I., Schreckenberger, B., Jokat, W., 2013. The crustal structure of the Central Mozambique continental margin—Wide-angle seismic, gravity and magnetic study in the Mozambique Channel, Eastern Africa. Tectonophysics 599, 170–196. https://doi.org/10.1016/j.tecto.2013.04.015

Lemoine, A., Briole, P., Bertil, D., Roullé, A., Foumel, M., THINON, I., Raucoules, D., Michele, M. de, Valty, P., 2020. The 2018-2019 seismo-volcanic crisis east of Mayotte,

Comoros islands: seismicity and ground deformation markers of an exceptional submarine eruption. https://doi.org/10.31223/osf.io/d46xj

Leroux, E., Counts, J., Jorry, S., Jouet, G., Révillon, S., Boudagher-Fadel, M.K., Courgeon, S., Berthod, C., Ruffet, G., Bachèlery, P., 2020. Evolution of the glorieuses seamount in the sw indian ocean and surrounding deep somali basin since the cretaceous. Mar. Geol. https://doi.org/10.1016/j.margeo.2020.106202

Levin, N., Beger, M., Maina, J., McClanahan, T., Kark, S., 2018. Evaluating the potential for transboundary management of marine biodiversity in the Western Indian Ocean. Australas. J. Environ. Manag. 25, 62–85. https://doi.org/10.1080/14486563.2017.1417167

Liebske, C., Behrens, H., Holtz, F., Lange, R.A., 2003. The influence of pressure and composition on the viscosity of andesitic melts. Geochim. Cosmochim. Acta 67, 473–485. https://doi.org/10.1016/S0016-7037(02)01139-9

Lipman, P.W., Calvert, A.T., 2011. Early growth of Kohala volcano and formation of long Hawaiian rift zones. Geology 39, 659–662. https://doi.org/10.1130/G31929.1

Llanes, P., Herrera, R., Gómez, M., Muñoz, A., Acosta, J., Uchupi, E., Smith, D., 2009. Geological evolution of the volcanic island La Gomera, Canary Islands, from analysis of its geomorphology. Mar. Geol. 264, 123–139. https://doi.org/10.1016/j.margeo.2009.05.001

Lonsdale, P., 1989. A geomorphological reconnaissance of the submarine part of the East Rift Zone of Kilauea Volcano, Hawaii. Bull. Volcanol. 51, 123–144. https://doi.org/10.1007/BF01081981

MacDonald, G.A., 1972. Volcanoes, Prentice H. ed. New Jersey.

Macgregor, D., 2015. History of the development of the East African Rift System: a series of interpreted maps through time. J. African Earth Sci. 101, 232–252. https://doi.org/10.1016/j.jafrearsci.2014.09.016

Mahanjane, E. S., 2014. The Davie Fracture Zone and adjacent basins in the offshore Mozambique Margin – A new insights for the hydrocarbon potential. Marine and Petroleum Geology, 57, 561-571. https://doi.org/10.1016/j.marpetgeo.2014.06.015

Mahanjane, E.S., 2012. A geotectonic history of the northern Mozambique Basin including the Beira High – A contribution for the understanding of its development. Mar. Pet. Geol. 36, 1–12. https://doi.org/10.1016/j.marpetgeo.2012.05.007

Mark, R.K., Moore, J.G., 1987. Slopes of the Hawaiian ridge. US Geol. Surv. Prof. Pap 1350,

101–107.

Martin, A.K., Hartnady, C.J.H., 1986. Plate tectonic development of the South West Indian Ocean: a revised reconstruction of East Antarctica and Africa. J. Geophys. Res. 91, 4767–4786. https://doi.org/10.1029/JB091iB05p04767.

McClanahan, T.R., Friedlander, A.M., Graham, N.A.J., Chabanet, P., Bruggemann, J.H., 2021. Variability in coral reef fish baseline and benchmark biomass in the central and western Indian Ocean provinces. Aquat. Conserv. Mar. Freshw. Ecosyst. 31, 28–42. https://doi.org/10.1002/aqc.3448

Merz, D.K., Caplan-Auerbach, J., Thurber, C.H., 2019. Seismicity and Velocity Structure of Lō'ihi Submarine Volcano and Southeastern Hawai'i. J. Geophys. Res. Solid Earth 124, 11380–11393. https://doi.org/10.1029/2019JB018168

Mesko, G.T., Class, C., Maqway, M.D., Boniface, N., Manya, S., Hemming, S.R., 2014. The timing of early magmatism and extension in the Southern East African rift: tracking geochemical source variability with 40 Ar/39 Ar geochronology at the Rungwe Volcanic Province, SW Tanzania, in: AGU Fall Meeting Abstracts. pp. V51A-4730.

Michon, L., 2016. The volcanism of the Comoros archipelago integrated at a regional scale, in: Active Volcanoes of the Southwest Indian Ocean. Springer, pp. 333–344. https://doi.org/10.1007/978-3-642-31395-0_21

Michon, L., Saint-Ange, F., Bachelery, P., Villeneuve, N., Staudacher, T., 2007. Role of the structural inheritance of the oceanic lithosphere in the magmato-tectonic evolution of Piton de la Fournaise volcano (La Réunion Island). J. Geophys. Res. Solid Earth 112, 1–21. https://doi.org/10.1029/2006JB004598

Miramontes, E., Penven, P., Pierens, R., Droz, L., Toucanne, S., Jorry, S.J., Jouet, G., Pastor, L., Jacinto, R.S., Gaillot, A., 2019. The influence of bottom currents on the Zambezi Valley morphology (Mozambique Channel, SW Indian Ocean): In situ current observations and hydrodynamic modelling. Mar. Geol. 410, 42–55. https://doi.org/10.1016/j.margeo.2019.01.002

Mitchell, N.C., Masson, D.G., Watts, A.B., Gee, M.J.R., Urgeles, R., 2002. The morphology of the submarine flanks of volcanic ocean islands: a comparative study of the Canary and Hawaiian hotspot islands. J. Volcanol. Geotherm. Res. 115, 83–107. https://doi.org/10.1016/S0377-0273(01)00310-9

Mitchell, N.C., Stretch, R., Oppenheimer, C., Kay, D., Beier, C., 2012. Cone morphologies associated with shallow marine eruptions: east Pico Island, Azores. Bull. Volcanol. 74,

2289–2301. https://doi.org/10.1007/s00445-012-0662-5

Mougenot, D., Recq, M., Virlogeux, P., Lepvrier, C., 1986. Seaward extension of the East African rift. Nature 321, 599. https://doi.org/10.1038/321599a0

Mueller, C.O., Jokat, W., 2019. The initial Gondwana break-up: a synthesis based on new potential field data of the Africa-Antarctica Corridor. Tectonophysics 750, 301–328. https://doi.org/10.1016/j.tecto.2018.11.008

Mueller, C.O., Jokat, W., 2017. Geophysical evidence for the crustal variation and distribution of magmatism along the central coast of Mozambique. Tectonophysics 712, 684–703. https://doi.org/10.1016/j.tecto.2017.06.007

Mueller, C.O., Jokat, W., Schreckenberger, B., 2016. The crustal structure of Beira High, central Mozambique—combined investigation of wide-angle seismic and potential field data. Tectonophysics 683, 233–254. https://doi.org/10.1016/j.tecto.2016.06. 028.

Mukhopadhyay, R., Batiza, R., 1994. Basinal seamounts and seamount chains of the central Indian Ocean: Probable near-axis origin from a fast-spreading ridge. Mar. Geophys. Res. 16, 303–314. https://doi.org/10.1007/BF01247147

Mukhopadhyay, R., Khadge, N.H., 1990. Seamounts in the Central Indian Ocean Basin: indicators of the Indian plate movement. Proc. Indian Acad. Sci. Planet. Sci. 99, 357–365.

Mullins HT and Hine AC (1989) Scalloped bank margins: Beginning of the end for carbonate platforms? Geology 17 (1) 30-33

Navarro, a., Lourenço, N., Chorowicz, J., Miranda, J.M., Catalão, J., 2009. Analysis of geometry of volcanoes and faults in Terceira Island (Azores): Evidence for reactivation tectonics at the EUR/AFR plate boundary in the Azores triple junction. Tectonophysics 465, 98–113. https://doi.org/10.1016/j.tecto.2008.10.020

Nguyen, L.C., Hall, S.A., Bird, D.E., Ball, P.J., 2016. Reconstruction of the East Africa and Antarctica continental margins. J. Geophys. Res. Solid Earth 121, 4156–4179. https://doi.org/10.1002/2015JB012776.

Norton, I.O., Sclater, J.G., 1979. A model for the evolution of the Indian Ocean and the breakup of Gondwanaland. J. Geophys. Res. 84, 6803–6830. https://doi.org/10.1029/JB084iB12p06803.

Nougier, J., Cantagrel, J.M., Karche, J.P., 1986. The Comores archipelago in the western Indian Ocean: volcanology, geochronology and geodynamic setting. J. African Earth Sci. 5, 135–144. https://doi.org/10.1016/0899-5362(86)90003-5

O'Connor, J.M., Jokat, W., Regelous, M., Kuiper, K.F., Miggins, D.P., Koppers, A.A.P., 2019. Superplume mantle tracked isotopically the length of Africa from the Indian Ocean to the Red Sea. Nat. Commun. 10, 1–13. https://doi.org/10.1038/s41467-019-13181-7

Olu, K., 2014. PAMELA-MOZ01 cruise, RV L'Atalante. https://doi.org/10.17600/14001000

Pelleter, A.-A., Caroff, M., Cordier, C., Bachèlery, P., Nehlig, P., Debeuf, D., Arnaud, N., 2014. Melilite-bearing lavas in Mayotte (France): An insight into the mantle source below the Comores. Lithos 208, 281–297. https://doi.org/10.1016/j.lithos.2014.09.012

Phethean, J.J.J., Kalnins, L.M., van Hunen, J., Biffi, P.G., Davies, R.J., McCaffrey, K.J.W., 2016. Madagascar's escape from Africa: a high-resolution plate reconstruction for the Western Somali Basin and implications for supercontinent dispersal. Geochem. Geophys. Geosyst. 17, 2825–2834. https://doi.org/10.1002/2016GC006624.

Ponte, J. P., Robin, C., Guillocheau, F., Popescu, S., Suc, J. P., Dall'Asta, M., Melinte-Dobrinescu, M.C., Bubik, M, Dupont, G., Gaillot, J., 2019. The Zambezi delta (Mozambique Channel, East Africa): High resolution dating combining bio-orbital and seismic stratigraphies to determine climate (paleoprecipitation) and tectonic controls on a passive margin. Marine and Petroleum Geology, 105, 293-312. https://doi.org/10.1016/j.marpetgeo.2018.07.017

Quidelleur, X., Michon, L., Famin, V., Geffray, M. C., Danišík, M., Gardiner, N., Rusquet, A., Zakaria, M. G., 2022. Holocene volcanic activity in Anjouan Island (Comoros archipelago) revealed by new Cassignol-Gillot groundmass K–Ar and 14C ages. Quaternary Geochronology, 67, 101236. https://doi.org/10.1016/j.quageo.2021.101236

Rabinowitz, P.D., Coffin, M.F., Falvey, D., 1983. The separation of Madagascar and Africa. Science (80-.). 220, 67–69.

Raillard, S., 1990. Les Marges de l'Afrique de l'Est et les Zones de Fracture Associées: Chaine Davie et Ride du Mozambique (PhD Thesis). Université Pierre et Marie Curie Paris VI.

Rappaport, Y., Naar, D.F., Barton, C.C., Liu, Z.J., Hey, R.N., 1997. Morphology and distribution of seamounts surrounding Easter Island. J. Geophys. Res. Solid Earth 102, 24713–24728. https://doi.org/10.1029/97JB01634

Reeves, C.V., 2018. The development of the East African margin during Jurassic and Lower Cretaceous times: a perspective from global tectonics. Pet. Geosci. 24, 41–56. https://doi.org/10.1144/petgeo2017-021.

Reeves, C.V., Teasdale, J.P., Mahanjane, E.S., 2016. Insight into the Eastern Margin of Africa

from a new tectonic model of the Indian Ocean. Geol. Soc. Lond. Spec. Publ. 431, 1–24. https://doi.org/10.1144/SP431.12.

Reeves, C., 2014. The position of Madagascar within Gondwana and its movements during Gondwana dispersal. J. African Earth Sci. 94, 45–57. https://doi.org/10.1016/j.jafrearsci.2013.07.011

Reeves, C., De Wit, M., 2000. Making ends meet in Gondwana: retracing the transforms of the Indian Ocean and reconnecting continental shear zones. Terra Nov. 12, 272–280. https://doi.org/10.1046/j.1365-3121.2000.00309.x

Renne, P.R., Balco, G., Ludwig, K.R., Mundil, R., Min, K., 2011. Response to the comment by WH Schwarz et al. on "Joint determination of 40K decay constants and 40Ar*/40K for the Fish Canyon sanidine standard, and improved accuracy for 40Ar/39Ar geochronology" by PR Renne et al.(2010). Geochim. Cosmochim. Acta 75, 5097–5100.

Renne, P.R., Mundil, R., Balco, G., Min, K., Ludwig, K.R., 2010. Joint determination of 40K decay constants and 40Ar*/40K for the Fish Canyon sanidine standard, and improved accuracy for 40Ar/39Ar geochronology. Geochim. Cosmochim. Acta 74, 5349–5367. https://doi.org/10.1016/j.gca.2010.06.017

Renne, P.R., Swisher, C.C., Deino, A.L., Karner, D.B., Owens, T.L., DePaolo, D.J., 1998. Intercalibration of standards, absolute ages and uncertainties in 40Ar/39Ar dating. Chem. Geol. 145, 117–152. https://doi.org/10.1016/S0009-2541(97)00159-9

Romagnoli, C., Belvisi, V., Innangi, S., Di Martino, G., Tonielli, R. 2020. New insights on the evolution of the Linosa volcano (Sicily Channel) from the study of its submarine portions, Marine Geology, 2020, 419, pp. 1 – 12. 10.1016/j.margeo.2019.106060

Romer, R.H.W., Beier, C., Haase, K.M., Hübscher, C., 2018. Correlated changes between volcanic structures and magma composition in the Faial volcanic system, Azores. Front. Earth Sci. 6, 78. https://doi.org/10.3389/feart.2018.00078

Rowden, A.A., Clark, M.R., Wright, I.C., 2005. Physical characterisation and a biologically focused classification of "seamounts" in the New Zealand region. New Zeal. J. Mar. Freshw. Res. 39, 1039–1059. https://doi.org/10.1080/00288330.2005.9517374

Rubin, K.H., Soule, S.A., Chadwick, W.W., Fornari, D.J., Clague, D.A., Embley, R.W., Baker, E.T., Perfit, M.R., Caress, D.W., Dziak, R.P., 2012. Volcanic eruptions in the deep sea. Oceanography 25, 142–157.

Ruffet, G., Gruau, G., Ballèvre, M., Féraud, G., Philippot, P., 1997. Rb/Sr and 40Ar/39Ar laser probe dating of high-pressure phengites from the Sesia zone (Western Alps):

underscoring of excess argon and new age constraints on the high-pressure metamorphism. Chem. Geol. 141, 1–18. https://doi.org/10.1016/S0009-2541(97)00052-1

Ruffet, G., Féraud, G., Balèvre, M., Kiénast, J.-R., 1995. Plateau ages and excess argon in phengites: an 40Ar/ 39Ar laser probe study of Alpine micas (Sesia Zone, Western Alps, northern Italy). Chem. Geol. 121, 327–343. https://doi.org/10.1016/0009-2541(94)00132-R

Ruffet, G., Féraud, G., Amouric, M., 1991. Comparison of 40Ar/39Ar conventional and laser dating of biotites from the North Trégor Batholith. Geochim. Cosmochim. Acta 55, 1675–1688. https://doi.org/10.1016/0016-7037(91)90138-U

Saria, E., Calais, E., Stamps, D.S., Delvaux, D., Hartnady, C.J.H., 2014. Present-day kinematics of the East African Rift. J. Geophys. Res. Solid Earth 119, 3584–3600. https://doi.org/10.1002/2013JB010901

Scrutton, R.a., 1978. Davie fracture zone and the movement of Madagascar, Earth planet. Sci. Lett., 39, 84–88.

Segoufin, J., Patriat, P., 1980. Existences d'anomalies mésozoïques dans le bassin de Somalie: implications pour les relations Afrique-Antarctique-Madagascar. C.R. Acad. Sci. 291 (1980), 85–88.

Sinha, S.T., Saha, S., Longacre, M., Basu, S., Jha, R. & Mondal, T., 2019. Crustal Architecture and nature of continental breakup along a transform margin: new insights from Tanzania–Mozambique Margin, Tectonics, 2018TC005221. https://doi.org/10.1029/2018TC005221

Smith, D.K., Kong, L.S.L., Johnson, K.T.M., Reynolds, J.R., 2002. Volcanic morphology of the submarine Puna Ridge, Kilauea volcano. Geophys. Monogr. Geophys. UNION 128, 125–142.

Späth, A., Roex, A.P. Le, Duncan, R.A., 1996. The geochemistry of lavas from the Comores Archipelago, Western Indian Ocean: petrogenesis and mantle source region characteristics. J. Petrol. 37, 961–991. https://doi.org/10.1093/petrology/37.4.961

Stabile, P., Webb, S., Knipping, J.L., Behrens, H., Paris, E., Giuli, G., 2016. Viscosity of pantelleritic and alkali-silicate melts: Effect of Fe redox state and Na/(Na+ K) ratio. Chem. Geol. 442, 73–82. https://doi.org/10.1016/j.chemgeo.2016.09.003

Stamps, D.S., Calais, E., Saria, E., Hartnady, C., Nocquet, J., Ebinger, C.J., Fernandes, R.M., 2008. A kinematic model for the East African Rift. Geophys. Res. Lett. 35. https://doi.org/10.1029/2007GL032781

Stamps, D.S., Saria, E., Kreemer, C., 2018. A Geodetic Strain Rate Model for the East African Rift System. Sci. Rep. 8, 732. https://doi.org/10.1038/s41598-017-19097-w

Stamps, D.S., Kreemer, C., Fernandes, R., Rajaonarison, T.A., Rambolamanana, G., 2021. Redefining East African Rift System kinematics. Geology. https://doi.org/10.1130/G47985.1

Stretch, R.C., Mitchell, N.C., Portaro, R.A., 2006. A morphometric analysis of the submarine volcanic ridge south-east of Pico Island, Azores. J. Volcanol. Geotherm. Res. 156, 35–54. https://doi.org/10.1016/j.jvolgeores.2006.03.009

Thompson, G., Bryan, W. B., Frey, F. A., Dickey, J. S., & Davies, H., 1982. Petrology, geochemistry and original tectonic setting of basalts from the Mozambique Basin and Ridge (DSDP sites 248, 249 and 250), and from the Southwest Indian Ridge (DSDP site 251). Marine Geology, 48(3-4), 175-195.

Thompson, J.O., Moulin, M., Aslanian, D., De Clarens, P., Guillocheau, F., 2019. New starting point for the Indian Ocean: Second phase of breakup for Gondwana. Earth-Science Rev. 191, 26–56. https://doi.org/10.1016/j.earscirev.2019.01.018

Tibaldi, A., 1995. Morphology of pyroclastic cones and tectonics. J. Geophys. Res. 100, 24,521-24,535. https://doi.org/10.1029/95JB02250

Tuck-Martin, A., Adam, J. & Eagles, G., 2018. New plate kinematic model and tectono-stratigraphic history of the East Afr can and West Madagas- can Margins, Basin Res., 30, 1118–1140.

Tibaldi, A., 2015. Structure of volcano plumbing systems : A review of multi-parametric effects. J. Volcanol. Geotherm. Res. 298, 85–135. https://doi.org/10.1016/j.jvolgeores.2015.03.023

Tzevahirtzian, A., Zaragosi, S., Bachèlery, P., Biscara, L., Marchès, E., 2021. Submarine morphology of the Comoros volcanic archipelago. Mar. Geol. 432. https://doi.org/10.1016/j.margeo.2020.106383

Upton, B.G.J., 1982. Oceanic Islands. In: Nairn, P., Stehli, F. (Eds.), Ocean Basins and their Margins, Indian Ocean, 6(13). Plenum Press, New York, pp. 585–648.

Vormann, M., Franke, D. & Jokat, W., 2020. The crustal structure of the southern Davie Ridge offshore northern Mozambique—a wide- angle seismic and potential field study, Tectonophysics, 778, 228370. https://doi.org/10.1016/j.tecto.2020.228370.

Vormann, M., Jokat, W., 2021a. Crustal variability along the rifted/sheared East African margin: a review. Geo-Marine Letters, 41(2), 1-9. https://doi.org/10.1007/s00367-021-

00690-y

Vormann, M., Jokat, W., 2021b. The crustal structure of the Kerimbas Basin across the offshore branch of the East African Rift System. Geophys. J. Int. 226, 2073–2102. https://doi.org/10.1093/gji/ggab194

Weiß, B.J., Hübscher, C., Lüdmann, T., 2015. The tectonic evolution of the southeastern Terceira Rift/São Miguel region (Azores). Tectonophysics 654, 75–95. https://doi.org/10.1016/j.tecto.2015.04.018

Wessel P (2007) Seamount characteristics. Seamounts Ecol Fish Conserv 3–25

Wessel P, Sandwell DT, Kim S-S (2010) The global seamount census. Oceanography 23:24–33

Wiles, E., Green, A., Watkeys, M., Jokat, W., & Krocker, R., 2014. Anomalous seafloor mounds in the northern Natal Valley, southwest Indian Ocean: implications for the East African Rift System. Tectonophysics, 630, 300-312. https://doi.org/10.1016/j.tecto.2014.05.030

Wiles, E., Watkeys, M., Jokat, W., 2020. Surface expression of microplate boundary kinematics: An isolated abyssal hill in the Mozambique Channel. J. African Earth Sci. 168, 103830. https://doi.org/10.1016/j.jafrearsci.2020.103830

Yang, Z., Chen, W.-P., 2010. Earthquakes along the East African Rift System: a multi- scale, system-wide perspective. J. Geophys. Res. 115, B12309. https://doi.org/10.1029/2009JB006779.

Yesson C, Clark MR, Taylor ML, Rogers AD (2011) The global distribution of seamounts based on 30 arc seconds bathymetry data. Deep Sea Res Part I Oceanogr Res Pap 58:442–453

York, D., 1968. Least squares fitting of a straight line with correlated errors. Earth Planet. Sci. Lett. 5, 320–324.

York, D., Evensen, N.M., Martınez, M.L., De Basabe Delgado, J., 2004. Unified equations for the slope, intercept, and standard errors of the best straight line. Am. J. Phys. 72, 367–375. https://doi.org/10.1119/1.1632486

Zinke, J., Reijmer, J.J.G., Thomassin, B.A., Dullo, W.-C., Grootes, P.M., Erlenkeuser, H., 2003. Postglacial flooding history of Mayotte lagoon (Comoro archipelago, southwest Indian Ocean). Mar. Geol. 194, 181–196. https://doi.org/10.1016/S0025-3227(02)00705-3

Figure captions

Figure 1: a) Geological context showing the study area (red box) located on the Quathlamba seismic axis (after Courgeon, 2017 and Deville et al., 2018), GEBCO 30 arc-second global grid of elevation 2014, about 930 m-resolution. White hatched lines : proposed plate boundaries, b) Bathymetric map of the seamounts located in the southern part of the Mozambique Channel, c) Morphological map of the region showing profiles across edifice summit (A-B) and volcanic ridge (X-Y), and dredge locations (in red) for samples used in $^{40}Ar/^{39}Ar$ dating. G : Glorieuses, ABFZ : Andrew Bain Fracture Zone, EPFZ : Prince Edward Fracture Zone, ESFZ : Eric Simpson Fracture Zone, MOZ: Mozambique Ridge

Figure 2: Interpretative map of the Bassas da India/Europa complex showing main geomorphologic features. Boxes indicate areas shown in more detail in Figures 5 and 8.

Figure 3: Bathymetric elevation of a) major volcanic edifices in the southern part of the Mozambique channel and b) identified volcanic ridges. All sections are marked on Fig. 1c.

Figure 4: Submarine pictures from the Hall Bank to the volcanic ridge located in the southwest part of Bassas da India. a) Volcanic rocks on carbonate substrate on the top of Hall Bank. b) Breccia in a faulted zone on the top of Hall Bank. c) Lava outcrops on a drowned terrace on the southern edge of Bassas da India. d) Recent fracture affecting sediments and volcanic rocks in the southeast of Bassas da India. Picture locations are marked on Fig. 2.

Figure 5: Details of delineated geomorphologic features interpreted from multibeam backscatter and bathymetry. a-b) Hall Bank and the west part of Jaguar Bank and c-d) Jaguar Bank. Dark shades indicate regions of greater acoustic backscatter and are interpreted as volcanic or carbonated units not covered by significant marine sedimentation. Volcanic features located on the carbonate platform have been identified by Courgeon et al., 2016.

Figure 6: $^{39}Ar//^{40}Ar$ age spectra and $^{37}ArCa/^{39}ArK$ spectra of samples MOZ01-DW05-01 and MOZ01-DW05-13 samples collected on Hall Bank, and samples MOZ01-DR19-04 and MOZ04-DR08-01 collected near Jaguar Bank and Bassas da India, respectively. Apparent age error bars are at the 2σ level; errors in the J-parameter are not included. Plateau age is given

with 2σ uncertainties including errors in the J-parameter. Inverse isochron (correlation) diagram with $^{36}Ar/^{40}Ar$ vs. $^{39}Ar/^{40}Ar$. White ellipses are excluded from isochron regression (York, 1968; York et al., 2004), MSWD stands for Mean Squares of Weighted Deviates. Dredge locations are marked on Fig. 1c.

Figure 7: 3D images, with x5 vertical exaggeration, showing the main structures recognized in the Bassas da India-Europa complex. a) General view of the three seamounts discovered between Bassas da India and Europa. b) Volcanic ridges between Jaguar Bank and Bassas da India. c) Northeast side of Pamela Seamount 1 (PS1) seamount and Bassas da India atoll . d) View of PS1, Pamela Seamount 2 (PS2) and Ptolemee north of Europa.

Figure 8: Details of delineated geomorphologic features derived from multibeam backscatter and bathymetry. a-b) PS1 located on the south flank of Bassas da India, c-d) Ptolemee seamount, and e-f) Northern flank of Europa. Dark shades indicate regions of greater acoustic backscatter.

Figure 9: Morphological characteristics of volcanic cones identified. a) Basal area of volcanic cones versus height, b) Frequency of volcanic cones height, c) Average base length versus height of volcanic cones, dashed lines indicate values of aspect ratio (height/average base length). Linoas, Hawaii, Canary, Azores and Comoros data are from Romagnoli et al. 2021; Clague et al. 2000, Mitchell et al., 2002; Stretch et al., 2006; Mitchell et al., 2012; Casalbore et al., 2015; Weiß et al. 2015 and Tzevahirtzian et al., 2021, respectively, d) Mean slope versus basal area of volcanic cones, e) Frequency of mean slope of volcanic cones, f) Frequency of maximum slope of volcanic cones, g) Maximum slope versus height of volcanic cones, h) Frequency of direction of elongation of volcanic cones.

Figure 10: 3D diagram illustrating the magma emplacement in Bassas da India/Europa complex. The eruptions of the proximal section of the rift zones are fed by lateral injections of magma from a shallow magma chamber located under the main volcanic center, whereas direct magma injections from a deeper storage zone feed the large volcanic cones in the distal section of the rift zones, or, occasionally, at higher altitude. Large edifices are supplied by deep and shallow depth magma chambers. The lithosphere structuration has been inferred by Mueller and Jokat (2017) from synthetic amplitude modelling along the two seismic

refraction profiles (including the 20140010 seismic profile which is located to the north-west of the Bassas da India/Europa complex) coupled with two magnetic models.

Figure 11: Map of seamounts' basal area (a) and height (b). Statistical analysis of seamounts' basal area (c) and height (d) for NE-SW and SE-NW trends, in pink and in green, respectively. e) stereographic projections of fault strikes (Deville et al., 2018) and elongated seamount orientations.

Table captions

Table 1: Location of dredges performed during PAMELA-MOZ01 (DW5 and DR19) and PAMELA-MOZ04 (DR08) oceanographic cruises.

Dredge	*Oceanographic campaign*	Location	DOI	Latitude	Longitude	*Depth*	Latitude	Longitude	*Depth*
MOZ01-DW05	*PAMELA-MOZ01*	Hall Bank	10.17600/14001000	S 21° 51,3409'	E 39° 6,15217'	512	S 21° 51,80274'	E 39° 6,38168'	507
MOZ01-DR19	*PAMELA-MOZ01*	Jaguar Bank	10.17600/14001000	S 21°44,190'	E 39°32,295'	941	S 21°44,101'	E 39°32,302'	991
MOZ04-DR08	*PAMELA-MOZ04*	Bassas da India	10.17600/15000700	21°34' 14.9" S	39°40' 34.7" E	521	21°34' 4.4" S	39°40' 35.3" E	510

Table 2: Physical variables of all identified volcanic structures that form the Bassas da India/Europa complex.

Site	Name	Latitude (DD)	Longitude (DD)	Diameter (m)	Area (Km2)	Elevation (m)	Prof_MEAN (m)	Pente_MIN (°)	Pente_MAX (°)	Pente_MEAN (°)	ORIENTATION	Aspect ratio
Hall Bank	SM-1	39.0446	-21.8019	241	0.0404	47	-1718	15.00	24.07	20.30	162	0.20
Hall Bank	SM-2	39.0457	-21.7931	1456	0.9180	353	-1715	4.78	32.05	21.15	123	0.24
Hall Bank	SM-3	39.0515	-21.8028	335	0.0791	63	-1629	2.55	20.65	11.95	172	0.19
Hall	S	39.	-	519	0.	140	-	2.18	29.7	20.14	167	0.

Bank	M-4	1083	21.9190		1907		1374		3			27
	S	39.-			0.							
Hall Bank	M-5	1210	21.9222	524	1791	243	-1565	15.48	32.12	25.09	117	0.46
	S	39.-			0.							
Hall Bank	M-6	1339	21.8542	253	0456	54	-1009	20.22	29.06	24.99	90	0.21
	S	39.-			0.							
Hall Bank	M-7	1352	21.9265	553	2269	179	-1851	6.88	33.35	23.06	135	0.32
	S	39.-			0.							
Hall Bank	M-8	1501	21.8496	477	1471	151	-1378	10.28	31.01	21.97	97	0.32
	S	39.-			0.							
Hall Bank	M-9	1509	21.8318	605	2482	183	-1819	1.61	31.16	23.43	124	0.30
	S	39.-			0.							
Hall Bank	M-10	1516	21.8727	289	0612	63	-1404	14.08	25.61	19.33	90	0.22
	S	39.-			0.							
Hall Bank	M-11	1557	21.8825	654	2287	120	-1648	4.33	24.55	15.42	99	0.19
	S	39.-			0.							
Hall Bank	M-12	1569	21.8709	660	3115	217	-1499	5.25	34.32	21.85	144	0.33
	S	39.-			0.							
Hall Bank	M-13	1586	21.9191	717	3343	157	-2130	1.14	32.16	19.71	139	0.22
	S	39.-			0.							
Hall Bank	M-14	1630	21.8761	708	2990	233	-1682	8.98	32.73	23.58	172	0.33
	S	39.-			0.							
Hall Bank	M-15	1724	21.8915	745	3676	193	-2117	3.05	28.21	16.63	163	0.26
	S	39.-			0.							
Hall Bank	M-16	2040	21.8451	428	1314	104	-2228	7.74	26.73	18.71	45	0.24
	S	39.-			0.							
Jaguar Bank	M-17	2309	21.8888	1116	7806	237	-2347	9.36	34.62	22.03	10	0.21
	S	39.-			0.							
Jaguar Bank	M-18	2328	21.7858	536	2099	104	-2638	1.78	23.60	12.96	0	0.19
	S	39.-			0.							
Jaguar Bank	M-19	2511	21.8648	1032	4785	202	-2217	5.64	31.69	20.18	15	0.20
	S	39.-			0.							
Jaguar Bank	M-20	2540	21.8262	932	5609	273	-2269	10.31	28.20	20.81	21	0.29

	S	39.	-		0.							
Jaguar	M-	258	21.9		30		-		29.8			0.
Bank	21	8	034	777	61	171	2224	5.39	3	19.82	169	22
	S	39.	-		0.							
Jaguar	M-	262	21.9		10		-		18.3			0.
Bank	22	5	080	409	29	65	2259	1.38	0	11.65	31	16
	S	39.	-		0.							
Jaguar	M-	263	21.8		71		-		32.6			0.
Bank	23	6	611	985	09	309	2083	4.22	3	26.10	172	31
	S	39.	-		0.							
Jaguar	M-	270	21.8		39		-		31.3			0.
Bank	24	3	402	737	42	195	2027	7.74	0	19.41	131	26
	S	39.	-		0.							
Jaguar	M-	279	21.7		32		-		28.0			0.
Bank	25	2	861	683	35	234	1660	3.78	6	20.59	177	34
	S	39.	-		0.							
Jaguar	M-	285	21.7		14		-		27.8			0.
Bank	26	8	800	482	14	136	1483	8.07	6	19.92	25	28
	S	39.	-		0.							
Jaguar	M-	291	21.7		30		-		29.0			0.
Bank	27	9	385	637	73	139	1952	5.65	7	17.99	33	22
	S	39.	-		0.							
Jaguar	M-	296	21.7		10		-		25.8			0.
Bank	28	6	665	417	54	5	1452	6.08	1	16.72	15	12
	S	39.	-		0.							
Jaguar	M-	296	21.8		34		-		34.4			0.
Bank	29	8	663	728	22	250	1638	4.77	2	25.02	168	34
	S	39.	-		0.							
Jaguar	M-	297	21.7		10				25.9			0.
Bank	30	5	955	396	48	128	-970	6.76	8	18.85	0	32
	S	39.	-		0.							
Jaguar	M-	298	21.7		07		-	14.9	30.0			0.
Bank	31	6	909	332	95	123	1022	5	8	24.81	20	37
	S	39.	-		0.							
Jaguar	M-	299	21.7		09		-		30.7			0.
Bank	32	0	825	359	41	125	1220	1.39	7	23.34	0	35
	S	39.	-		0.							
Jaguar	M-	299	21.9		25		-		29.6			0.
Bank	33	3	145	684	65	173	1871	3.68	9	22.52	157	25
	S	39.	-		0.							
Jaguar	M-	302	21.7		63		-		32.9			0.
Bank	34	7	559	969	39	332	1813	5.26	6	23.03	136	34
	S	39.	-		0.							
Jaguar	M-	303	21.7		08		-	12.3	19.5			0.
Bank	35	9	649	372	39	96	1491	3	9	15.45	130	26
	S	39.	-		0.							
Jaguar	M-	305	21.7		07				22.7			0.
Bank	36	1	909	314	28	89	-884	6.55	8	17.72	160	28
Jaguar	S	39.	-		0.		-		27.9			0.
Bank	M-	305	21.7	779	44	240	1296	4.33	2	20.02	174	31

	37	8	746		42							
	S	39.	-		1.							
Jaguar	M-	307	21.9	179	70		-		35.5			0.
Bank	38	4	244	7	00	390	1837	4.17	5	20.85	21	22
	S	39.	-		0.							
Jaguar	M-	308	21.7		13		-		26.7			0.
Bank	39	1	700	517	62	74	1339	4.31	7	14.06	141	14
	S	39.	-		0.							
Jaguar	M-	312	21.7		01		-	13.1	13.2			0.
Bank	40	5	753	153	58	28	1294	8	1	13.19	90	19
	S	39.	-		0.							
Jaguar	M-	316	21.7		05		-	19.8	28.1			0.
Bank	41	7	809	276	49	77	1115	0	0	24.47	135	28
	S	39.	-		0.							
Jaguar	M-	317	21.7		01		-	19.7	20.1			0.
Bank	42	8	771	164	80	43	1274	8	0	19.69	0	26
	S	39.	-		1.							
Jaguar	M-	319	21.7	177	56		-		34.1			0.
Bank	43	0	562	5	76	523	1815	2.68	2	22.29	123	29
	S	39.	-		0.							
Jaguar	M-	339	21.8		03			16.5	28.5			0.
Bank	44	1	930	214	24	59	-919	3	5	22.79	90	28
	S	39.	-		0.							
Jaguar	M-	340	21.7	105	78		-		31.4			0.
Bank	45	6	390	4	25	209	1979	1.10	5	17.84	146	20
	S	39.	-		0.							
Jaguar	M-	348	21.7		17		-		27.4			0.
Bank	46	0	427	479	01	114	2103	0.85	8	14.95	90	24
	S	39.	-		0.							
Jaguar	M-	348	21.7		35		-	12.4	31.7			0.
Bank	47	3	497	703	55	225	1949	2	9	26.53	173	32
	S	39.	-		0.							
Jaguar	M-	349	21.9		02			13.6	19.3			0.
Bank	48	0	034	205	84	34	-944	5	9	16.88	90	17
	S	39.	-		0.							
Jaguar	M-	365	21.9		05			13.0	27.1			0.
Bank	49	2	045	280	60	34	-721	1	7	19.88	0	12
	S	39.	-		0.							
Jaguar	M-	367	21.9		04			21.4	30.3			0.
Bank	50	8	013	271	83	90	-587	5	9	25.55	143	33
	S	39.	-		0.							
Jaguar	M-	402	21.9		05				24.0			0.
Bank	51	7	910	285	80	58	-957	9.85	3	17.27	0	20
	S	39.	-		0.							
Jaguar	M-	440	21.7		45		-		21.8			0.
Bank	52	7	020	880	70	120	2422	2.39	9	12.97	122	14
	S	39.	-		0.							
Jaguar	M-	452	21.7	107	88		-		28.1			0.
Bank	53	8	106	8	05	333	2175	6.87	9	21.65	2	31

	S	39.	-		0.							
Jaguar	M-	468	21.8		18				27.4			0.
Bank	54	6	135	496	20	156	-628	6.89	9	22.01	17	31
	S	39.	-		1.							
Jaguar	M-	471	21.7	151	50		-		36.3			0.
Bank	55	1	241	9	59	464	1828	2.97	8	25.75	178	31
	S	39.	-		0.							
Jaguar	M-	472	21.8		06				22.1			0.
Bank	56	0	051	308	91	54	-774	4.77	1	13.74	90	17
	S	39.	-		0.							
Jaguar	M-	474	21.8		09				24.9			0.
Bank	57	6	017	359	32	50	-754	6.85	6	14.61	12	14
	S	39.	-		0.							
Jaguar	M-	474	21.8		03			14.2	18.6			0.
Bank	58	8	062	230	79	42	-841	7	5	17.36	90	18
	S	39.	-		0.							
Jaguar	M-	476	21.8		02			9.8	22.2			0.
Bank	59	9	172	183	42	44	-678	9	8	21.08	90	24
	S	39.	-		0.							
Jaguar	M-	478	21.8		27				25.3			0.
Bank	60	6	408	673	87	186	-741	2.47	1	19.57	8	28
	S	39.	-		0.							
Jaguar	M-	478	21.7		09				24.7			0.
Bank	61	7	999	364	50	5[illegible]	-810	1.25	9	12.05	165	14
	S	39.	-		0.							
Jaguar	M-	480	21.8		0[illegible]							0.
Bank	62	4	312	105	7[illegible]	10	-576	5.24	6.17	5.71	90	09
	S	39.	-		0.							
Jaguar	M-	481	21.8		05				17.6			0.
Bank	63	5	295	285	90	30	-572	1.48	4	9.55	90	10
	S	39.	-		0.							
Jaguar	M-	483	21.8		02			10.6	21.1			0.
Bank	64	1	319	187	56	32	-616	9	3	15.91	0	17
	S	39.	-		0.							
Jaguar	M-	483	21.7		29				33.7			0.
Bank	65	2	930	637	85	190	-862	9.63	5	22.13	45	30
	S	39.	-		0.							
Jaguar	M-	483	21.8		12				29.4			0.
Bank	66	3	350	448	22	150	-641	1.85	5	19.55	163	33
	S	39.	-		0.							
Jaguar	M-	485	21.8		41				30.4			0.
Bank	67	4	120	771	55	183	-881	4.39	6	19.97	76	24
	S	39.	-		0.							
Jaguar	M-	485	21.7		43		-	12.2	48.8			0.
Bank	68	5	406	769	62	347	1400	2	6	28.62	12	45
	S	39.	-		0.							
Jaguar	M-	485	21.7		08				15.5			0.
Bank	69	8	824	342	34	27	-825	3.30	1	10.81	27	08
Jaguar	S	39.	-		0.				25.4			0.
Bank	M-	487	21.8	299	06	73	-699	6.74	2	19.22	0	25

	70	6	285		51							
	S	39.	-		0.							
Jaguar	M-	487	21.7		16			11.5	26.6			0.
Bank	71	9	866	474	62	145	-938	2	5	20.68	15	31
	S	39.	-		0.							
Jaguar	M-	489	21.8		09				23.9			0.
Bank	72	8	316	361	28	68	-777	4.05	7	15.10	63	19
	S	39.	-		0.							
Jaguar	M-	491	21.8		04			12.4	23.0			0.
Bank	73	0	282	246	47	31	-795	0	7	18.01	0	12
	S	39.	-		0.							
Jaguar	M-	491	21.7		06				12.9			0.
Bank	74	8	756	321	92	19	-781	3.31	5	7.23	0	06
	S	39.	-		0.							
Jaguar	M-	494	21.7		06				17.4			0.
Bank	75	2	810	294	08	58	-874	1.86	9	10.76	0	20
	S	39.	-		0.							
Jaguar	M-	494	21.7		03				11.1			0.
Bank	76	4	708	224	47	8	-741	4.31	4	7.28	0	03
	S	39.	-		0.							
Jaguar	M-	497	21.7		08				24.2			0.
Bank	77	2	606	357	48	53	-742	0.70	4	13.82	13	15
	S	39.	-		0.							
Jaguar	M-	497	21.7		16				24.0			0.
Bank	78	7	764	484	90	75	-792	9.99	9	17.91	42	18
	S	39.	-		0.							
Jaguar	M-	498	21.7		06				18.8			0.
Bank	79	2	692	301	57	54	-761	2.44	3	11.27	45	18
	S	39.	-		0.							
Jaguar	M-	502	21.7		06				13.8			0.
Bank	80	2	658	296	36	25	-738	2.66	0	9.47	173	08
	S	39.	-		0.							
Jaguar	M-	505	21.7		03			11.0	15.8			0.
Bank	81	4	584	226	54	13	-817	1	5	13.21	0	06
	S	39.	-		0.							
Jaguar	M-	506	21.7	111	45				26.5			0.
Bank	82	0	812	3	28	371	-984	7.70	2	17.26	78	33
	S	39.	-		0.							
Jaguar	M-	511	21.7		06				20.3			0.
Bank	83	5	749	303	54	53	-810	7.18	7	13.60	0	17
	S	39.	-		0.							
Jaguar	M-	511	21.8	114	83		-		32.3			0.
Bank	84	8	014	3	77	271	1242	6.21	3	22.89	81	24
	S	39.	-		0.							
Jaguar	M-	515	21.7		10				19.9			0.
Bank	85	5	709	382	47	44	-847	1.47	8	12.01	165	12
	S	39.	-		0.							
Jaguar	M-	517	21.7		04			11.5	17.2			0.
Bank	86	8	577	238	04	30	-840	7	5	14.95	162	13

Jaguar Bank	S M-87	39.518 7	-21.7632	246	0.0429	26	-847	6.04	14.68	10.65	18	0.10
Jaguar Bank	S M-88	39.519 5	-21.7537	240	0.0402	37	-910	5.03	13.21	7.73	90	0.15
Jaguar Bank	S M-89	39.521 6	-21.7568	318	0.0673	47	-908	1.53	14.62	9.62	0	0.15
Jaguar Bank	S M-90	39.521 7	-21.7448	430	0.1343	81	-965	0.58	21.39	14.97	180	0.19
Jaguar Bank	S M-91	39.522 3	-21.6697	895	0.5732	163	-2354	2.86	29.56	19.02	46	0.18
Jaguar Bank	S M-92	39.522 7	-21.7525	199	0.0280	40	-946	1.06	15.06	13.06	90	0.20
Jaguar Bank	S M-93	39.523 2	-21.7602	230	0.0355	21	-911	4.83	13.47	10.37	0	0.09
Jaguar Bank	S M-94	39.524 3	-21.8153	705	0.2932	142	-1579	3.18	27.09	18.36	44	0.20
Jaguar Bank	S M-95	39.525 9	-21.7851	431	0.1278	32	-1201	1.39	22.75	11.00	99	0.07
Jaguar Bank	S M-96	39.526 2	-21.7581	248	0.0430	44	-943	2.98	10.86	7.89	72	0.18
Jaguar Bank	S M-97	39.526 9	-21.7598	336	0.0684	37	-964	1.84	11.58	5.14	8	0.11
Jaguar Bank	S M-98	39.529 7	-21.7482	450	0.1498	96	-902	4.15	21.68	14.84	28	0.21
Jaguar Bank	S M-99	39.530 8	-21.7566	219	0.0329	21	-954	6.63	13.57	9.99	0	0.10
Jaguar Bank	S M-100	39.533 4	-21.7535	598	0.2599	143	-915	9.39	26.06	21.07	177	0.24
Jaguar Bank	S M-101	39.534 7	-21.7461	491	0.1792	79	-962	3.91	22.96	14.13	6	0.16
Jaguar Bank	S M-102	39.534 7	-21.7983	1339	1.3338	280	-1453	1.64	27.81	18.49	19	0.21

	2											
	S											
	M-	39.	-		0.							
Jaguar	10	535	21.6		12		-	12.4	27.6			0.
Bank	3	1	967	425	48	149	2041	7	7	21.92	159	35
	S											
	M-	39.	-		1.							
Jaguar	10	537	21.8	154	78		-		33.5			0.
Bank	4	5	256	1	49	399	1750	3.31	9	22.78	15	26
	S											
	M-	39.	-		0.							
Jaguar	10	540	21.7		20		-		24.1			0.
Bank	5	6	007	586	62	81	1891	5.65	5	14.97	165	14
	S											
	M-	39.	-		0.							
Jaguar	10	541	21.7		04		-		19.0			0.
Bank	6	3	501	255	49	56	1024	5.24	9	12.47	135	22
	S											
	M-	39.	-		0.							
Jaguar	10	542	21.7		15		-		30.3			0.
Bank	7	8	327	478	43	171	1018	6.09	3	23.20	70	36
	S											
	M-	39.	-		0.							
Jaguar	10	542	21.7		29		-		19.0			0.
Bank	8	9	444	880	02	124	1016	4.68	0	12.94	120	14
	S											
	M-	39.	-		0.							
Jaguar	10	543	21.6		20		-		18.0			0.
Bank	9	3	610	591	22	79	2370	3.52	8	11.27	25	13
	S											
	M-	39.	-		0.							
Jaguar	11	544	21.7		33		-		28.6			0.
Bank	0	6	048	725	26	155	1809	2.96	6	18.26	9	21
	S											
	M-	39.	-		0.							
Jaguar	11	545	21.7		02		-					0.
Bank	1	2	384	200	83	22	1060	4.61	4.85	4.73	135	11
	S											
	M-	39.	-		0.							
Jaguar	11	545	21.7		07		-		17.0			0.
Bank	2	4	561	326	34	50	1128	2.88	3	9.34	20	15
	S											
	M-	39.	-		0.							
Jaguar	11	545	21.7		03		-		10.4			0.
Bank	3	9	412	211	03	19	1024	2.65	4	6.88	0	09
	S											
	M-	39.	-		0.							
Jaguar	11	547	21.7		05		-		14.2			0.
Bank	4	9	368	279	39	37	1044	5.92	9	10.65	90	13

	SM-115	39.5482	-21.7582	277	0.0533	58	-1161	2.97	17.57	11.82	45	0.21
Jaguar Bank	SM-116	39.5486	-21.6867	751	0.4234	218	-2155	2.52	27.99	22.26	171	0.29
	SM-117	39.5498	-21.7512	263	0.0472	35	-1134	5.04	11.50	8.29	90	0.13
	SM-118	39.5509	-21.7633	488	0.1725	132	-1303	3.30	31.04	22.65	0	0.27
	SM-119	39.5524	-21.7394	270	0.0501	31	-1145	5.11	16.42	11.09	90	0.11
	SM-120	39.5531	-21.8327	702	0.3589	127	-1968	7.53	24.55	16.41	6	0.18
	SM-121	39.5582	-21.7322	384	0.1771	64	-1102	3.28	25.01	16.66	0	0.17
	SM-122	39.5640	-21.7352	825	0.5151	216	-1186	2.37	30.24	20.30	8	0.26
	SM-123	39.5642	-21.7684	512	0.1864	100	-1727	5.09	26.07	16.51	164	0.20
	SM-124	39.5670	-21.7048	774	0.3765	232	-1748	4.52	30.64	22.91	59	0.30
	SM-125	39.5679	-21.7302	281	0.0563	57	-1313	5.63	24.45	14.91	30	0.20
	SM-126	39.5725	-21.8070	2073	1.4961	275	-2051	2.12	27.90	15.40	127	0.13
Jaguar Bank	SM-	39.572	-21.6	747	0.30	209	-1880	10.65	32.22	22.72	169	0.28

	127	6	992		58							
Jaguar Bank	SM-128	39.5737	-21.747	478	0.1676	71	-1982	3.27	28.37	15.20	0	0.15
Jaguar Bank	SM-129	39.5908	-21.7633	559	0.2251	81	-2091	4.67	24.67	16.40	163	0.14
Europa	SM-130	40.4731	-22.4855	722	0.3736	158	-2563	13.21	33.00	21.33	61	0.22
Europa	SM-131	40.5798	-22.4634	778	0.4515	196	-3153	5.98	31.84	23.28	60	0.25
Europa	SM-132	40.4375	-22.4616	1298	1.0031	365	-2049	7.14	30.95	22.65	99	0.28
Europa	SM-133	40.4815	-22.4445	523	0.1958	141	-2467	4.79	34.62	24.49	3	0.27
Europa	SM-134	40.4851	-22.4334	508	0.1848	143	-2463	11.63	32.04	24.85	13	0.28
Europa	SM-135	40.4428	-22.4298	639	0.2894	169	-1853	5.72	30.50	22.02	161	0.26
Europa	SM-136	40.5025	-22.4203	1012	0.6064	192	-2619	6.03	32.65	22.05	163	0.19
Europa	SM-137	40.5619	-22.4180	779	0.4355	146	-3075	6.66	30.78	20.99	157	0.19
Europa	SM-138	40.2813	-22.4174	594	0.2347	218	-1936	5.25	36.96	25.30	25	0.37
Europa	SM-139	40.1981	-22.4142	1038	0.6925	275	-2836	5.74	36.58	22.99	100	0.26

Europa	SM-140	40.5790	-22.4078	1065	0.8193	164	-3143	2.48	25.41	12.50	131	0.15
Europa	SM-141	40.2030	-22.4064	791	0.3047	127	-2812	2.86	26.59	16.54	178	0.16
Europa	SM-142	40.5556	-22.3998	1182	0.8630	208	-2995	2.65	30.09	18.02	177	0.18
Europa	SM-143	40.2391	-22.3877	1031	0.5420	226	-2410	7.92	27.79	20.11	27	0.22
Europa	SM-144	40.1755	-22.3767	334	0.0796	47	-3047	1.07	12.01	8.89	160	0.14
Europa	SM-145	40.2166	-22.3683	1606	1.8582	446	-2614	0.16	33.46	23.81	97	0.28
Europa	SM-146	40.1978	-22.3475	797	0.4419	199	-2916	3.89	27.96	15.92	179	0.25
Europa	SM-147	40.2025	-22.3177	409	0.1251	69	-2993	4.13	16.92	12.00	90	0.16
Europa	SM-148	40.1870	-22.3091	1385	1.2386	255	-3013	2.50	32.15	19.05	161	0.18
Europa	SM-149	40.1874	-22.2971	318	0.0705	84	-3021	6.19	25.59	17.76	0	0.26
Europa	SM-150	40.1826	-22.2946	430	0.1331	91	-3036	5.95	24.03	18.00	0	0.21
Europa	SM-151	40.2928	-22.2922	325	0.0713	102	-2308	16.97	23.12	20.39	135	0.31
Europa	SM-	40.226	-22.2	1146	0.80	226	-2956	1.87	32.24	21.42	166	0.20

	152S	1	685		34							
Europa	M-153S	40.2121	-22.2658	436	0.1061	40	-3081	4.77	11.33	6.66	157	0.09
Europa	M-154S	40.3219	-22.2652	598	0.2492	141	-2380	3.85	27.09	19.86	97	0.24
Europa	M-155S	40.2296	-22.2604	912	0.5009	166	-2966	0.45	27.39	17.76	144	0.18
Europa	M-156S	40.1935	-22.2601	804	0.4836	143	-3048	5.00	26.89	17.18	169	0.18
Europa	M-157S	40.3126	-22.2587	642	0.3005	184	-2509	7.70	26.41	20.80	145	0.29
Europa	M-158S	40.2226	-22.2586	310	0.0694	66	-3071	13.39	19.92	16.74	90	0.21
Europa	M-159S	40.2227	-22.2525	377	0.0985	79	-3069	6.42	16.94	11.31	90	0.21
Europa	M-160S	40.4302	-22.2521	654	0.3127	144	-2696	3.02	27.79	17.33	136	0.22
Europa	M-161S	40.3974	-22.2488	747	0.4124	208	-2538	9.20	29.74	20.50	163	0.28
Europa	M-162S	40.2562	-22.2472	869	0.5443	206	-2907	1.91	32.23	20.72	165	0.24
Europa	M-163S	40.2087	-22.2467	338	0.0815	55	-3086	7.44	13.59	11.33	165	0.16
Europa	M-164	40.2092	-22.2421	260	0.0471	40	-3058	2.33	18.43	11.81	18	0.16

Europa	SM-165	40.2058	-22.2384	846	0.5286	128	-3048	1.25	26.72	13.01	37	0.15
Europa	SM-166	40.4249	-22.2381	1429	1.5159	334	-2704	6.35	31.90	21.46	174	0.23
Europa	SM-167	40.2456	-22.2378	334	0.0785	54	-3026	7.59	15.21	10.50	20	0.16
Europa	SM-168	40.3405	-22.2322	478	0.1641	120	-2634	8.61	25.54	18.74	165	0.25
Europa	SM-169	40.3762	-22.2258	722	0.3722	135	-2696	4.92	29.36	18.33	107	0.19
Europa	SM-170	40.2779	-22.2252	642	0.2101	120	-2969	1.87	22.93	13.83	125	0.19
Europa	SM-171	40.2243	-22.2228	341	0.0857	49	-3081	3.92	12.07	7.41	90	0.14
Europa	SM-172	40.2431	-22.2172	156	1.1024	271	-2997	6.01	29.78	19.90	55	0.20
Europa	SM-173	40.2726	-22.2151	331	0.0769	34	-3017	1.79	7.81	5.58	63	0.10
Ptolemee	SM-174	40.2579	-22.2133	2338	2.0605	256	-2979	1.95	32.86	18.29	140	0.11
Ptolemee	SM-175	40.4141	-22.2119	646	0.3042	160	-2876	10.52	30.98	22.32	23	0.25
Ptolemee	SM-176	40.2378	-22.2097	334	0.0788	63	-3054	8.46	18.17	13.84	45	0.19
Ptolemee	SM-	40.240	-22.1	683	0.34	130	-3009	5.39	24.97	18.98	80	0.19

	177S	9	999		53							
Ptolemee	M-178S	40.2596	-22.1992	749	0.4185	171	-2978	8.58	30.25	23.42	26	0.23
Ptolemee	M-179S	40.2537	-22.1985	425	0.1248	90	-3036	6.37	19.96	14.26	173	0.21
Ptolemee	M-180S	40.2266	-22.1984	1804	2.0422	353	-2911	5.36	33.64	23.90	132	0.20
Ptolemee	M-181S	40.2044	-22.1939	473	0.1659	85	-3037	7.26	18.13	13.76	0	0.18
Ptolemee	M-182S	40.2551	-22.1934	141	0.0121	10	-30[illegible]4	4.33	4.54	4.44	90	0.07
Ptolemee	M-183S	40.2504	-22.1922	745	0.3772	206	-2990	7.13	29.29	21.84	71	0.28
Ptolemee	M-184S	40.2555	-22.1904	323	0.0618	95	-3060	6.95	24.95	17.20	18	0.29
Ptolemee	M-185S	40.2183	-22.1[illegible]	790	0.4398	211	-2929	8.15	28.17	21.52	26	0.27
Ptolemee	M-186S	40.3233	-22.1895	534	0.2022	70	-3036	6.18	22.44	13.77	51	0.13
Ptolemee	M-187S	40.2460	-22.1881	624	0.2756	186	-2990	6.36	25.11	16.58	58	0.30
Ptolemee	M-188S	40.2565	-22.1869	425	0.1107	54	-3013	7.22	16.49	11.87	81	0.13
Ptolemee	M-189S	40.3201	-22.1857	700	0.2227	87	-3065	2.64	21.34	12.55	51	0.12

Ptolemee	SM-190	40.2815	-22.1843	365	0.0981	39	-3038	3.93	16.02	9.68	15	0.11
Ptolemee	SM-191	40.2140	-22.1836	1102	0.8383	285	-2848	7.61	31.88	24.41	53	0.26
Ptolemee	SM-192	40.2775	-22.1798	496	0.1772	81	-3013	6.24	23.16	14.86	137	0.16
Ptolemee	SM-193	40.2705	-22.1781	711	0.3534	149	-2947	6.49	29.32	22.01	112	0.21
Ptolemee	SM-194	40.3151	-22.1766	424	0.1267	58	-3072	7.04	18.39	12.14	90	0.14
Ptolemee	SM-195	40.2549	-22.1751	856	0.5386	163	-2933	4.29	25.82	19.03	168	0.19
Ptolemee	SM-196	40.2913	-22.1666	345	0.0875	29	-3056	2.78	11.82	6.79	0	0.09
Ptolemee	SM-197	40.2022	-22.1662	2420	3.2893	387	-2586	1.49	31.49	22.07	130	0.16
Ptolemee	SM-198	40.2525	-22.1596	1821	1.6689	304	-2888	6.27	33.10	20.84	149	0.17
Ptolemee	SM-199	40.2769	-22.1577	1604	1.9441	280	-2921	0.35	34.91	16.72	6	0.17
Ptolemee	SM-200	40.2245	-22.1541	1575	1.3751	289	-2671	4.47	31.61	21.60	5	0.18
Ptolemee	SM-201	40.3416	-22.1434	868	0.4832	154	-3061	5.00	29.23	19.36	11	0.18
Ptolemee	SM-	40.225	-22.1	664	0.31	144	-2615	9.25	32.29	23.18	119	0.22

	202S	6	418		70							
Ptolemee	M-203S	40.2789	-22.1411	344	0.0854	17	-3050	2.98	8.58	5.56	6	0.05
Ptolemee	M-204S	40.1784	-22.1408	2327	4.1064	627	-2337	5.94	37.85	22.94	83	0.27
Ptolemee	M-205S	40.2003	-22.1408	2003	1.9276	281	-2398	0.99	22.96	15.13	86	0.14
Ptolemee	M-206S	40.2390	-22.1387	1403	1.3923	335	-2727	2.69	31.27	22.33	162	0.24
Ptolemee	M-207S	40.3368	-22.1379	408	0.1089	34	-3008	2.26	11.78	7.67	37	0.08
Ptolemee	M-208S	40.2040	-22.1169	1919	2.6744	435	-2349	6.29	27.88	19.93	21	0.23
Ptolemee	M-209S	40.2343	-22.1156	922	0.4340	195	-2660	7.00	26.91	18.62	10	0.21
Ptolemee	M-210S	40.1503	-22.1125	2924	4.0554	574	-2261	5.06	35.08	24.92	112	0.20
Ptolemee	M-211S	40.4491	-22.1125	296	0.0617	48	-3143	2.46	7.55	4.84	0	0.16
Ptolemee	M-212S	40.0251	-22.1121	428	0.1222	58	-2742	11.27	19.84	15.00	70	0.13
Ptolemee	M-213S	40.4617	-22.1062	615	0.2232	86	-3099	3.80	21.96	13.14	10	0.14
Ptolemee	M-214	40.4540	-22.1061	197	0.0236	18	-3132	4.45	4.94	4.69	90	0.09

Ptolemee	SM-215	40.1954	-22.0956	1098	0.8992	301	-2366	4.53	32.39	23.90	21	0.27
Ptolemee	SM-216	40.0118	-22.0955	1301	1.0120	181	-2689	3.16	27.99	17.75	92	0.14
Ptolemee	SM-217	40.1825	-22.0944	1695	2.1714	429	-2207	2.26	39.21	23.27	168	0.25
Ptolemee	SM-218	40.1332	-22.0843	3153	4.4334	643	-2122	4.02	32.92	21.49	78	0.20
Ptolemee	SM-219	40.1866	-22.0820	934	0.6183	252	-2406	8.70	26.40	19.76	9	0.27
Ptolemee	SM-220	40.1705	-22.0793	449	0.1458	4[illegible]	-2378	4.32	15.10	10.52	90	0.11
Ptolemee	SM-221	40.1583	-22.0724	3307	[illegible]	582	-2152	1.70	34.18	21.30	97	0.18
Ptolemee	SM-222	40.0287	-22.0724	162[illegible]	1.6917	271	-2476	1.71	33.60	22.51	81	0.17
Ptolemee	SM-223	40.[illegible]1278	22.0651	1447	1.4294	409	-1859	4.37	31.80	24.88	171	0.28
Ptolemee	SM-224	40.1377	-22.0425	1361	1.2087	381	-1939	1.78	31.44	22.91	138	0.28
Ptolemee	SM-225	40.1152	-22.0402	1147	0.9472	329	-1823	3.38	32.08	21.84	23	0.29
Ptolemee	SM-226	40.1335	-22.0322	820	0.4024	246	-1761	1.03	30.67	20.92	134	0.30
Ptolemee	SM-[illegible]	40.118	-22.0	1161	1.02	293	-1535	5.06	34.36	23.96	10	0.25

	227S	8	289		30							
Ptolemee	SM-228S	40.0612	-22.0235	712	0.3714	163	-1722	4.88	29.60	21.76	170	0.23
Ptolemee	SM-229S	40.0497	-22.0115	1024	0.7590	210	-1655	2.09	29.89	22.50	36	0.20
Ptolemee	SM-230S	40.1175	-22.0036	2196	3.1086	658	-1235	5.44	31.63	22.28	43	0.30
Ptolemee	SM-231S	40.0790	-22.0033	985	0.7086	257	-1245	4.57	34.91	21.02	4	0.26
Ptolemee	SM-232S	40.1344	-21.9988	480	0.1695	97	-1651	4.96	29.08	16.82	0	0.20
Ptolemee	SM-233S	40.1424	-21.9974	929	0.4868	279	-1775	7.48	31.55	23.89	32	0.30
Ptolemee	SM-234S	40.1529	-21.9937	484	0.1181	76	-1999	2.52	21.45	11.89	12	0.16
Ptolemee	SM-235S	40.1081	-21.9903	1632	1.7819	384	-1043	4.43	28.08	20.61	11	0.24
Ptolemee	SM-236S	40.0293	-21.9871	484	0.1622	125	-1957	3.50	25.79	16.72	9	0.26
Ptolemee	SM-237S	40.0903	-21.9858	2102	2.0607	286	-939	2.81	36.65	17.74	31	0.14
Ptolemee	SM-238S	40.0120	-21.9852	977	0.7085	301	-1899	7.95	34.28	26.39	136	0.31
Ptolemee	SM-239S	40.2552	-21.9842	535	0.2069	101	-2797	7.46	24.40	15.58	18	0.19

Ptolemee	SM-240	40.1875	-21.9826	535	0.1919	154	-2280	9.02	31.39	20.95	2	0.29
Ptolemee	SM-241	40.0316	-21.9812	207	0.0304	40	-1978	7.87	17.18	12.66	0	0.19
Ptolemee	SM-242	40.2157	-21.9796	882	0.5604	194	-2542	3.57	28.96	15.53	14	0.22
Ptolemee	SM-243	40.0300	-21.9793	228	0.0359	59	-2030	6.33	14.25	9.95	162	0.26
Ptolemee	SM-244	40.0409	-21.9790	1279	1.2192	404	-1854	8.17	31.57	24.71	177	0.32
Ptolemee	SM-245	40.1978	-21.9784	898	0.4830	307	-2364	9.22	36.37	26.97	174	0.34
Ptolemee	SM-246	40.0328	-21.9780	192	0.0237	31	-2038	4.45	10.45	6.98	0	0.16
Ptolemee	SM-247	40.0324	-21.9759	252	0.0466	60	-2066	11.38	16.57	13.89	162	0.24
Ptolemee	SM-248	40.2641	-21.9757	829	0.4460	130	-2837	2.68	28.35	16.91	25	0.16
Ptolemee	SM-249	40.0802	-21.9746	404	0.1178	141	-1271	10.61	28.20	21.01	70	0.35
Ptolemee	SM-250	40.0181	-21.9736	2805	3.8161	511	-1887	3.63	33.56	21.69	125	0.18
Ptolemee	SM-251	40.1749	-21.9735	748	0.4009	255	-2218	7.23	34.27	22.68	24	0.34
Ptolemee	SM-	40.094	-21.9	441	0.13	83	-1030	8.73	28.69	15.97	114	0.19

	252S	5	723		94							
Ptolemee	M-253S	40.1866	-21.9723	1284	1.2363	398	-2204	8.27	32.89	25.91	8	0.31
Ptolemee	M-254S	40.0490	-21.9716	1004	0.6214	410	-1812	1.47	32.10	22.36	155	0.41
Ptolemee	M-255S	40.0312	-21.9704	482	0.1404	114	-2120	4.12	27.50	16.97	161	0.24
Ptolemee	M-256S	40.2423	-21.9697	2781	3.0343	391	-2600	2.36	38.83	21.46	12	0.14
Ptolemee	M-257S	40.0780	-21.9691	557	0.2218	177	-1338	5.52	40.83	20.73	86	0.32
Ptolemee	M-258S	40.0673	-21.9687	2185	2.4146	637	-1388	4.47	33.60	23.69	87	0.29
Ptolemee	M-259S	40.2206	-21.9685	1201	0.2569	247	-2439	1.11	29.65	18.73	23	0.21
Ptolemee	M-260S	40.2040	-21.9683	1818	2.2260	440	-2175	3.48	31.72	24.21	5	0.24
Ptolemee	M-261S	40.0974	-21.9660	547	0.2157	177	-1179	9.01	29.39	23.89	135	0.32
Ptolemee	M-262S	40.0910	-21.9656	589	0.2517	157	-1256	2.91	35.92	21.75	90	0.27
Ptolemee	M-263S	40.1068	-21.9635	260	0.0453	77	-1415	14.98	20.78	18.81	90	0.30
Ptolemee	M-264S	40.2127	-21.9582	1262	1.1762	498	-2286	3.43	32.01	26.41	171	0.39

Ptolemee	SM-265	40.0941	-21.9566	1299	1.0959	371	-1449	2.41	33.24	23.14	46	0.29
Ptolemee	SM-266	40.0560	-21.9548	906	0.5849	334	-1742	7.49	33.29	25.63	172	0.37
Ptolemee	SM-267	39.9147	-21.9543	1356	1.2243	289	-2758	7.18	37.36	21.42	70	0.21
Ptolemee	SM-268	40.1161	-21.9503	517	0.1899	164	-1775	1.48	31.94	19.76	83	0.32
Ptolemee	SM-269	40.1884	-21.9448	675	0.3279	184	-2449	11.93	31.89	23.15	3	0.27
Ptolemee	SM-270	40.5801	-21.9394	510	0.1913	105	-3044	3.36	21.46	14.64	47	0.21
Ptolemee	SM-271	40.1676	-21.9392	1598	1.0265	418	-2371	8.46	37.04	24.79	41	0.26
Ptolemee	SM-272	40.2108	-21.9357	114	0.7052	167	-2572	5.82	31.37	20.16	65	0.15
Ptolemee	SM-273	40.1168	-21.9345	1740	2.2083	448	-1884	6.21	30.39	23.37	1	0.26
Ptolemee	SM-274	40.1718	-21.9297	441	0.1306	92	-2510	4.43	20.80	13.23	172	0.21
Ptolemee	SM-275	40.1410	-21.9293	2003	2.8048	574	-2140	7.49	34.92	24.97	23	0.29
Ptolemee	SM-276	40.0345	-21.9251	3071	4.4273	515	-2308	1.32	33.10	20.37	167	0.17
Ptolemee	SM-	40.130	-21.9	1261	0.86	304	-2318	3.36	28.79	19.30	86	0.24

	277S	7	159		33							
Ptolemee	M-278S	40.0682	-21.9133	1318	1.2834	367	-2290	5.60	30.70	22.57	147	0.28
Ptolemee	M-279S	40.0581	-21.9101	844	0.5121	156	-2394	3.75	23.68	14.80	168	0.19
Ptolemee	M-280S	40.0211	-21.9011	801	0.4418	215	-2452	5.40	31.82	22.92	176	0.27
Ptolemee	M-281S	40.0535	-21.8978	412	0.1243	127	-2595	7.54	26.72	20.19	15	0.31
Ptolemee	M-282S	40.0419	-21.8952	812	0.3822	198	-2552	14.96	30.36	22.87	167	0.24
Ptolemee	M-283S	40.0323	-21.8912	795	0.4617	170	-2489	5.12	27.04	17.00	3	0.21
Ptolemee	M-284S	40.1227	-21.8867	456	0.1448	68	-2610	0.77	22.66	14.53	97	0.15
Ptolemee	M-285S	40.0758	-21.8828	815	0.4801	235	-2643	5.62	29.32	22.45	177	0.29
Ptolemee	M-286S	40.1159	-21.8829	657	0.3036	109	-2600	7.97	25.01	17.31	39	0.17
Ptolemee	M-287S	40.0095	-21.8780	1074	0.8207	274	-2653	2.10	34.25	20.32	1	0.25
Ptolemee	M-288S	40.0750	-21.8749	667	0.2936	128	-2698	3.22	24.54	16.47	30	0.19
Ptolemee	M-289S	40.0209	-21.8690	993	0.5388	269	-2684	4.01	30.80	19.82	81	0.27

Ptolemee	SM-290	40.1324	-21.8679	605	0.2298	117	-2687	3.39	22.48	15.42	113	0.19
Ptolemee	SM-291	40.0092	-21.8600	348	0.0732	64	-2824	2.90	19.21	13.44	135	0.18
Pammela Seamount 2	SM-292	40.1214	-21.8506	1967	1.3573	383	-2380	3.12	33.65	21.32	131	0.19
Pammela Seamount 2	SM-293	40.0565	-21.8420	1907	2.3159	479	-2609	5.38	37.20	23.08	180	0.25
Pammela Seamount 2	SM-294	40.1687	-21.8226	1182	0.9844	175	-2508	1.39	25.18	16.56	169	0.15
Pammela Seamount 2	SM-295	40.0961	-21.8183	1588	1.8965	401	-2112	2.94	30.34	20.89	176	0.25
Pammela Seamount 2	SM-296	40.0451	-21.8087	1683	2.[illegible]03	557	-2618	10.14	35.11	26.72	161	0.33
Pammela Seamount 2	SM-297	40.1770	-21.8028	751	0.4056	151	-2595	3.33	29.89	18.69	147	0.20
Pammela Seamount 2	SM-298	40.0322	-21.7977	1059	0.5534	228	-2752	2.29	28.18	19.11	168	0.22
Pammela Seamount 2	SM-299	40.0502	-21.7934	1278	1.1412	374	-2504	4.21	31.26	24.53	177	0.29
Pammela Seamount 2	SM-300	40.1493	-21.7929	815	0.4617	123	-2210	0.66	27.01	15.60	51	0.15
Pammela Seamount 2	SM-301	40.1312	-21.7924	696	0.3283	112	-1970	1.43	27.90	13.88	179	0.16
Pammela	SM-	40.079	-21.7	0	1.11	319	-2413	4.19	29.50	16.72	174	0.23

Seamount 2	302	3	880		96							
Pammela Seamount 2	SM-303	40.1340	-21.7841	379	0.1019	47	-2053	7.02	17.39	12.78	165	0.12
Pammela Seamount 2	SM-304	40.0199	-21.7835	1865	2.5414	482	-2619	0.53	36.26	25.25	108	0.26
Pammela Seamount 2	SM-305	40.0305	-21.7726	1892	2.6372	510	-2591	6.77	32.72	23.53	160	0.27
Pammela Seamount 2	SM-306	40.0719	-21.7667	1028	0.7302	178	-2586	2.74	26.19	17.20	94	0.17
Pammela Seamount 2	SM-307	40.1643	-21.7659	1334	0.9339	211	-2554	3.98	34.25	19.16	149	0.16
Pammela Seamount 2	SM-308	40.0994	-21.7556	3826	0.1026	89	-2671	3.06	22.25	15.80	0	0.23
Pammela Seamount 2	SM-309	40.0184	-21.7509	2511	3.2037	519	-2711	2.51	34.57	22.06	29	0.21
Pammela Seamount 2	SM-310	40.1097	-21.7229	417	0.1271	79	-2885	3.58	15.52	11.48	135	0.19
Pammela Seamount 2	SM-311	40.0035	-21.7221	1152	0.9367	369	-2525	5.39	33.22	24.35	133	0.32
Pammela Seamount 2	SM-312	40.0233	-21.7293	1032	0.5917	116	-2831	3.33	23.13	12.98	159	0.11
Pammela Seamount 1	SM-313	40.1880	-21.7820	2256	2.4675	375	-2803	1.18	32.54	19.86	31	0.17
Pammela Seamount 1	SM-314	39.9816	-21.7420	465	0.1573	80	-2828	6.13	19.89	14.00	146	0.17

Pammel a Seamount 1	S M-315	39.9871	-21.7248	1278	1.1788	443	-2433	3.46	31.24	25.15	60	0.35
Pammel a Seamount 1	S M-316	40.0270	-21.6916	794	0.4558	167	-2608	2.32	25.37	18.53	125	0.21
Pammel a Seamount 1	S M-317	40.1066	-21.6756	578	0.2430	118	-2891	3.62	26.97	15.68	125	0.20
Pammel a Seamount 1	S M-318	40.1136	-21.6952	2436	3.8488	335	-2841	0.65	39.12	15.13	21	0.14
Pammel a Seamount 1	S M-319	40.0679	-21.6638	3027	4.0961	318	-2680	0.43	30.83	16.74	178	0.10
Pammel a Seamount 1	S M-320	39.9771	-21.6634	759	0.4228	217	-1744	2.64	29.66	20.00	4	0.29
Pammel a Seamount 1	S M-321	39.9718	-21.6549	870	0.5385	191	-1512	5.31	29.96	20.82	120	0.22
Pammel a Seamount 1	S M-322	39.9636	-21.6524	600	0.2852	140	-1395	4.44	31.11	17.81	31	0.22
Pammel a Seamount 1	S M-323	40.0587	-21.6498	569	0.1672	57	-2665	6.04	16.75	11.36	177	0.10
Pammel a Seamount 1	S M-324	40.0349	-21.6470	1763	1.0853	177	-2497	3.71	28.12	14.82	90	0.10
Pammel a Seamount 1	S M-325	40.0552	-21.6437	1149	0.7211	149	-2631	1.05	26.59	14.16	30	0.13
Pammel a Seamount 1	S M-326	40.0639	-21.6368	874	0.5564	149	-2650	3.39	23.49	15.17	3	0.17
Pammel a	S M-	40.040	-21.6	1230	1.113	290	-2524	1.26	32.49	22.09	14	0.24

Seamount 1	327	4	300		98							
Pammela Seamount 1	SM-328	40.0719	-21.6257	3038	52.32	301	-2567	2.89	36.85	18.30	161	0.10
Pammela Seamount 1	SM-329	40.0940	-21.6229	1398	0.4911	87	-2633	1.28	27.27	13.53	103	0.06
Pammela Seamount 1	SM-330	40.1079	-21.6212	599	0.2436	84	-2763	3.83	23.16	15.34	137	0.14
Pammela Seamount 1	SM-331	40.1734	-21.6196	1155	0.9716	221	-3043	1.99	34.79	16.89	35	0.19
Pammela Seamount 1	SM-332	40.1197	-21.6063	427	0.1257	59	-2744	7.87	19.54	14.03	171	0.14
Pammela Seamount 1	SM-333	40.1427	-21.6037	809	0.4778	214	-2981	5.04	27.80	19.37	173	0.26
Pammela Seamount 1	SM-334	39.8908	-21.4601	128	1.2109	263	-2700	1.46	35.70	17.34	179	0.20
Pammela Seamount 1	SM-335	39.9389	-21.4577	911	0.4792	115	-3013	3.54	26.94	15.84	51	0.13
Pammela Seamount 1	SM-336	39.9453	-21.4471	1101	0.9204	264	-3007	2.68	33.17	21.66	0	0.24
Pammela Seamount 1	SM-337	39.9421	-21.4391	889	0.3473	136	-3049	7.27	24.41	16.01	43	0.15
Pammela Seamount 1	SM-338	40.0784	-21.5942	548	0.2150	148	-2746	1.92	31.58	23.03	3	0.27
Pammela Seamount 1	SM-339	40.1435	-21.5896	750	0.3979	103	-3026	6.57	22.73	14.76	133	0.14

Pammel	S											
a	M-	39.	-		0.							
Seamou	34	914	21.5		49		-		27.3			0.
nt 1	0	5	839	812	96	186	1794	1.83	7	18.36	1	23
Pammel	S											
a	M-	39.	-		0.							
Seamou	34	920	21.5		12		-		21.6			0.
nt 1	1	8	765	443	57	71	1969	4.55	4	15.51	7	16
Pammel	S											
a	M-	39.	-		0.							
Seamou	34	924	21.5	116	94		-		32.6			0.
nt 1	2	0	696	0	58	281	2046	0.59	8	21.99	178	24
Pammel	S											
a	M-	40.	-		0.							
Seamou	34	151	21.6		63		-		13.3			0.
nt 1	3	0	259	914	45	75	2985	2.48	7	9.08	21	08
Pammel	S											
a	M-	39.	-		4.							
Seamou	34	629	21.6	421	05		-		33.4			0.
nt 1	4	5	182	9	05	666	1535	1.44	5	21.92	64	16
Pammel	S											
a	M-	39.	-		1.							
Seamou	34	859	21.5	138	31		-		46.2			0.
nt 1	5	3	794	1	22	292	1799	2.87	7	21.99	9	21
Pammel	S											
a	M-	39.	-		1							
Seamou	34	815	21.5	129	25		-		28.9			0.
nt 1	6	3	787	9	85	275	1882	5.98	1	19.32	176	21
Pammel	S											
a	M-	39.	-		0.							
Seamou	34	872	21.5	113	94		-		27.8			0.
nt 1	7	1	725	6	33	199	1908	0.42	3	12.61	176	17
Pammel	S											
a	M-	39.	-		0.							
Seamou	34	841	21.5	114	65		-		25.9			0.
nt 1	8	6	712	3	06	160	1974	2.23	8	17.44	120	14
Pammel	S											
a	M-	39.	-		1.							
Seamou	34	801	21.5	125	15		-		27.7			0.
nt 1	9	7	683	7	43	264	1737	0.66	0	17.97	173	21
Pammel	S											
a	M-	39.	-		0.							
Seamou	35	836	21.5		34		-		27.3			0.
nt 1	0	1	586	983	33	138	2034	1.71	1	17.66	153	14
Pammel	S											
a	M-	39.	-		0.							
Seamou	35	907	21.5		11		-		19.1			0.
nt 1	1	9	569	415	82	70	2195	5.97	2	12.80	148	17
Pammel	S	39.	-	231	2.		-		33.1			0.
a	M-	804	21.5	6	19	511	1612	3.44	9	22.36	140	22

Seamount 1 Pammela	352 SM-353	3 39.8240	539 21.5533	971	34 0.5580	230	-1892	6.90	31.05	22.36	156	0.24
Seamount 1 Pammela	354 SM-355	39.8870 39.8507	21.5510 21.5437	1037 1432	0.7495 1.3776	197 291	-2184 -2017	4.88 5.41	35.28 34.57	22.09 23.08	32 138	0.19 0.20
Seamount 1 Pammela	356 SM-357	39.8186 39.8766	21.5437 21.5408	980 346	0.5121 0.0799	196 45	-1812 -2335	8.09 6.54	31.84 19.50	20.91 13.44	30 135	0.20 0.13
Seamount 1 Pammela	358 SM-359	39.8351 39.8001	21.5405 21.5391	1211 419	0.7148 0.1105	222 59	-1959 -1628	3.42 5.85	30.04 20.68	18.41 14.81	90 58	0.18 0.14
Seamount 1 Pammela	360 SM-361	39.9467 39.8622	21.5311 21.5253	1457 1679	1.1497 2.0963	223 309	-2657 -2067	0.92 3.83	26.47 24.02	15.34 16.92	33 169	0.15 0.18
Bassas da India	SM-362	39.6091	21.7808	714	0.3751	123	-2199	2.89	25.38	15.09	166	0.17
Bassas da India	SM-363	39.6114	21.7542	1599	1.4247	319	-2159	0.32	29.80	20.08	2	0.20
Bassas da India	SM-364	39.5773	21.7479	821	0.4894	332	-1518	6.44	36.20	28.56	159	0.40

Bassas da India	SM-365	39.5854	-21.7318	766	0.4220	212	-1559	5.46	35.60	25.51	157	0.28
Bassas da India	SM-366	39.6269	-21.7275	1403	1.2688	353	-1993	9.91	33.59	22.94	23	0.25
Bassas da India	SM-367	39.5864	-21.7274	402	0.1108	35	-1596	0.96	18.05	9.42	164	0.09
Bassas da India	SM-368	39.6134	-21.7237	360	0.0933	50	-1899	5.98	23.88	14.53	135	0.14
Bassas da India	SM-369	39.5908	-21.7231	627	0.2656	106	-1651	2.97	24.54	15.68	157	0.17
Bassas da India	SM-370	39.6012	-21.7208	667	0.3100	130	-1563	6.78	28.01	21.41	53	0.20
Bassas da India	SM-371	39.5815	-21.7202	395	0.0942	36	-1564	4.70	21.20	13.47	52	0.09
Bassas da India	SM-372	39.5967	-21.7156	713	0.3408	231	-1536	7.30	28.38	21.49	21	0.32
Bassas da India	SM-373	39.6472	-21.7150	713	0.3733	148	-2344	1.29	26.43	18.44	4	0.21
Bassas da India	SM-374	39.6047	-21.7963	564	0.2340	88	-2099	9.71	25.90	18.31	17	0.16
Bassas da India	SM-375	39.6679	-21.7132	1063	0.8432	206	-2460	5.49	26.51	19.01	14	0.19
Bassas da India	SM-376	39.5999	-21.7097	879	0.5475	218	-1512	0.97	30.24	21.47	116	0.25
Bassas da India	SM-	39.992	-21.7	373	0.09	26	-2341	0.55	7.40	3.79	15	0.07

	377S	4	085		54							
Bassas da India	M-378S	39.5757	-21.7071	358	0.0886	42	-1878	1.25	13.96	8.89	165	0.12
Bassas da India	M-379S	39.6146	-21.7039	1213	1.0603	297	-1798	4.52	31.08	21.46	154	0.24
Bassas da India	M-380S	39.6510	-21.7012	618	0.2543	114	-2364	6.14	27.42	17.14	74	0.19
Bassas da India	M-381S	40.0946	-21.6963	459	0.1254	45	-2903	2.38	13.08	8.25	115	0.10
Bassas da India	M-382S	39.5847	-21.6905	563	0.1914	84	-2022	0.84	21.75	12.74	75	0.15
Bassas da India	M-383S	39.6015	-21.6893	368	0.0938	46	-1739	7.80	25.79	16.74	131	0.13
Bassas da India	M-384S	39.5811	-21.6880	599	0.1520	48	-2049	4.73	23.77	11.58	64	0.08
Bassas da India	M-385S	39.5985	-21.6766	1985	2.9929	469	-1747	2.77	32.63	23.96	165	0.24
Bassas da India	M-386S	39.6122	-21.6734	431	0.1347	51	-1926	3.64	20.95	11.98	90	0.12
Bassas da India	M-387S	39.6184	-21.6716	753	0.3899	107	-2017	3.18	23.95	14.29	122	0.14
Bassas da India	M-388S	39.6115	-21.6680	300	0.0638	38	-1940	2.71	10.39	7.78	0	0.13
Bassas da India	M-389S	39.5873	-21.6653	666	0.3155	152	-1974	8.37	30.63	21.59	176	0.23

Bassas da India	SM-390	39.6136	-21.6634	293	0.0587	24	-1846	7.96	22.06	14.41	72	0.08
Bassas da India	SM-391	39.6096	-21.6585	771	0.4441	171	-1723	8.33	26.18	20.81	152	0.22
Bassas da India	SM-392	39.6382	-21.6565	1665	1.7486	348	-1959	2.13	32.04	22.21	37	0.21
Bassas da India	SM-393	39.5842	-21.6557	1384	0.9138	321	-2136	3.32	31.30	19.36	103	0.23
Bassas da India	SM-394	39.5942	-21.6552	358	0.0938	49	-2139	3.94	11.82	7.59	75	0.14
Bassas da India	SM-395	39.6265	-21.6546	816	0.2793	79	-2004	1.58	22.59	11.35	58	0.10
Bassas da India	SM-396	39.6166	-21.6529	590	0.2562	108	-1808	3.03	25.52	14.21	157	0.18
Bassas da India	SM-397	39.6960	-21.6524	688	0.2625	126	-2431	7.28	26.59	19.48	153	0.18
Bassas da India	SM-398	39.6470	-21.6483	824	0.3721	259	-2055	4.39	29.00	21.91	5	0.31
Bassas da India	SM-399	39.6760	-21.6462	2525	3.3384	463	-2236	3.48	33.59	21.19	98	0.18
Bassas da India	SM-400	39.5951	-21.6437	1811	2.4766	407	-2064	2.75	32.10	20.62	32	0.22
Bassas da India	SM-401	40.0279	-21.6147	1359	1.1202	208	-2520	1.62	30.09	15.31	99	0.15
Bassas da India	SM-	39.624	-21.6	1482	1.33	477	-1563	3.38	32.10	23.42	46	0.32

	402S	6	081		42							
Bassas da India	M-403S	39.6469	-21.6014	516	0.1801	83	-1347	10.05	26.53	19.16	147	0.16
Bassas da India	M-404S	39.7034	-21.6007	567	0.2315	134	-1699	5.37	29.99	21.59	110	0.24
Bassas da India	M-405S	39.6148	-21.6006	1286	1.0430	325	-1704	4.87	31.22	23.90	86	0.25
Bassas da India	M-406S	39.6260	-21.5859	1211	0.7049	269	-1535	3.27	31.55	22.83	79	0.22
Bassas da India	M-407S	39.8552	-21.5721	253	0.0405	22	-2078	1.92	11.96	6.68	0	0.09
Bassas da India	M-408S	39.6350	-21.5716	492	0.1772	150	-1089	8.40	30.05	20.96	31	0.30
Bassas da India	M-409S	39.8517	-21.5707	293	0.0611	44	-2040	3.80	11.33	9.09	0	0.15
Bassas da India	M-410S	39.8863	-21.5669	1166	0.9507	182	-2011	2.29	28.57	16.24	1	0.16
Bassas da India	M-411S	39.8575	-21.5645	351	0.0825	44	-2081	5.89	14.10	9.14	84	0.12
Bassas da India	M-412S	39.8011	-21.5612	303	0.0664	55	-1691	5.39	17.50	11.78	0	0.18
Bassas da India	M-413S	39.8603	-21.5606	252	0.0437	56	-2124	2.97	17.92	11.23	90	0.22
Bassas da India	M-414	39.6227	-21.5586	132	0.0124	31	-1064	13.88	13.94	13.91	0	0.24

Bassas da India	SM-415	39.6259	-21.5581	357	0.0736	82	-967	7.26	21.54	16.93	163	0.23
Bassas da India	SM-416	39.9176	-21.5550	432	0.1360	134	-2232	3.29	28.66	19.06	18	0.31
Bassas da India	SM-417	39.8610	-21.5545	522	0.1973	153	-2067	12.73	33.31	23.20	165	0.29
Bassas da India	SM-418	39.6090	-21.5504	234	0.0404	55	-1233	12.81	21.98	17.87	0	0.23
Bassas da India	SM-419	39.7665	-21.5499	261	0.0489	30	-1396	4.83	15.28	9.98	162	0.12
Bassas da India	SM-420	39.7619	-21.5494	305	0.0656	45	-1305	5.13	22.40	13.40	150	0.16
Bassas da India	SM-421	39.6079	-21.5482	205	0.0403	48	-1225	13.64	21.62	17.28	90	0.24
Bassas da India	SM-422	39.7728	-21.5456	3[illegible]2	0.0722	52	-1422	2.96	18.59	10.83	160	0.17
Bassas da India	SM-423	39.[illegible]	21.5420	1200	0.5535	241	-1398	2.20	30.99	20.71	165	0.20
Bassas da India	SM-424	39.8035	-21.5300	1014	0.4278	174	-1617	3.29	30.48	19.48	42	0.17
Bassas da India	SM-425	39.8187	-21.5240	1443	1.1685	278	-1649	5.16	30.01	17.01	159	0.19
Bassas da India	SM-426	39.6255	-21.5228	608	0.2747	155	-412	9.06	27.00	22.38	0	0.25
Bassas da India	SM-	39.606	-21.5	330	0.07	76	-993	2.97	21.36	13.70	27	0.23

	427S	5	169		26							
Bassas da India	M-428S	39.6225	-21.5149	342	0.0834	88	-555	6.83	24.20	19.52	17	0.26
Bassas da India	M-429	39.8251	-21.2995	1140	0.7052	77	-3066	1.37	15.45	9.20	39	0.07

Table 3: Comparison of the offshore section of the volcanic ridges of Bassas da India/Europa complex, Hawaiian volcanoes (Mark and Moore, 1987; Fornari et al., 1988; Lonsdale, 1989; Clague et al., 2019), Canary Islands (Gee et al., 2001; Mitchell et al., 2002; Acosta et al., 2003b), Grande Comore Island (Tzevahirtzian et al., 2021), and Galapagos and Fernandina Islands (Harpp et al., 2003; Geist et al., 2006, 2008).

	Average long axis slope	Lenght	Width (max)
Bassas da India/Europa complex			
Hall Bank (east)	8-11°	10 km	5 km
Jaguar Bank (east)	4°	20 km	10 km
Bassas da India (east)	11°	10 km	5 km
Bassas da India (south)	6°	15 km	10 km
Ptolemee (south)	4°	40 km	3-6 km
Ptolemee (east)	6°	18 km	3 km
PS1 (east)	4°	30 km	3-5 km
PS1 (south)	8°	15 km	3-5 km
Canary Islands			
Cumbre Vieja Ridge	11-17°	38 km	27 km
El Hierro Northeast Ridge	22°	15 km	26 km
El Hierro Northwest Ridge	11-17°	16 km	26 km
Hawaii Islands			
Puna ridge	2-4°	70 km	> 40 km
Hilo Ridge	4°	40 km	20 km
Loihi	6-10°	11-19 km	20 km
Comoros archipelago			
Southeast Karthala	4°	13 km	15 km
Galapagos			
Genovesa	2-3°	50 km	20 km

Fernandina			
Fernandina NW Rift	9°	13 km	8 km

Figure 1

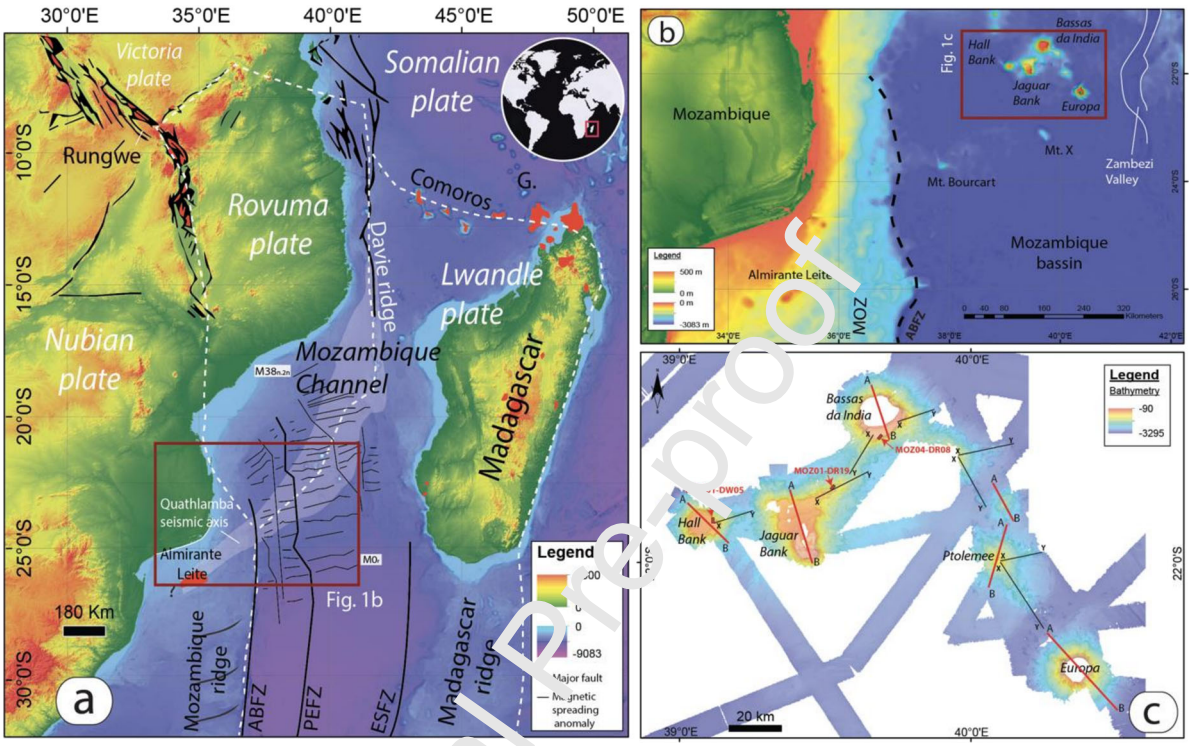

Figure 2

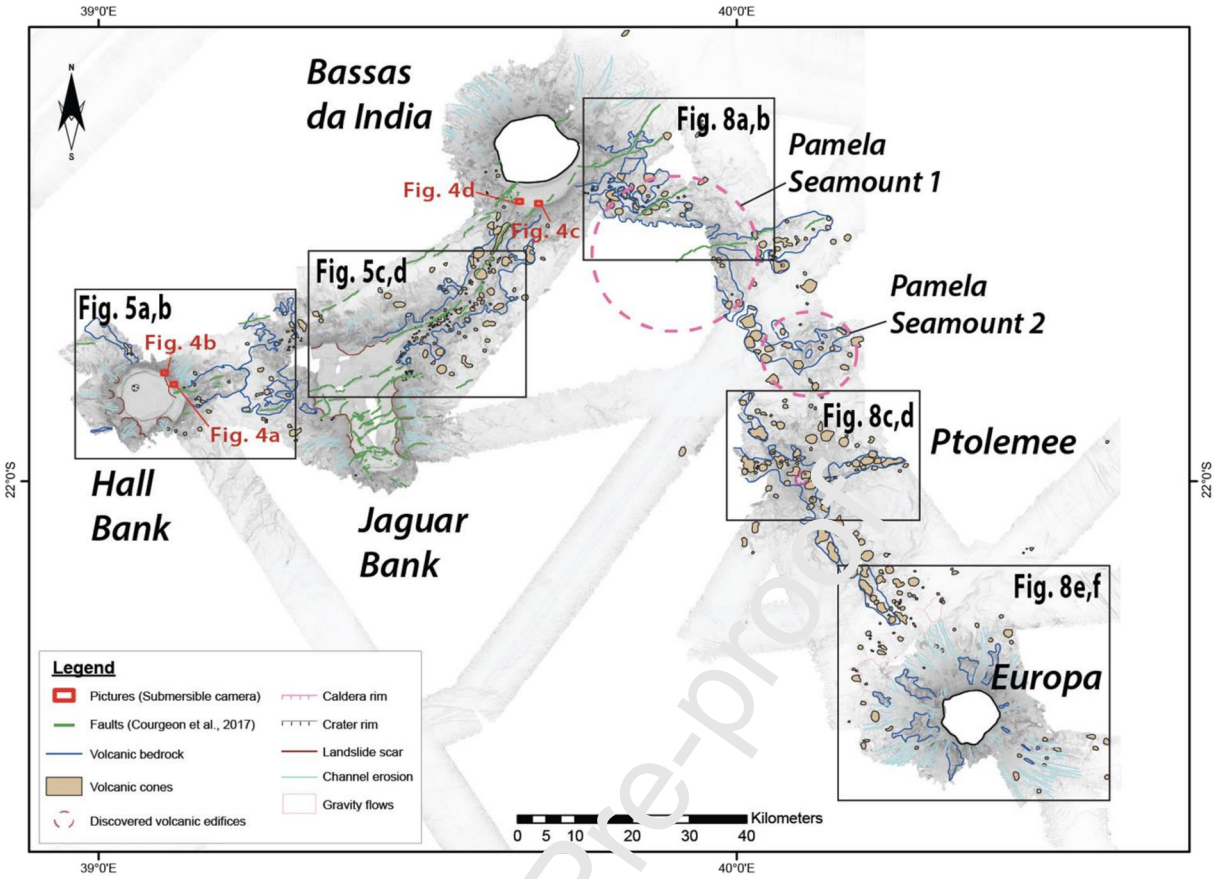

Figure 3

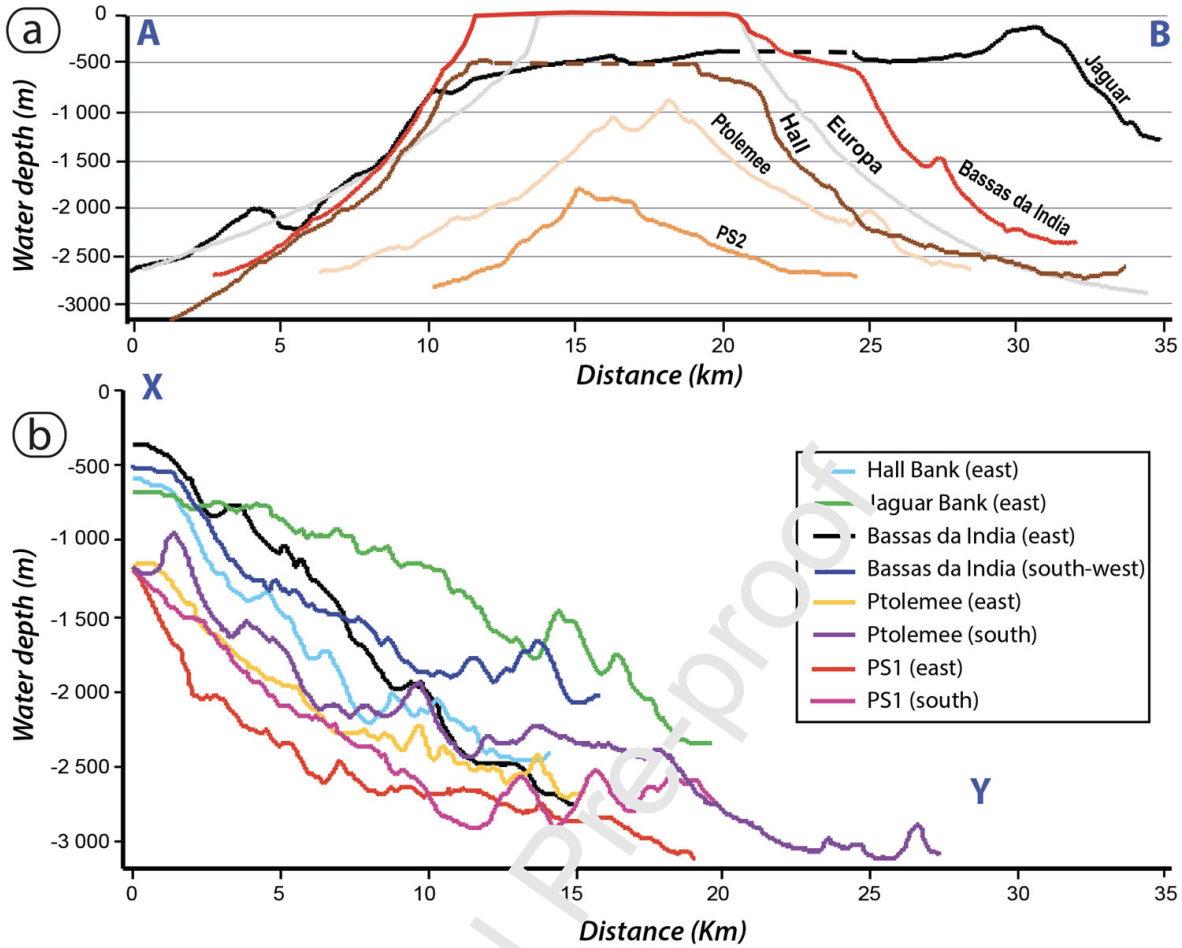

Figure 4

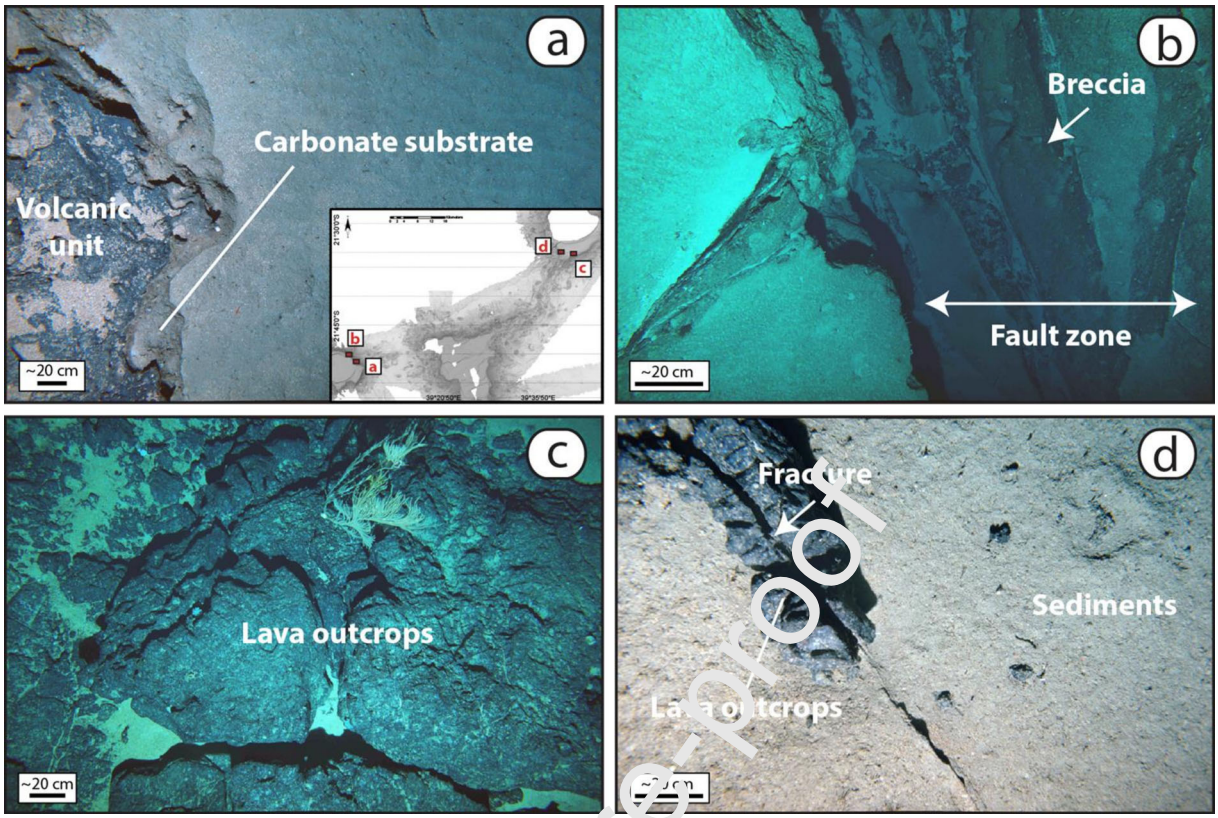

Figure 5

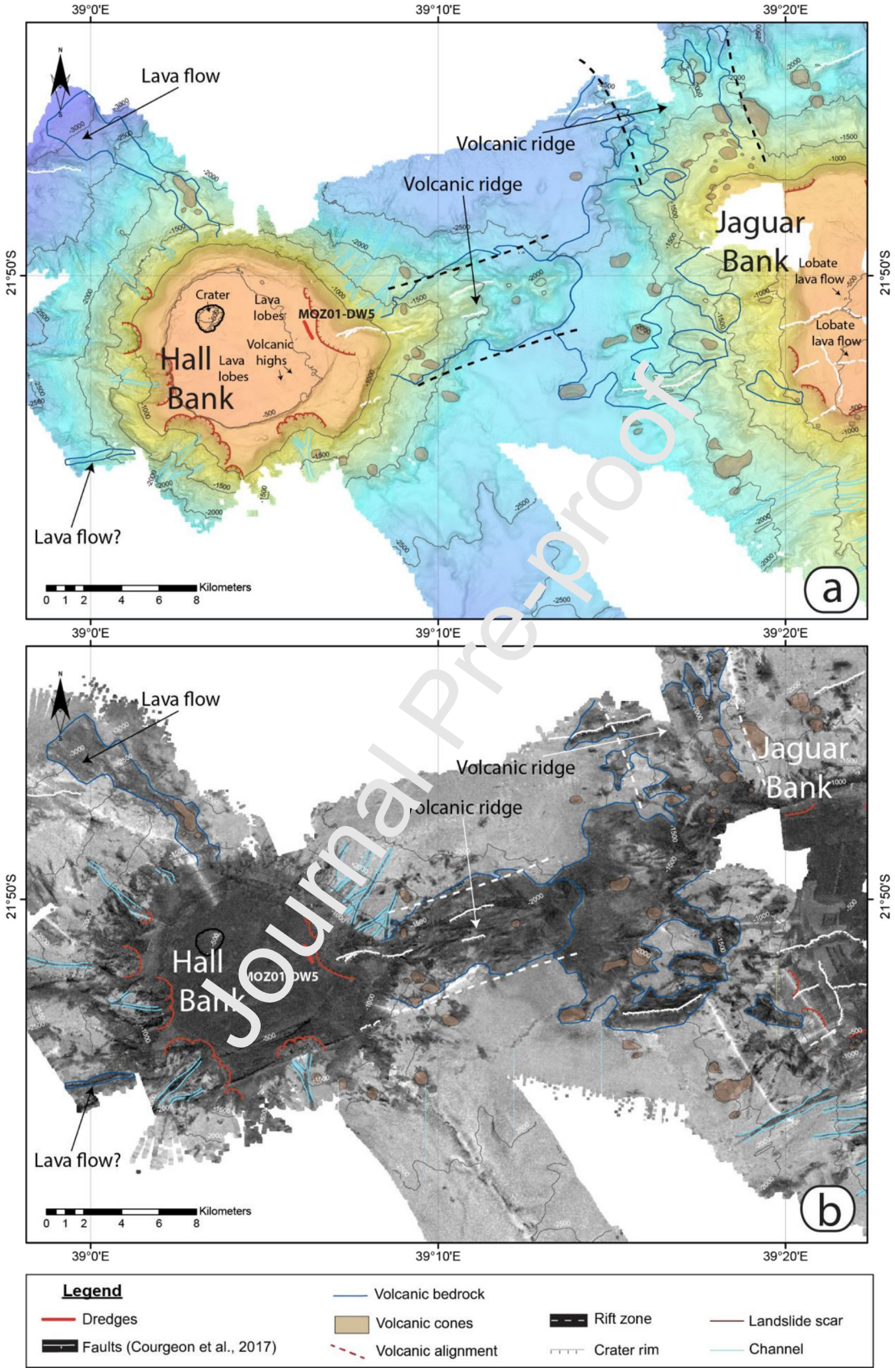

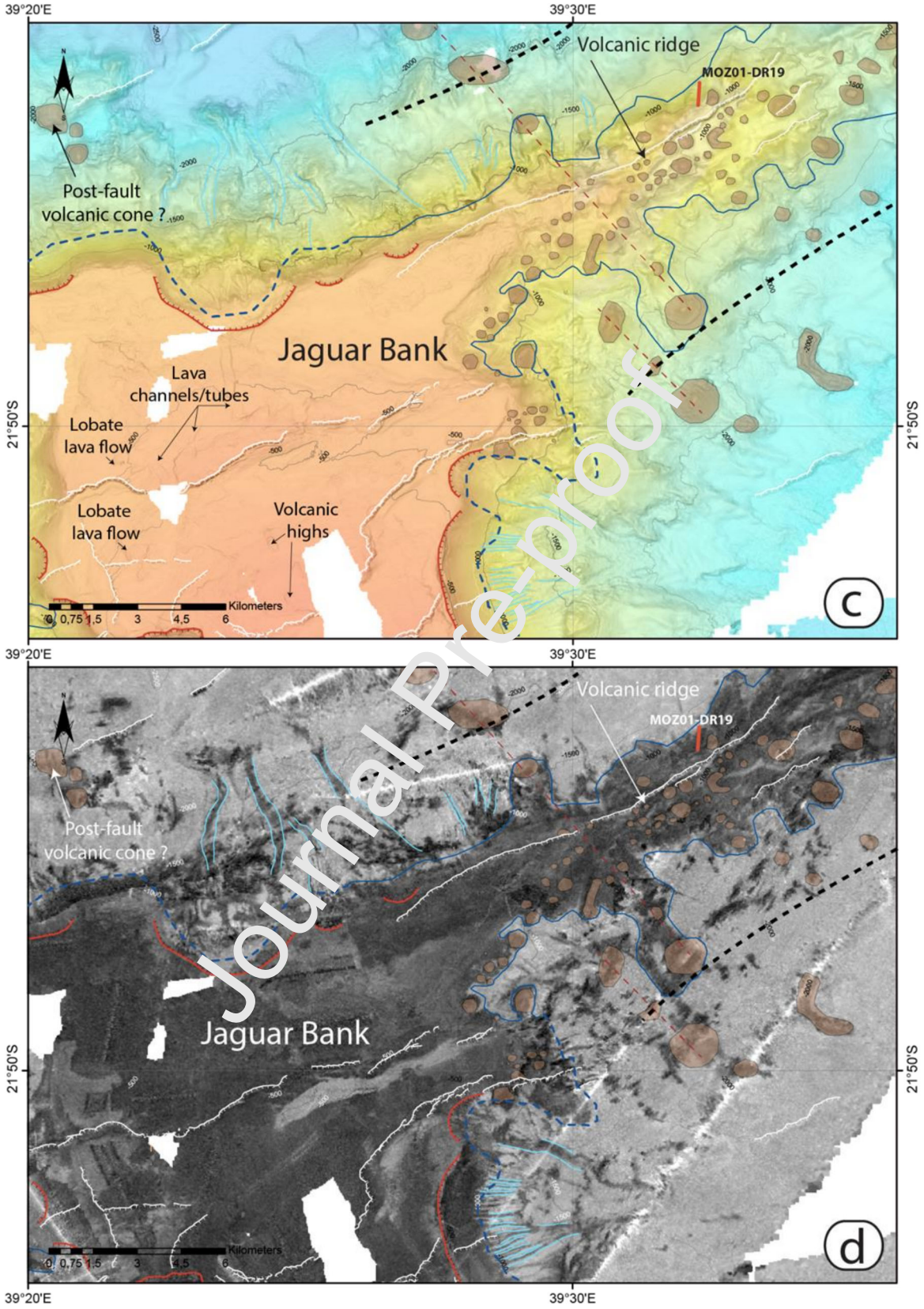

Figure 6

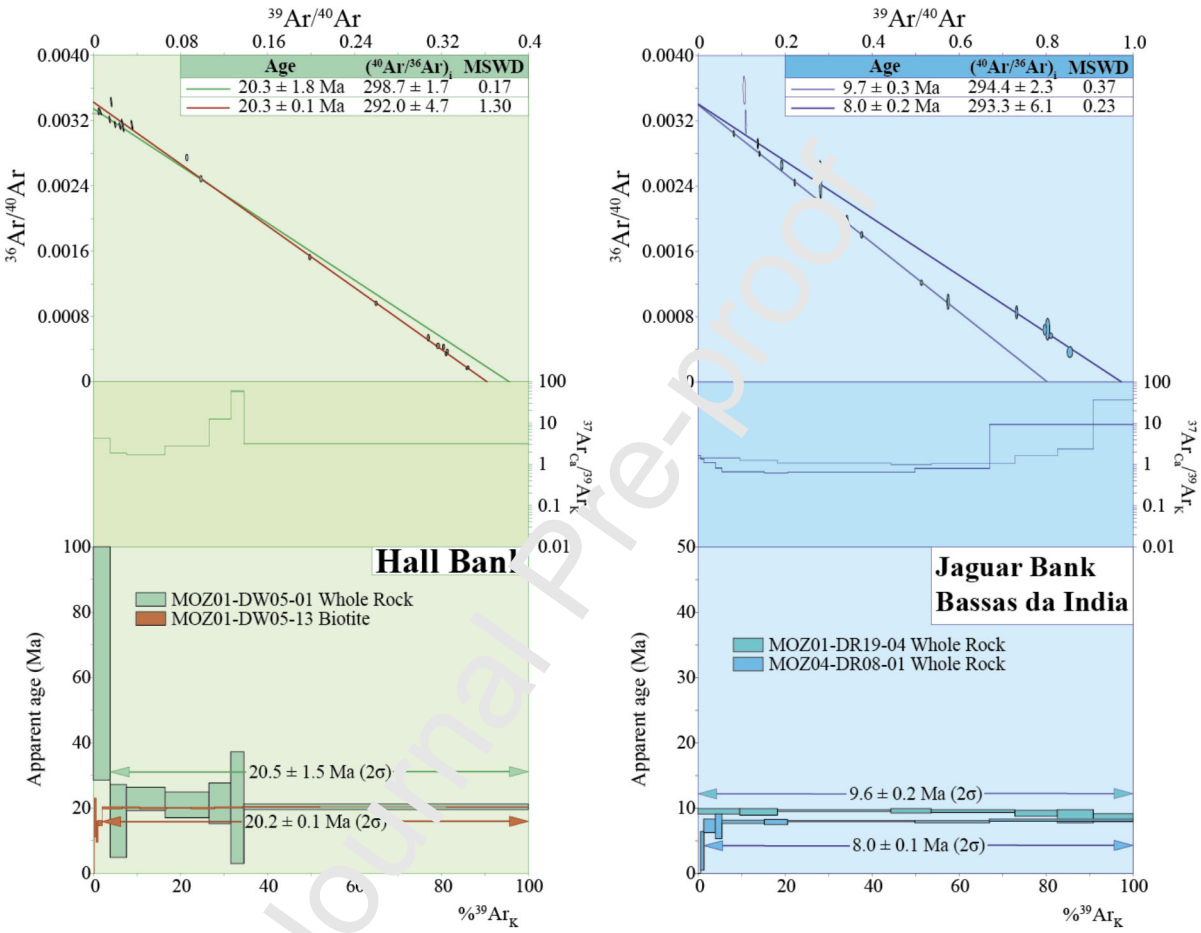
Age
(40Ar/36Ar)i
MSWD
20.3 ± 1.8 Ma
298.7 ± 1.7
0.17
20.3 ± 0.1 Ma
292.0 ± 4.7
1.30
MOZ01-DW05-01 Whole Rock
MOZ01-DW05-13 Biotite
20.5 ± 1.5 Ma (2σ)
20.2 ± 0.1 Ma (2σ)
Apparent age (Ma)
%39ArK
9.7 ± 0.3 Ma
294.4 ± 2.3
0.37
8.0 ± 0.2 Ma
293.3 ± 6.1
0.23
Jaguar Bank
Bassas da India
MOZ01-DR19-04 Whole Rock
MOZ04-DR08-01 Whole Rock
9.6 ± 0.2 Ma (2σ)
8.0 ± 0.1 Ma (2σ)

Figure 7

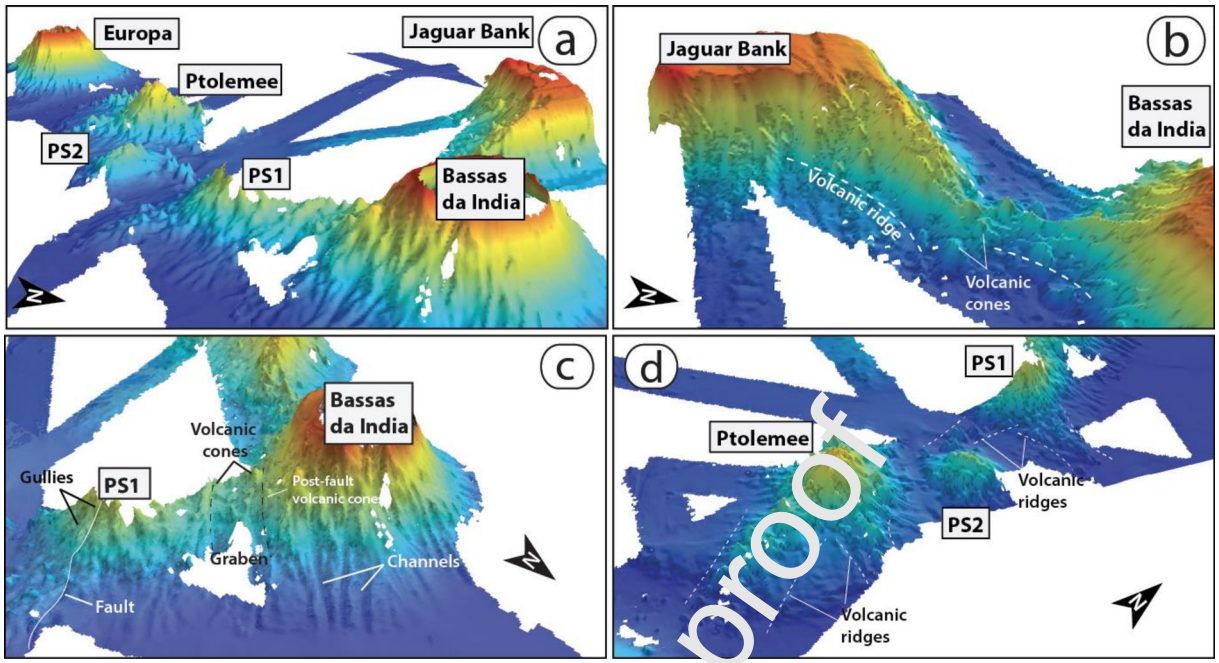

Figure 8

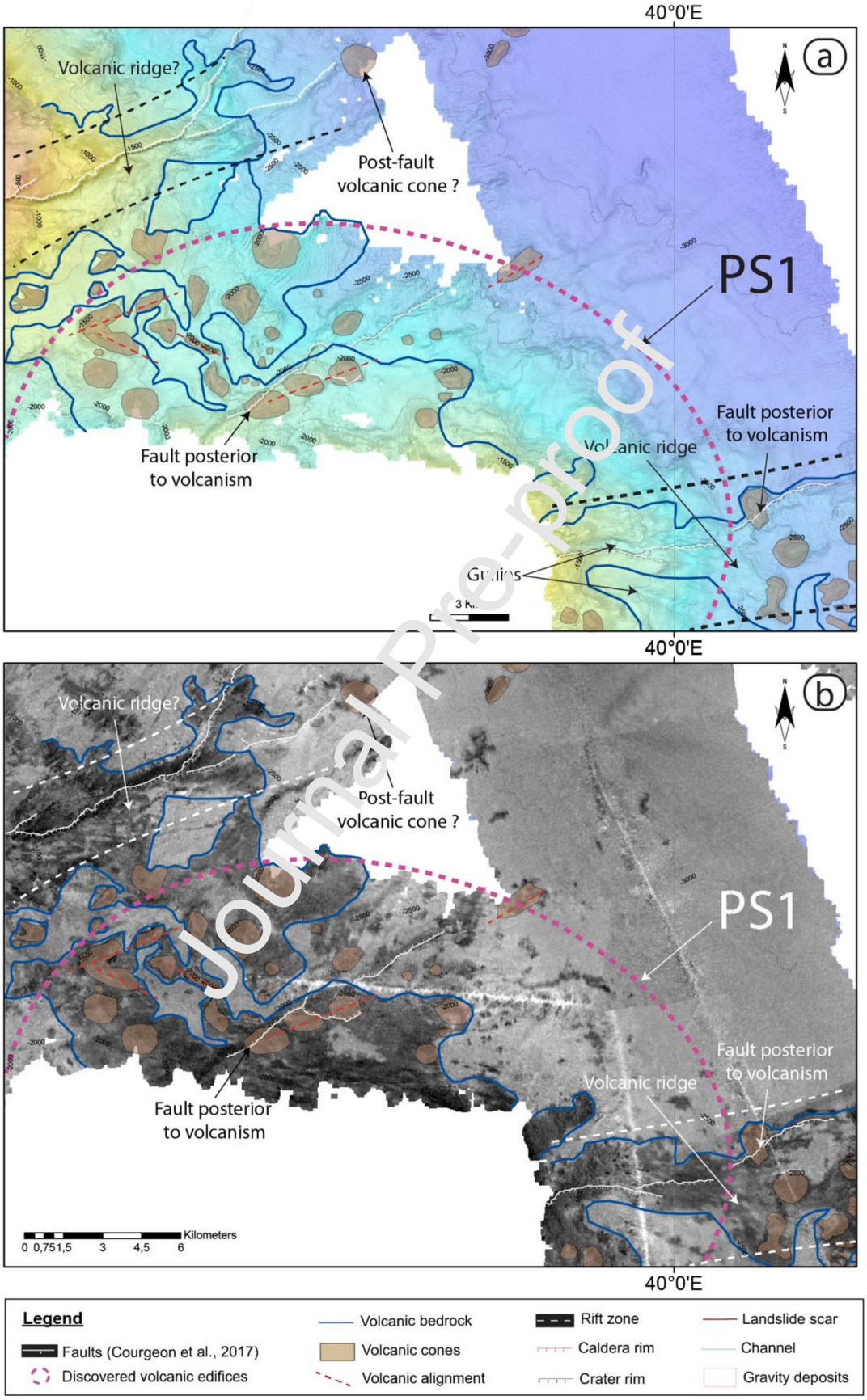

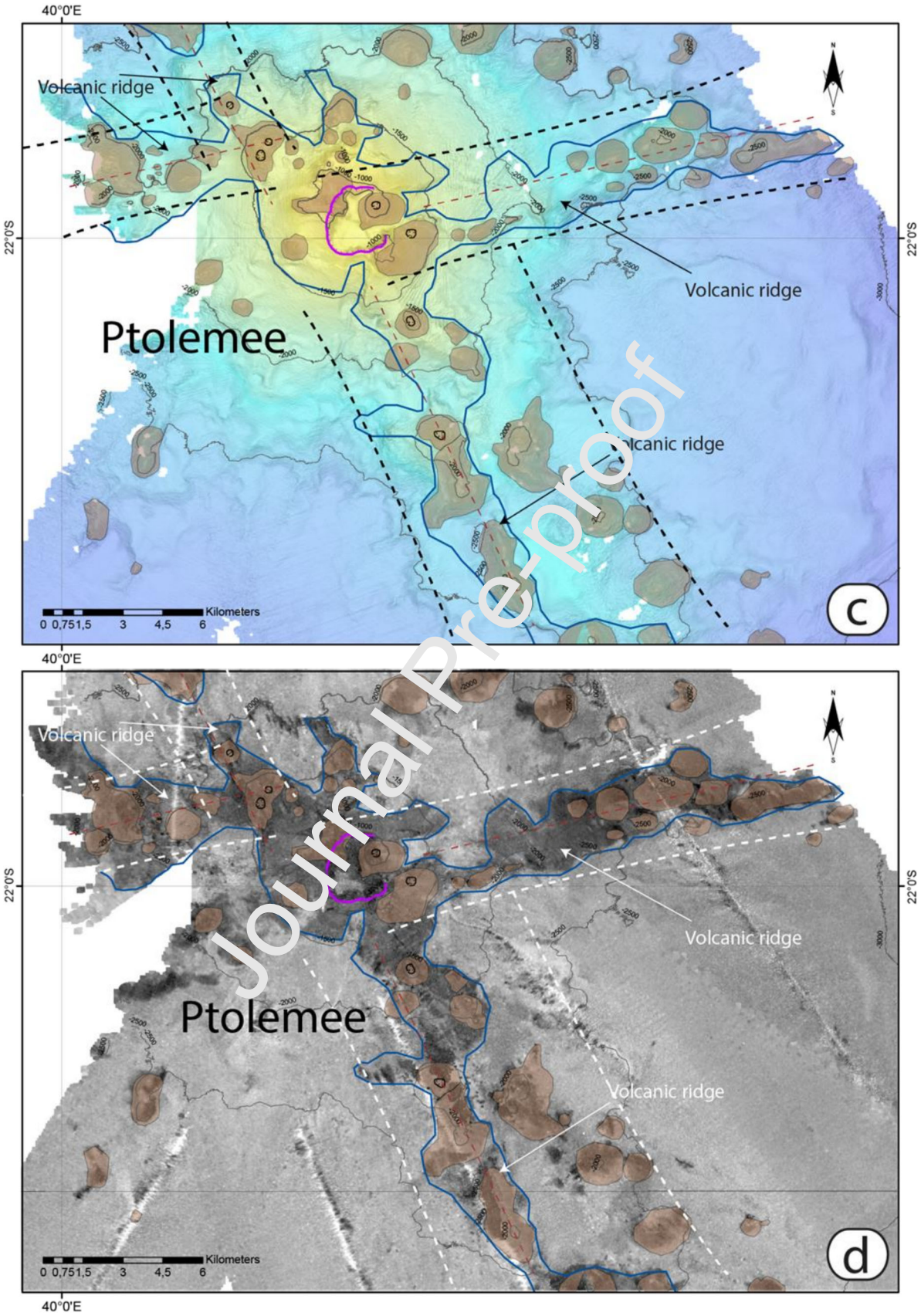

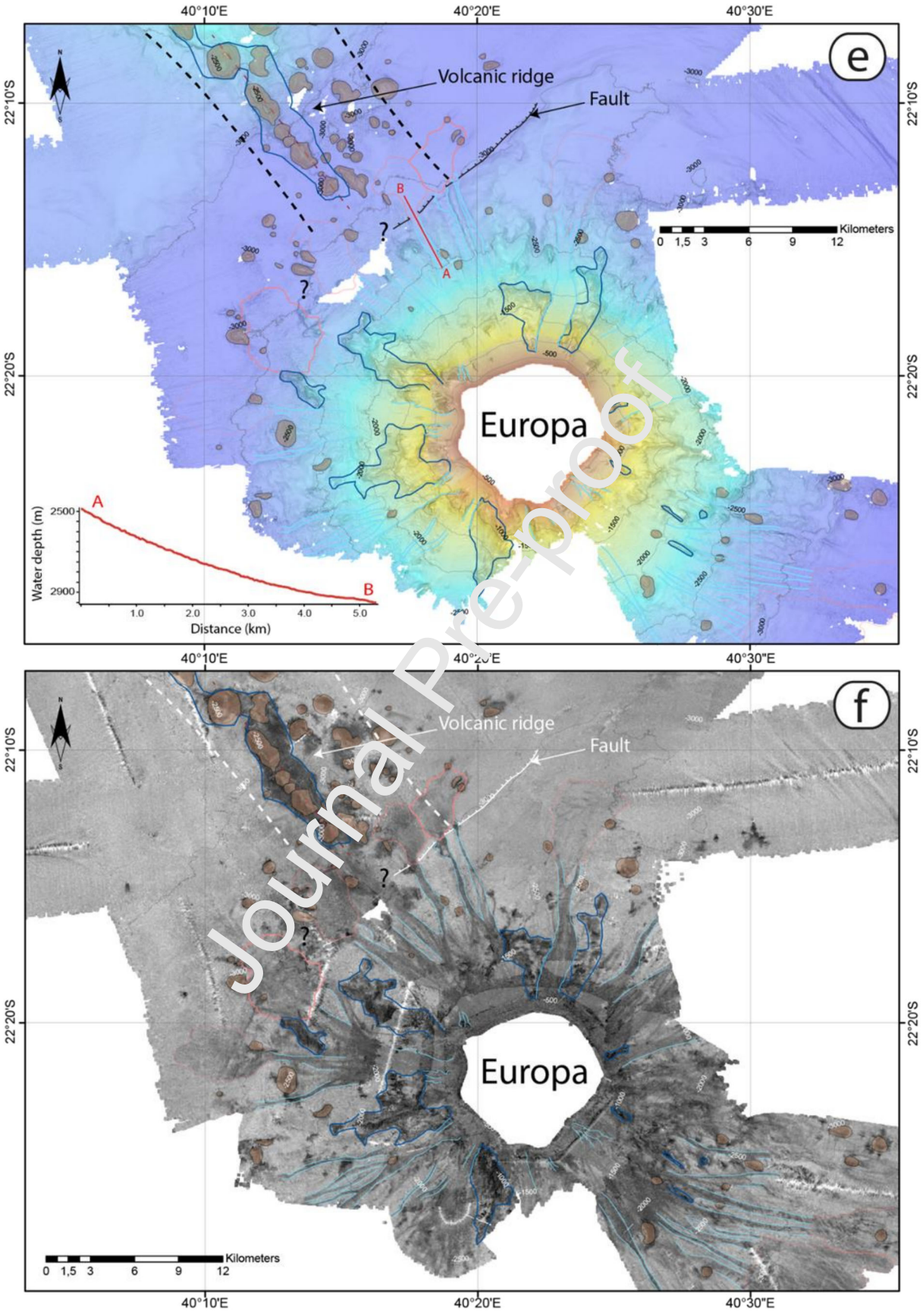

Figure 9

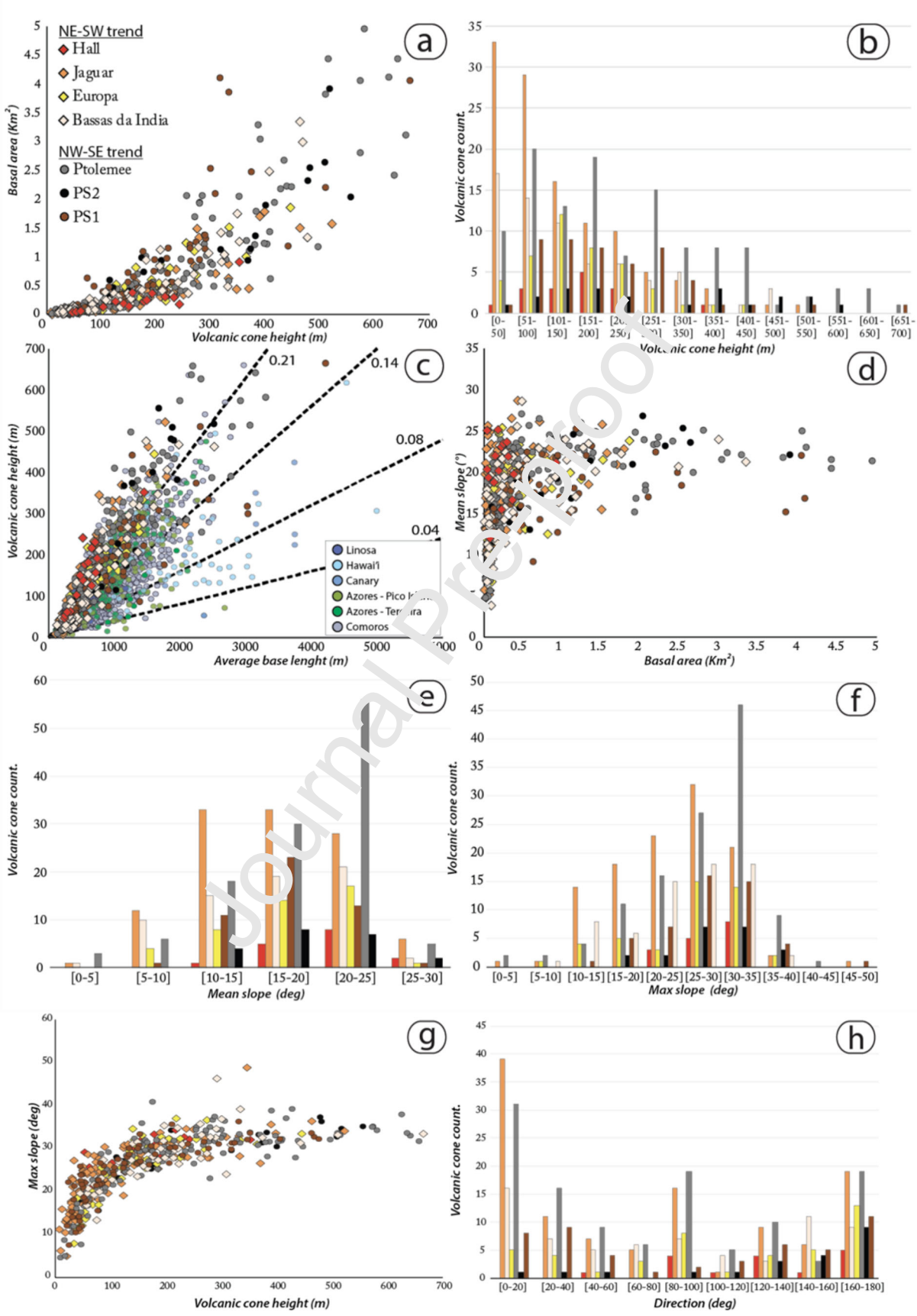

Figure 10

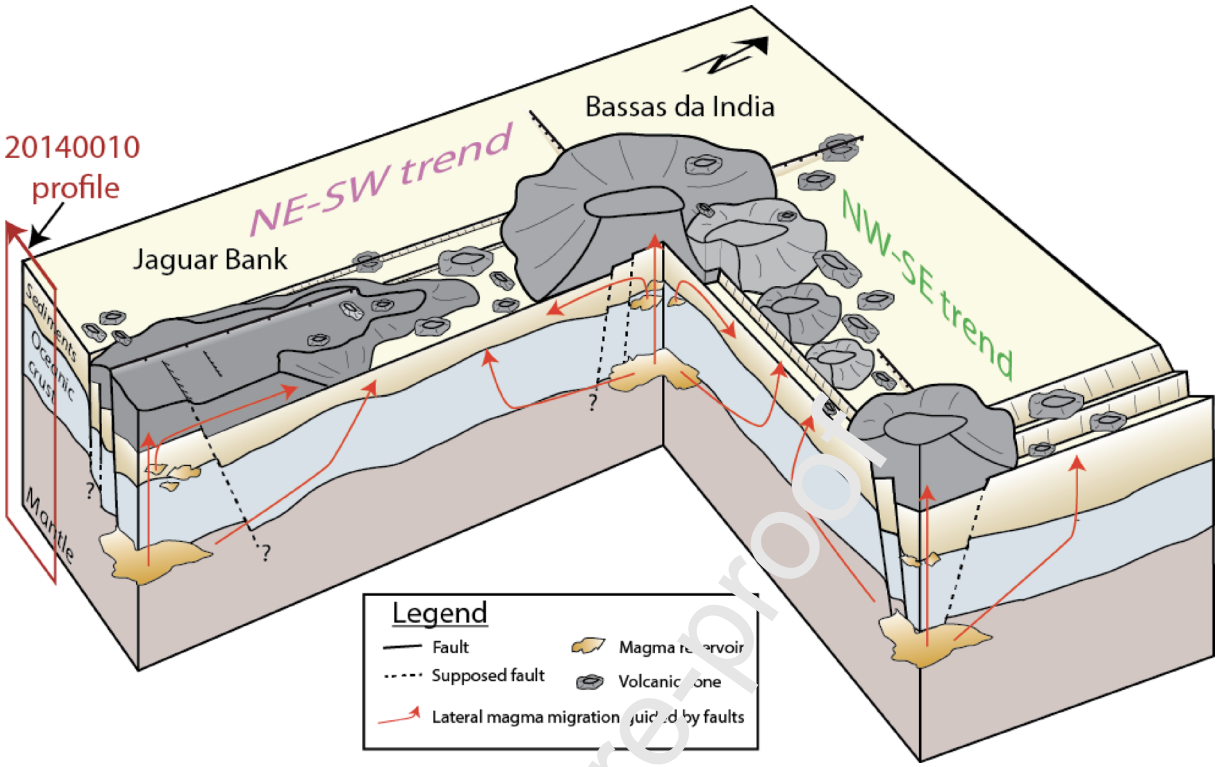

Figure 11

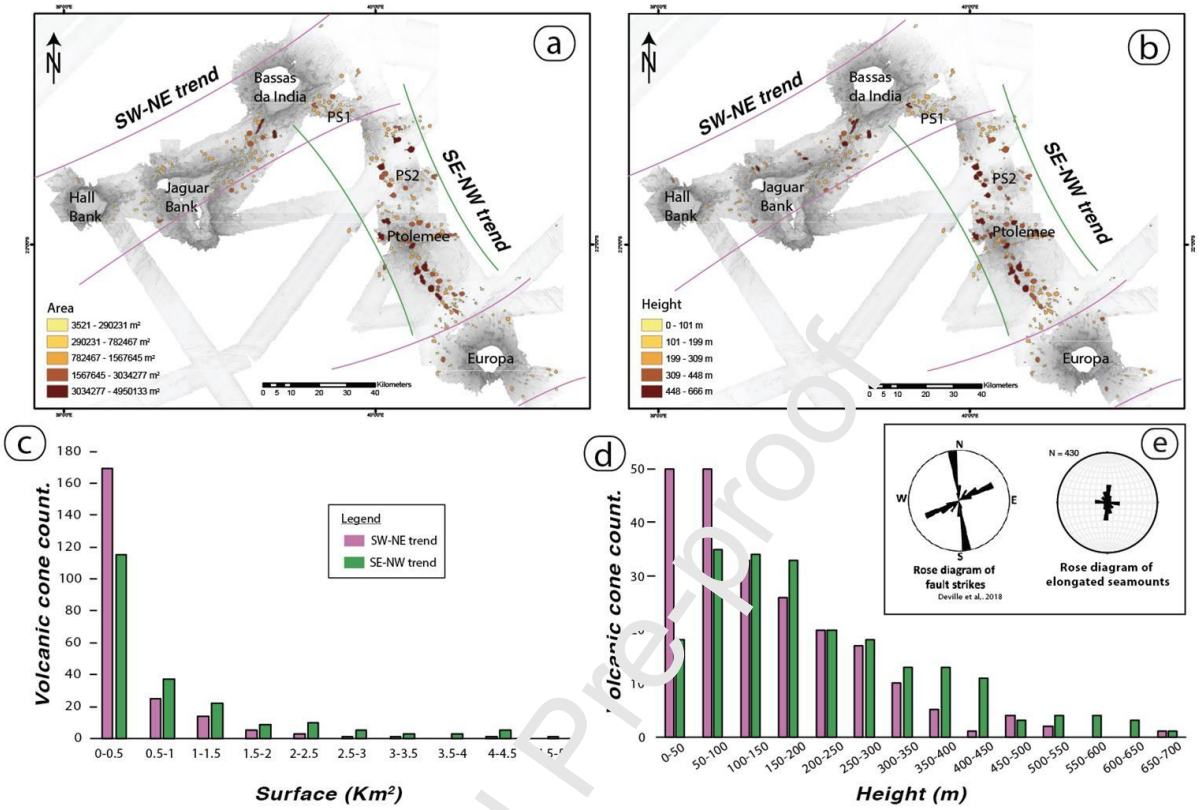

Supplementary material

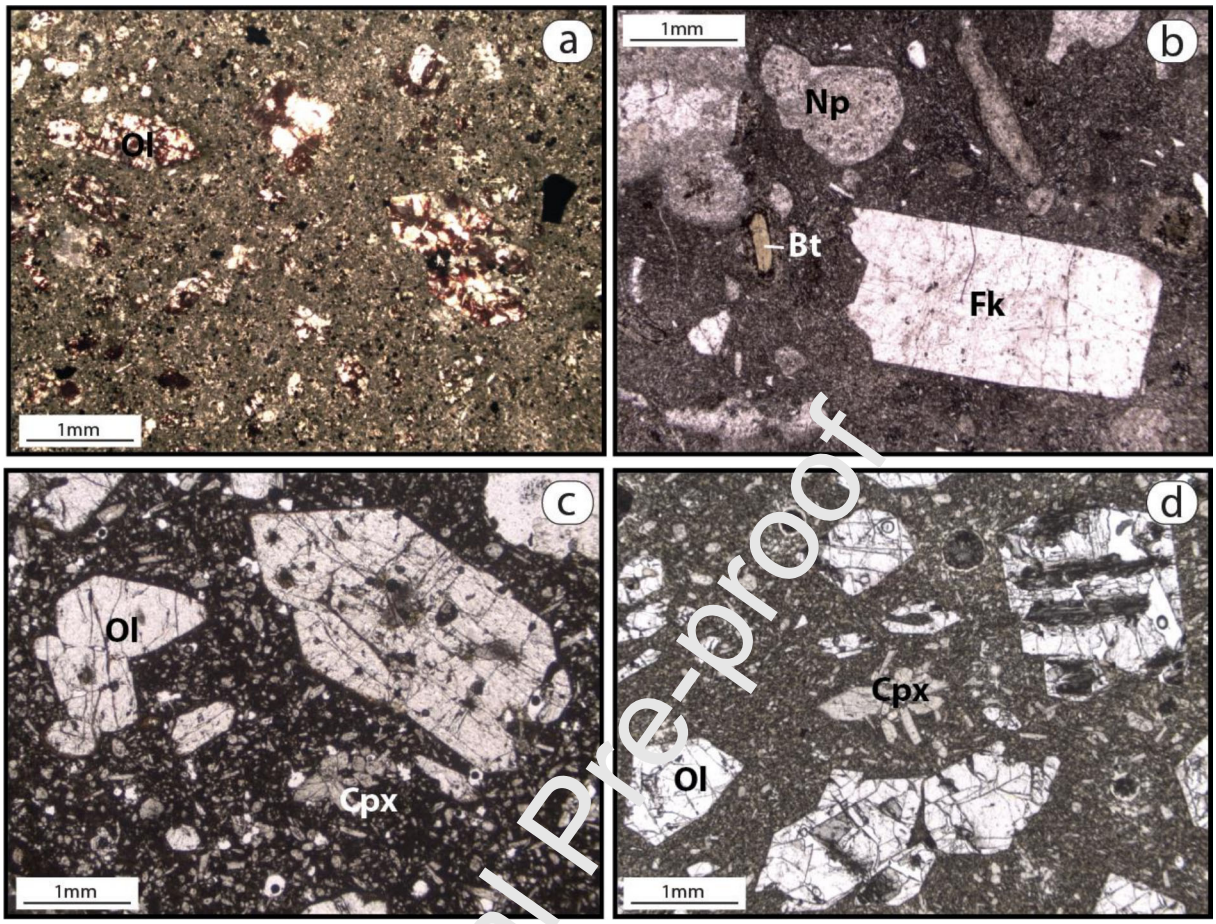

Figure S1: Petrological characteristics of the dated samples. a) MOZ01-DW05-01 collected on the Hall Bank is characterized by a porphyritic texture made of olivine phenocrysts, mostly iddingsitized, set in a fine-grained microcrystalline mesostasis. b) MOZ01-DW05-13 sample also collected on the Hall Bank has a moderately porphyritic texture, with phenocrysts set in a fine-grained microcrystalline mesostasis. The mineral assemblage includes alkali feldspar, nepheline, clinopyroxene, biotite, titanite, amphibole and Fe-Ti oxides; Feldspar is the dominant phenocryst phase and occurs as large euhedral to sub-euhedral crystals (0.5 mm – 4 cm). Samples MOZ01-DR19-04 (c) and MOZ04-DR08-01 (d), collected on the east volcanic ridge of the Jaguar Bank and on Bassas da India, respectively, display similar textures and paragenesis. Porphyritic ultramafic rocks are composed of sub-euhedral to euhedral olivine and zoned clinopyroxene phenocrysts (< 1 cm) embedded in an oxidized matrix with clinopyroxene microcrysts (< 500 μm).

Table S1: $^{40}Ar/^{39}Ar$ incremental heating experiments on our dredged samples.

			J parameter	error J			Mass Discrimination (1+e)	Err Discrimination							
	MOZ01-DW5-13 biotite		4.08E-03	1.39E-05			1.009908	1.33E-03							
step	40Ar	Error 40Ar	39Ar	Error 39Ar	38Ar	Error 38Ar	37Ar	Error 37Ar	36Ar	Error 36Ar	40Ar*/39Ar K	Error 40Ar*/39ArK	Apparent age (My)	Error Age (My)	Delay to irradiation (day)
1	385.411568	0.428596	6.509944	0.029067	0.000001	0.010199	0.510051	0.010898	1.382542	0.019291	0	0.920563	0	6.834839	196.974306
2	252.941334	0.247867	6.915365	0.015432	0.000001	0.008902	0.217861	0.018183	0.829109	0.018706	2.330799	0.806391	17.12405	5.896907	196.994444
3	314.274656	0.396079	11.230689	0.020672	0.009476	0.008083	0.695231	0.026279	1.038852	0.015839	1.735863	0.434794	12.768531	3.187405	197.013889
4	267.636822	0.192829	23.27455	0.065593	0.000001	0.009252	1.737723	0.027669	0.792768	0.008842	2.087948	0.123054	15.347407	0.902946	197.034028
5	542.244428	0.262818	109.030433	0.108392	0.000001	0.009583	4.301922	0.032841	0.930493	0.016375	2.730719	0.04652	20.045978	0.349722	197.074306
6	359.92882	0.28556	94.490864	0.179321	0.001153	0.009968	2.318811	0.03904	0.39568	0.006336	2.744075	0.022581	20.143474	0.184964	197.094444
7	480.464993	0.433517	149.38211	0.227387	0.000001	0.00797	2.163108	0.028907	0.304297	0.015778	2.721693	0.0317	19.980079	0.245936	197.674306
8	400.936632	0.390937	131.589392	0.205723	0.000001	0.009027	0.065927	0.010832	0.154752	0.008569	2.732862	0.020319	20.061617	0.170245	197.694444
9	393.060208	0.379621	127.636468	0.139604	0.000001	0.009619	0.086873	0.010653	0.17396	0.009828	2.712551	0.023405	19.913339	0.189938	197.713889
10	480.437759	0.519898	153.474684	0.263251	0.000001	0.00787	0.08443	0.010797	0.220714	0.012953	2.741474	0.025797	20.124485	0.206128	197.734028
11	1272.68246	1.253008	416.4303	0.341594	0.000001	0.014453	0.236125	0.015162	0.451383	0.018299	2.769214	0.01433	20.32698	0.134565	197.774306
12	1987.91084	0.78428	688.467334	0.569702	0.000001	0.014311	0.184131	0.016143	0.336427	0.015797	2.769914	0.008437	20.332091	0.1047	197.794444
Fusion	1288.90899	1.389094	447.999198	0.46926	0.000001	0.013076	0.106165	0.009742	0.232223	0.016558	2.750672	0.012378	20.191633	0.123435	197.824306

			J parameter	error J			Mass Discrimination (1+e)	Err Discrimination							
	MOZ01-DR19-04 Whole Rock		4.32E-03	1.47E-05			1.006618	1.31E-03							
step	40Ar	Error 40Ar	39Ar	Error 39Ar	38Ar	Error 38Ar	37Ar	Error 37Ar	36Ar	Error 36Ar	40Ar*/39Ar K	Error 40Ar*/39ArK	Apparent age (My)	Error Age (My)	Delay to irradiation (day)
1	752.219412	0.558791	168.775152	0.247464	0.007708	0.026546	45.356493	0.138616	1.964096	0.028882	1.216715	0.053667	9.478394	0.418855	85.135417
2	434.073944	0.770252	149.564211	0.190932	0.000001	0.022149	35.32527	0.086195	0.935121	0.033183	1.211245	0.066061	9.435891	0.514796	85.154861
3	885.841882	0.616075	458.186266	0.321156	0.013175	0.018783	92.624707	0.207301	1.264601	0.023816	1.240643	0.016246	9.664298	0.132502	85.175
4	277.496082	0.236155	160.677318	0.235519	0.031058	0.035546	29.917103	0.075644	0.330806	0.024992	1.23001	0.04581	9.581694	0.35815	85.204861
5	890.507637	0.673696	337.104247	0.295343	0.012218	0.032726	66.131921	0.13799	1.76228	0.029541	1.228294	0.027351	9.568362	0.216221	85.225
6	1195.85101	2.551598	170.164897	0.553717	0.005016	0.017899	51.449434	0.194476	3.517098	0.0[illegible]798	1.180244	0.061275	9.195005	0.47771	85.815278
7	1732.53458	6.604745	144.266204	0.622706	0.000001	0.027761	63.589164	0.278817	5.516084	0.0[illegible]98	1.12539	0.129336	8.768684	1.005975	85.835417
Fusion	827.38112	2.307547	164.636052	0.584807	0.000001	0.034934	1099.10002	4.162705	4.191983	0.041[illegible]	1.096235	0.083524	8.542055	0.650279	85.854861

			J parameter	error J			Mass Discrimination (1+e)	Err Discrimination							
	MOZ01-DW5-01 Whole Rock		4.31E-03	1.46E-05			1.006618	1.31E-03							
step	40Ar	Error 40Ar	39Ar	Error 39Ar	38Ar	Error 38Ar	37Ar	Error 37Ar	36Ar	Er[illegible]36Ar	[illegible]Ar*/39Ar K	Error 40Ar*/39ArK	Apparent age (My)	Error Age (My)	Delay to irradiation (day)
1	3912.15731	12.641408	8.862702	0.029537	0.04684	0.036467	59.764598	0.104782	13.321[illegible]76	[illegible]19667	8.586164	4.942875	65.685929	37.136345	92.045139
2	1223.89152	2.696425	8.174462	0.038631	0.003056	0.036381	25.1137	0.16177	4.2[illegible]38	0.0[illegible]2198	2.06305	1.45087	16.001938	11.204139	92.065278
3	981.836203	1.964471	19.811315	0.066767	0.016114	0.035836	54.81991	0.162053	[illegible]89.[illegible]	0.[illegible]5327	2.944215	0.467239	22.79372	3.595847	92.085417
4	898.178117	1.131746	22.53953	0.041194	0.014325	0.036841	101.092521	0.153263	[illegible]088006	[illegible]035005	2.696969	0.510734	20.890593	3.934313	92.104861
5	724.032838	2.209216	11.951379	0.037835	0.000001	0.032872	222.932076	0.652743	[illegible]3405	0.025988	2.770315	0.810394	21.45537	6.239835	92.145139
6	1311.47625	2.002547	9.650924	0.056109	0.000001	0.031795	636.290765	1.82131[illegible]	5.7[illegible]7	0.042583	2.585703	2.21952	20.03349	17.10166	92.165278
Fusion	1440.58644	1.843377	146.687293	0.29507	0.000001	0.034705	733.712539	2.111[illegible]5	[illegible]14158	0.04157	2.625534	0.098287	20.340363	0.761901	92.185417

			J parameter	error J			Mass Discrimination (1+e)	Err Discrimination							
	MOZ04-DR08-01 Whole Rock		4.33E-03	1.47E-05			1.006618	1.31E-03							
step	40Ar	Error 40Ar	39Ar	Error 39Ar	38Ar	Error 38Ar	37Ar	Error 37Ar	36Ar	Error 36Ar	40Ar*/39Ar K	Error 40Ar*/39ArK	Apparent age (My)	Error Age (My)	Delay to irradiation (day)
250	155.054117	0.48814	16.574689	0.086119	0.008541	0.029195	4.397[illegible]07	0.03387	0.578154	0.026283	0	0.468309	0	3.67728	92.825
2	175.08921	0.333479	19.429654	0.072289	0.000001	0.019195	4.224[illegible]03	0.0[illegible]135	0.581273	0.024799	0.442332	0.376942	3.460338	2.946016	92.845139
3	476.071677	0.504718	66.005708	0.201061	0.000001	0.030458	11[illegible]23[illegible]	0.[illegible]4813	1.450318	0.028216	0.933555	0.130037	7.295409	1.014602	92.865278
4	129.112283	0.220541	36.528654	0.099535	0.000001	0.02141	[illegible]23482	0.05035	0.337984	0.029999	0.926878	0.240956	7.243337	1.879491	92.885417
5	336.964462	0.40802	248.328634	0.330411	0.000001	0.030983	26.[illegible]945	0.072977	0.349696	0.025152	1.016045	0.029901	7.938628	0.235455	92.915278
6	172.117981	0.654262	139.003518	0.379131	0.000001	0.027684	3.9653[illegible]	0.077275	0.142801	0.022079	1.004061	0.046887	7.845195	0.367021	92.935417
7	913.641183	1.517056	744.708571	1.507084	0.000001	0.027294	77.590259	0.429754	0.689724	0.027833	1.024483	0.011613	8.004407	0.096501	92.965278
8	541.566323	0.898145	434.617078	0.563821	0.000001	0.027416	56.133091	0.238338	0.469281	0.031435	1.013925	0.02149	7.9221	0.17077	92.975
Fusion	981.594324	1.969666	845.241982	2.424601	0.073196	0.042349	1261.731225	2.872931	2.939812	0.058694	1.047889	0.021177	8.186866	0.168578	92.995139

Parameters	(36Ar/37Ar)Ca	0.000322	3 %
	(39Ar/37Ar)Ca	0.000788	4 %
	(38Ar/37Ar)Ca	0.000026	100 %
	(40Ar/37Ar)Ca	0.0006	100 %
	(40Ar/39Ar)K	0.00085	4 %
	(38A/39Ar)K	0.011	91 %
[3]	(36Cli/38Cl)	316	5 %
[1] and [1']	(40Ar/36Ar)At	298.56	0.104 %
[1] and [1']	(38Ar/36Ar)At	0.1885	0.159 %
[2]	Lambda 40	5.53E-10	1.35E-12 y-1
	Lambda 39	2.58E-03	y-1
	Lambda 37	1.98E-02	d-1
	Lambda 36Cl	2.26E-06	y-1

References:

[1] Lee, JY, Marti, K, Severinghaus, JP, Kawamura, K, Yoo[illegible]ee, J[illegible]JS (2006). A redetermination of the isotopic abundances of atmospheric Ar. Geochimica Cosmochimica Acta, 70, 4507-4512.

[1'] Mark, DF, Stuart, FM, De Podesta, M (2011). New h[illegible]gh-preci[illegible]n measurements of the isotopic composition of atmospheric argon. Geochimica Cosmochimica Acta, 75, 7494-7501.

[2] Renne, PR, Balco, G, Ludwig, RL, Mundil R, Min[illegible] (2011). R[illegible]sponse to the comment by W.H. Schwarz et al. on "Joint determination of (40)K decay constants and (40)Ar*/(40)K for the Fish Canyon sanidine standard, and improved accuracy for (40)Ar/(39)Ar geochronology" by PR R[illegible]e et al.[illegible]010)[illegible]ochimica Cosmochimica Acta, 75, 5097-5100.

[3] York, D, Personnal Communication - McMast[illegible]ector

Regression metho York, D. (1969). Least-squares fitting of a straight li[illegible]with correlated errors. Earth Planet. Sci. Lett. 5, 320-4.

f Hb3gr and TCs m Rennes, PR, Balco, G, Ludwig, Mundil, R, Min, K, .(2[illegible]1). Response to the comment by W.H. Schwarz et al. on "Joint determination of (40)K decay constants and (40)Ar*/(40)K for the Fish Canyon sanidine standard, and improved accuracy for (40)Ar/(39)Ar geochronology" by PR Renne[illegible](2010). Geochimica Cosmochimica Acta, 75, 5097-5100.

Declaration of interests

☒ The authors declare that they have no known competing financial interests or personal relationships that could have appeared to influence the work reported in this paper.

☐The authors declare the following financial interests/personal relationships which may be considered as potential competing interests:

Highlights

- Bassas da India/Europa seafloor is characterized by seven large seamounts and more than 430 volcanic cones
- Miocene to Pleistocene volcanism is distributed along two main trends with different stages of maturation
- Magma ascent is strongly controlled by large pre-existing crustal structures
- Large edifices are fed by a well-developed magmatic system whereas volcanic ridges are supplied by episodic lateral magma migration though a network of faults.